STUDY OF ACTIVE CARBONS

BY

RAYMOND WILLIAM INNES

being a thesis submitted for the degree of Doctor of Philosophy in the Chemistry Department of the University of Glasgow.

SEPTEMBER 1988

ACKNOWLEDGEMENT

I would like to thank my supervisors, Dr. John Fryer and Prof. Fritz Stoeckli for their help and guidance throughout the course of this work as well as Dr. Tom Baird who also offered much useful advice.

I must also offer my thanks to the members of the Physical Chemistry Department of Neuchâtel University and the Electron Microscopy Section of Glasgow University for their help and discussion and in particular, David Thom for his technical assistance.

My thanks also go to the people in both Glasgow and Neuchâtel who have offered me support during the course of this work.

Finally, I must acknowledge the SERC for their financial support, without which the production of this thesis would not have been possible.

CONTENTS

SUMMARY

The intention of the present work was to examine a series of active carbons using a number of techniques. The series of carbons was produced from a commercial charcoal which was first carbonised and the activated at 850°C using carbon dioxide. The activation time was varied to produce a series of carbons possessing different degrees of burn-off.

Histograms showing the micropore size distributions were obtained from both high resolution electron microscopy and immersion calorimetry. Immersion calorimetry is a macro-technique whereby the sample is immersed in a variety of organic liquids and the quantity of heat released is correlated with a value of pore volume. Using this technique with molecular probes of increasing critical dimensions results in a set of values showing the pore volumes accessible to each of the probes which can then be used to construct a histogram of the micropore size distribution. High resolution electron microscopy on the other hand, is a technique whereby individual pores are imaged and then measured directly from the micrographs. This technique also results in a histogram showing the micropore size distribution. As the immersion results are averaged over many pores they are more statistically sound, microscopy however, because of its very nature, results in a clearer picture of pore structure.

In order for the results obtained from these two methods

to be compatible, certain assumptions had to be made based on theoretical calculations. These calculations had suggested that the interaction radius of an adsorbate molecule would be reduced during adsorption in a micropore. This reduction had to be accounted for, as did the finite widths associated with the carbon atoms constituting the micropore walls and this was undertaken by subtracting a value of 0.2nm from those results obtained from high resolution electron microscopy.

When these corrections had been made, it was found that for most of the carbons studied, the agreement between the two techniques was reasonable, especially in the region below around 0.6nm, seeming to validate the Everett and Powl model on which the corrections were based. The disagreement encountered in the region of larger pore size also had interesting implications, suggesting that rather than slit-pores, most of the pores in this range were of a different nature. Microscopical evidence was also provided showing the structure of these larger pore types to be quite varied. It was also shown that the quantity of such porosity increased with the increasing degree of activation of the sample under investigation, a property reflected quantitatively from immersion results and qualitatively from electron microscopy. The microscopical evidence presents a structure for the higher burn-off carbons where these larger pore types are spread through the specimen interconnected by a network of smaller pores. It also appears that these smaller pores must undergo exfoliation in order for the quantity of vapour that was adsorbed to occur.

In addition to these investigations, a variety of methods were also employed in order to discover the average pore size of some of the samples from their adsorption isotherms. The results of this investigation showed that for the carbons in this work at least, reliable results on average pore sizes could not be deduced from the adsorption isotherms.

A final area of investigation, in addition to that of the active carbons, was a brief examination of some coke samples. These coke samples were activated in a similar manner to the carbons, however the resulting information that was obtained for the densities and immersion values of the series of cokes that had been produced showed little variation with the degree of activation, so no detailed assessment of these samples was undertaken.

INTRODUCTION

1.1 Graphite Structure

1.1.1 Ideal Lattice

Carbon is a naturally occurring element which exists, in its pure form, in one of two main polymorphic forms: graphite and diamond. In diamond the carbon atoms are bound by sp^3 hybridised bonds of length 0.154 nm, which results in a tetrahedral structure and the characteristic strength associated with diamond. In graphite however, the structure is somewhat more complicated.

The crystal structure of graphite has been studied extensively since the early work of Ewald (1914), Debeye and Scherrer (1917), Hassel and Mark (1924) and Bernal (1924). It is composed of infinite planes, formed from carbon atoms ordered in regular hexagons, similar to those in the rings of aromatic organic compounds. The carbon atoms in each individual layer are bound to their nearest neighbour by three sp^2 hybridised orbitals, separated by bond angles of 120°. The interatomic distance between these atoms is 0.1421 nm. The layer planes are in a parallel array, bound together by van der Waals forces and the interlayer spacing for well oriented graphite is 0.33538 nm (Franklin, 1951). In less well oriented graphite, Franklin stated that the experimentally determined interplanar distance is an average value, which is dependent on the proportion of both oriented layers

with a spacing of 0.33538 nm and disoriented layers of 0.344 nm spacing.

The stacking sequence between the carbon layers in graphite has been shown to be of the ABAB... type i.e. the alternate layers are superimposable (Bernal, 1924 ; Maughin, 1926). The plane unit cell of this structure is defined by two atoms A_o and B_o and two crystallographic vectors $\underset{\sim}{a}_1$ and $\underset{\sim}{a}_2$ which are separated by an angle of 120° (figure 1.1). The unit length of these vectors is 0.246 nm. In order to define the three dimensional hexagonal structure of graphite, a further vector $\underset{\sim}{a}_3$ is necessary. This vector is perpendicular to the plane of the layers and its unit length is twice the distance between adjacent layer planes i.e. 0.6708 nm (Chartier and Chartier, 1987). Figure 1.2. illustrates the hexagonal graphite structure and the equivalence of the alternate layers. The relationship between adjacent layers is also apparent as being a translation of one carbon-carbon bond length.

In addition to the hexagonal form, graphite has also been shown to exist as a rhombohedral structure (Laidler and Taylor, 1940 ; Lipson and Stokes, 1942(a) and (b)). This type of graphite possesses an ABCABC... stacking sequence, in which the third layer has the same relative position to the second layer as the second layer has to the first. This rhombohedral structure appears to exist as a small percentage within the hexagonal form (Finch and Wilman, 1936 ; Boehm and Hoffman, 1955) and never on its own. It is thermodynamically less stable than the hexagonal

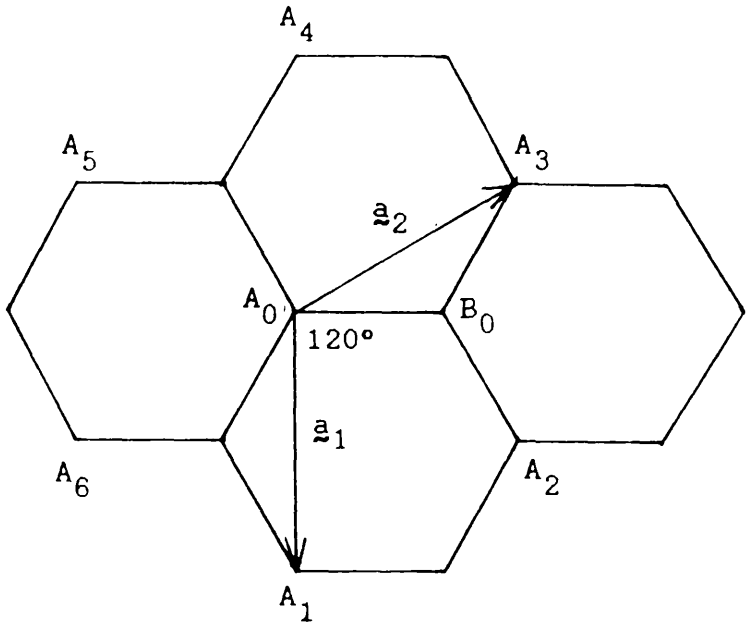

Figure 1.1

Graphite layer plane.

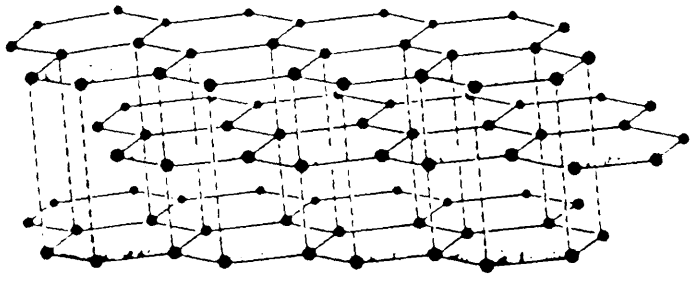

Figure 1.2

Hexagonal form of graphite.

structure and is formed on mechanical treatment (Bacon, 1952(a)) but reverts to the hexagonal form on heat treatment (Boehm and Coughlin, 1964) and chemical treatment (Laidler and Taylor, 1940 ; Lukesh, 1951(a) and (b)).

1.1.2 Non-Ideal Crystal Characteristics

In graphite crystals, there are two common defects that can be found. One is a stacking disorder which may arise from deviations from the ideal relative position between carbon layers. The other type of defect is a disruption of the carbon plane.

1.1.2.(a) Stacking Disorder

A stacking disorder occurs when the carbon layer planes no longer conform to an ABAB... or ABCABC... type stacking sequence. The degree of such a disorder in graphite affects the interlayer spacing of the carbon planes (Franklin, 1951; Bacon, 1950, 1951, 1952 and 1958). A material containing such a defect still possesses two dimensional crystallinity and a certain degree of parallelism of the layer planes. Such material is often denoted as turbostratic although use of this term is discouraged by I.U.P.A.C. Stacking disorder can also be produced when perfect dislocations dissociate into partials with fractional Burgers vectors. The defect then occurs in the region between the partials (Read, 1953 ; Friedel, 1964).

1.1.2.(b) Layer Defects

The disruption from their planar aromatic state, of the carbon layer planes is a second common disorder in graphite structure and is known as a layer defect. The disorder can be caused by the formation of a hole defect (Ubbelohde, 1957 ; Ubbelohde and Lewis, 1960), as a result of irradiation, which displaces atoms forming interstitials (Bollmann, 1960, 1961(a), (b) and (c)) or by the presence of twin planes, produced by tilting of the carbon layers (Lukesh, 1950 ; Baker et al., 1965). Another way in which such defects can be produced is by the formation of bonds with impurity atoms and by the presence of intercalated atoms (Heerschap et al., 1964).

1.1.3 Electronic Structure of Graphite

In the graphitic plane, each carbon atom is bound to its three nearest neighbours by equivalent σ bonds, which as previously mentioned, are localised corresponding to an sp^2 hybridisation of the atomic orbitals. Of the four valence electrons possessed by each carbon atom, three are involved in this type of covalent bonding. The remaining electron is delocalised over the carbon plane in the π orbital system.

As the interlayer spacing is relatively distant in comparison with the interatomic distance within a carbon plane, the interaction between the layers may be neglected and the electronic structure of graphite may then be treated as a two dimensional problem. It was initially

suggested by Coulson (1947) and Wallace (1947) that the π bond could be considered as a filled valence band and an empty conduction band. Later, work by Coulson and Taylor (1952) and McClure (1959) described these conduction and valence bands as just touching or narrowly overlapping at the corners of the Brillouin zone.

Resulting from work by Slonczewski and Weiss (1958), who included in their calculations the perturbation of the interlayer interactions, graphite is now regarded as a semi-metal. This is a structure which consists of small isolated pockets of holes in the valence band and an equal quantity of pockets of electrons in the conduction band. The semi-metal characteristics of graphite, which unlike a semi-conductor, has a small but finite overlap of the valence and conduction bands, results in its high electrical conductivity. The electronic structure and Fermi surface of graphite have been studied extensively and reviewed by Haering and Mrozowski (1960) and Cracknel (1969) with a more recent mathematical treatment by Charlier and Charlier (1987).

1.2 Active Carbon

1.2.1 Structure of Active Carbon

Active carbons are porous adsorbents, principally of biological origin. Their most important property is a very great ability for adsorbing vapours and gases due to their highly developed porous structure. They are made from

organic starting materials such as nutshells (especially coconut and almonds), wood, coal, fruit stones and peat as well as synthetic polymers such as PVC and Saran. These substances are burned with the exclusion of air in order to produce a carbonaceous resin. At this point the material is still not particularly active. The porosity must be further developed, for example, by heating it in a stream of carbon dioxide or steam.

The structure of these active carbons, as with all disordered carbons e.g. cokes, chars, carbon blacks etc. is based to a greater or lesser extent on the graphite structure.

The X-ray diffraction spectra of all disordered carbons show two common features. They contain (001) peaks which result from the parallel stacking of layer planes and peaks of the type (hk) which reflect a two dimensional regular structure within the individual layer plane segments (Fischbach, 1971). The fact that (hkl) type peaks are absent illustrates that there is little or no stacking order of the parallel layer planes.

From these characteristics, Warren (1941) formulated the turbostratic model. In this model, disordered carbon atoms are considered to exist as parallel stacks of graphitic layer planes. The layers are however, displaced from the typical ABAB... stacking sequence by small translations in a direction parallel to the plane or by a rotation about the c-axis (normal to the plane). This displacement from

the equilibrium stacking relationship results in an increased mean interlayer spacing due to the reduction of the van der Waals bonding.

This model has been further studied and developments have been made (Biscoe and Warren, 1942; Houska and Warren, 1954; Warren, 1956; Warren and Bodenstein, 1965, 1966; Franklin, 1950, 1951(a) and (b); Bacon, 1950, 1951, 1952, 1954, 1958). During this time, Franklin also introduced the notion of disorganised carbon and single layers, disorganised carbon being single or small clusters of carbon atoms which do not exist as part of a graphitic layer. Another point to arise as the model was revised was that in order to understand disordered carbon, layer plane defects as well as stacking disorder had to be considered.

Mering and Maire (1960) pointed out some of the failings of the turbostratic model and went on to propose a model based on the properties of imperfect layer planes rather than perfect layers in a disordered arrangement (Maire and Mering, 1970). In this model they considered the presence of "interstitial" carbon atoms firmly attached to each side of the layer planes. These atoms being the cause of lattice distortion and thus of the increase in the interlayer spacing. The fact that carbons with similar amounts of structural disorder display differing graphitisation behaviour could then be explained by varying concentrations of interstitial atoms (Schiller et al., 1967(a) and (b)). The transition from a random to an ordered arrangement of the interstitials relative to the

hexagonal layers to which they are attached, followed by removal of the defects from first one side and then the other, was used to explain the difference between the graphitic structure and the highly disordered carbon structure.This difference being spanned by four distinct phases, the ordered ABAB... stacking sequence being formed on removal of all the interstitial imperfections. Although Mering and his fellow workers have provided physical, structural and chemical evidence in support of this model, it would seem unlikely that such a simple model could sufficiently describe the highly complex structure of disordered carbons. Two problems associated with this model are that it assumes the presence of only one specific type of imperfection of the structure and that the work was only carried out on polyvinyl chloride samples and conventional pitch cokes. Its applicability to a wider range of carbons was not tested. Mering also noted that the bound interstitals differed from the mobile interstitial carbon atoms produced from irradiation damage. This model, even with its problems, still has many features relevant to the structure of real carbons.

Pauling (1966) proposed a model for the disordered structure based on bonding. It has been generally accepted that the bonding within a layer plane is composed of three identical single bonds and one resonating bond associated with each atom. Pauling suggests that this is the bonding state in turbostratic carbon. However, for graphite he suggests a quinoid structure, possessing two single bonds and a third double bond per atom. There will therefore be

a large out of plane bulge associated with the double bond. Coincidence of these bulges with the open hexagon centres of adjacent layers would result in enhancement of the van der Waals bonding and an ABAB... type stacking sequence. Transformation of the resonating bond to quinoid structure could then be considered the graphitisation process. Pauling noted that X-ray diffraction, magnetic susceptibility and layer plane compressibility are consistent with this model. A problem associated with this model however is that a quinoid structure would result in an orthorhombic crystal structure with two distinct interatomic distance values within the layer planes. The relative displacement of the layers would also differ from that of a hexagonal structure. Ergun (1968(a)) argued against this model but concluded that the evidence was inconclusive on the existence of a quinoid structure in graphite. Ergun has also reviewed the simple turbostratic model and commented on its inadequacies (Ergun 1968(a) and (b); Ergun and Gifford, 1968, 1969).

The importance of both individual and clusters of carbon atoms, "cross-link" or distorted carbon-carbon bonds and holes in layer planes have all been emphasized by Ruland (Ruland, 1964, 1965(a) and (b), 1967(a) and (b), 1968; Perret and Ruland, 1968, 1969). Layer curvature has also been shown to be of importance (Woodruff, 1969).

The existence of a good linear relationship with relatively little scatter between the mean interlayer spacing and the mean square displacement of adjacent

layers parallel to the layers has been shown by Ruland. He has also shown that the r.m.s. displacement of adjacent layers normal to the layers decreases as the mean interlayer spacing decreases. The scatter band however, is very broad and the values of the r.m.s. displacement of adjacent layers normal to the layers are in general significantly larger than the differences between the mean and minimum interlayer spacings. A final point that he noted was that as the mean interlayer spacing falls below 0.338 nm, the incidence of rhombohedral stacking drops sharply, but is still significant in moderately well graphitised material.

Some important points emerge from these statements. The first shows that there is no fundamental basis for the mean interlayer spacing of 0.344 nm that is traditionally associated with random parallel layer stacking. There is however, evidence for differences in the defect structure of different carbons with the same mean interlayer spacings. The increased interplanar distances of disordered carbon must result largely from defects rather than from stacking disorder, as shown by Ruland's second point. Ruland suggests that graphitisation occurs by the annealing out of defects as with the Mering model. He does however, acknowledge the importance of a variety of types of defect both within and between the layers.

From the traditional parameters used in the description of turbostratic carbon only the mean interlayer spacing seems to have survived in the many new models that have been

developed. It now however, seems likely that a significant proportion of the interlayer spacing increase in disordered carbons arises from defects within and between the layers (Maire et al. 1968).

With the advent of these newer models, parameters such as L_a and L_c have been questioned and/or replaced by other parameters. The apparent layer diameter L_a has been shown to have numerous correlations with other structural or physical property values. For this reason its interpretation is of particular importance. For some time, it has been questioned as to whether L_a corresponds to the actual dimensions of the layer structure and it is now generally accepted that the measured value of L_a is appreciably smaller than the average diameter of the layer planes. This is due to the fact that effectively, L_a is a measure of the average size of planar, defect free regions. Thus, even although the extent of the imperfect layer structure may be large, layers that are bent or contain holes will give smaller values of L_a. In order to find the true layer size a variety of X-ray techniques have been developed (Bouraoui and Mering, 1964; Eeles and Wilson, 1965), although they are extremely difficult to employ. L_a values are probably best interpreted as an indication of the relative flatness and perfection of the layers, rather than as real crystallite layer diameters. The actual extent of the defective layer structure is however, very important and may be the fundamental basis for distinguishing between graphitizing and non-graphitizing carbons. For the case of non-graphitizing

carbons, the layer segments are small (Perret and Ruland, 1968; Schiller et al. 1967) however, graphitizing carbons appear to possess an extensively developed layer structure (Ergun, 1968(a)).

1.2.2 Porous Structure

Active carbons are extremely porous materials and the size and structure of the pores can vary greatly, both for a given solid and from one solid to another. The pores are characterised by their widths, i.e. the diameter of a cylindrical pore or the distance between the walls of a slit pore. A method of pore classification that has been much used is that of Dubinin (1975), where pores whose radii exceed 100-200 nm are defined as macropores and those with radii in the range 1.8-1.9 nm to 100-200 nm as mesopores (or transitional pores). The final group of pores, micropores are subdivided into two groups by Dubinin. Micropores proper, have radii less than 0.6-0.7 nm and those pores in the range 0.6-0.7 to 1.5-1.6 nm are denoted as supermicropores.

More recently, I.U.P.A.C. (1985) have suggested a set of values for pore classification to alleviate the confusion within the literature. Pores are classified in the following manner: Pores of widths exceeding 50 nm are called macropores, those with widths 2 nm to 50 nm are called mesopores and those pores whose widths do not exceed 2 nm are micropores. These boundaries between the pore types are not arbitrary but reflect the different

pore filling mechanisms that occur within these various size groupings. It is this method of pore classification that has been employed in the present work.

1.2.2(a) Macropores

These, the largest of the pore types, may be studied by optical microscopy or more commonly by mercury porosimitry- a technique whereby mercury is forced into the pores, the pressure to do so being related to the radius of the pores by:

$$P = (2\gamma/r)\cos\phi \qquad (1.1)$$

where P is the hydrostatic pressure necessary to fill pores of radius r (supposed to be cylindrical).γ is the surface tension of mercury (480 dyn cm^{-1} at 293K) and ϕ is the contact angle (around 140° for typical solids (Stoeckli, 1976)). This technique is applicable for pores up to around 10^3 to 10^4 nm in radius.

The macropores of an active carbon act as transport pores, allowing adsorptive molecules to enter the smaller pores situated within a particle of carbon. These pores are unimportant from the point of view of the adsorption that takes place on them as their surface area is very small. However, their importance lies in the fact that they affect the rate of diffusion into the meso- and micropores.

1.2.2(b) **Mesopores**

The lower limit of the width of these pores corresponds to the smallest pores in which capillary condensation may take place and the upper limit corresponds to the limit within which one may use accurately, the results furnished by the adsorption isotherm. Capillary condensation is a function of the pore radius and is characterised by a hysteresis loop in the adsorption-desorption branches of the isotherm.

Capillary condensation occurs because the vapour pressure of liquid, p, above a concave meniscus formed by a liquid is lower than the saturation pressure p_o above a plane surface of the same liquid. This means that a gas or vapour adsorbed at a pressure p_a, will not be desorbed until a lower pressure p_d is reached (figure 1.3). p_d and p_o are related by the Kelvin equation, valid for a capillary of circular cross-section (Gregg and Sing, 1967).

$$\ln p_d/p_o = -(2\gamma V_m/r_k RT)\cos\phi \qquad (1.2)$$

where p_d is the desorption pressure, p_o the saturation pressure of the liquid at temp T, γ the surface tension of the adsorbate in the liquid state, V_m the molar volume of the liquid, r_k the Kelvin radius, R the gas constant and ϕ the contact angle.

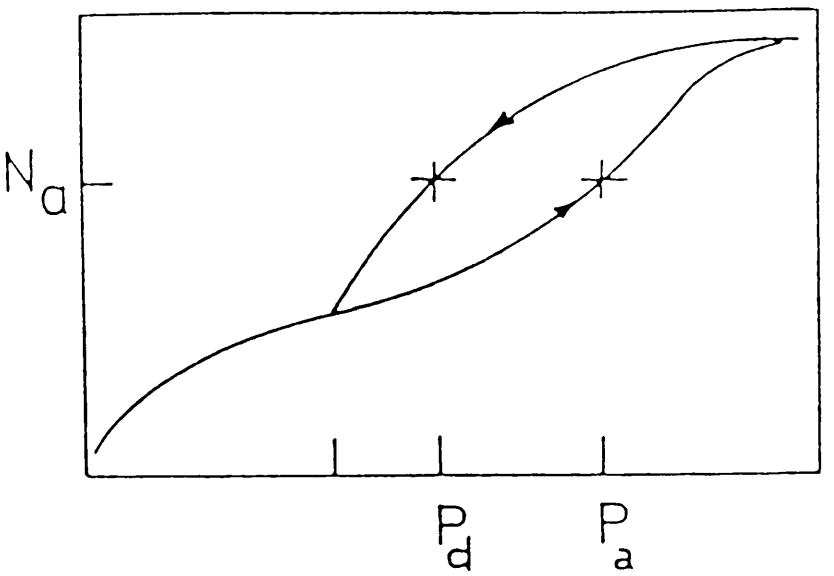

Figure 1.3

Adsorption by mesopores (capillary condensation).

The relationship between the effective radius of the pore r_p and the Kelvin radius is given by (Kraehenbuehl, 1983):

$$r_p = r_k + t \qquad (1.3)$$

t being the thickness of the layer normally adsorbed on the pore walls at pressure p_d.

The mesopores, which branch off from the macropores, as well as acting as pores where capillary condensation takes place, serve as passages to the micropores for the adsorbate.

1.2.2(c) **Micropores**

These comprise of all cavities of molecular dimensions in which volume filling of pores occurs (T.V.F.M. of Dubinin, 1975) rather than capillary condensation. These may be spaces between the ordered regions of a sample or even spaces between the layer planes within the sample. These pores may be studied by adsorption and immersion techniques, transmission electron microscopy and small angle scattering of X-rays. Some of these methods will be described in greater detail in later chapters.

The micropores, although smallest in pore size, constitute the largest part of the internal surface and therefore most of the adsorption occurs within them. In fact, for typical active carbons, the micropores constitute at least 90% of the apparent surface area.

1.2.3 History and Utilisation

The high capacity for adsorption possessed by active carbon has made it an extremely important material. As early as 1777, Fontana had discovered the adsorptive properties of charcoal and Scheel (1780) had found that charcoal which expelled gas on heating, readsorbed it on cooling. In the nineteenth century de Saussure (1814) and Mitscherlich (1843) began the formulation of views on the importance of both exposed surface area and pore volume in relation to the gas adsorbing properties of carbons.

Active carbon made early laboratory appearances in the production of high vacuum (Tait and Dewar, 1874(a) and (b)) and in the separation of nobel gases from air (Ramsey, 1905, 1908). Industrially, the first applications of the substance were more concerned with its behaviour towards liquid systems rather than its gas adsorbing properties. In fact, the decolourisation of sugar required vast quantities of carbon, therefore much development on active carbon production was undertaken (Valter, 1970).

The utilisation of poison gas during World War I gave a new momentum to the production and study of adsorbents for use in gas masks and much was learned about the technology of adsorptive carbons (Dacey, 1967). With the advent of World War II again an intensive study was undertaken. Although toxic gas was never used during this period, the development of new and more deadly agents meant that the development of more advanced respirators was necessary to

combat them.

Today such applications as air purification (Kahle, 1953, 1954), volatile solvent recovery (Rowe, 1964), deoderisation (McDowell, 1961) and the treatment of drinking water (Hyndshaw, 1965) make active carbon an important material.

The food industry makes use of carbons in certain operations, e.g. treatment of spirits and wines (Williams and Fallin, 1943) as well as beers (Kaiser, 1957). It is also used for bleaching oils and fats during their refinement (Anderson, 1953).

For the chemical industry, active carbon is a very important substance due to its uses both as a catalyst and catalyst support (Trapnell, 1955; Chaney et al., 1950). Its properties also make it important in chromatographic techniques.

Active carbon has many medicinal applications, such as for use in the treatment of infections of the digestive system. It is very effective in the treatment of poisoning, particularly by mushrooms, spoiled foodstuff (botulism), alkaloids (e.g. strychnine), metals and phenol. It is commonly used when the nature of the poison is unknown due to its almost universal applicability. Such carbons however, must conform to very strict requirements.

A final interesting application of carbon is its utilisation in the nuclear industry. In nuclear reactors, the production of nuclear fuel elements and the processing of spent fuel elements, it is essential that a thorough purification of circulating and exhaust gas is undertaken both from the point of view of safety and for the efficient operation of the process (Robinson Jr., 1961). Active carbon is generally used for the removal of these substances when they are relatively inactive chemically (Lehmer, 1960). As well as being used within the actual nuclear process, active carbon is also used as a filter in the emergency ventilation system for reactor buildings.

These applications are among some of the most important uses of active carbon but they are by no means the only ones. Active carbon is a very versatile material.

1.2.4 Carbonisation and Activation

Active carbons are produced from carbonaceous materials using one of two methods. The first of these is a two step process, consisting of a carbonisation reaction followed by activation. During the carbonisation stage, where the sample is heated with the exclusion of air, most of the non-carbon elements (mainly hydrogen and oxygen) are eliminated in a gaseous form. Graphitic sheets of very small dimensions are then formed from the carbon atoms which are freed during this process. The arrangement between these graphitic regions is not regular and while they are being formed, tarry substances are also produced

in the areas between them. Following this step is a process known as "physical" activation, whereby the porous structure is developed by removal of the tarry products. This is achieved by reacting the material with an oxidising gas (e.g. carbon dioxide, oxygen or steam) at high temperature. After the blocked pores have been cleared and the graphitic layers exposed, the action of the gas is to attack these layers. The reaction rate however, must vary from one area of the sample to another or no new porous structure would be developed. This is thought to be because the graphitic regions burn out faster in a direction parallel to the plane of the carbon layers than in the direction perpendicular to them (Grisdale, 1953). Therefore, the ordered regions will burn out at different rates depending on their relative orientation to the area where the activating gas is attacking (Dannenberg and Boonstra, 1955).

The second method employed to produce active carbon is a technique called "chemical" activation. This process is carried out in a single step. Substances such as $ZnCl_2$ or K_2S are added to the starting material and carbonisation and activation are then carried out together by heating the sample. The inorganic compounds prevent tarry substances being formed on a large scale. The resulting active carbon must then be washed however, to remove the activating material. Carbon produced in this manner may be further activated, if required, by using a gaseous reagent in a similar way as in "physical" activation. In the present work, the carbons were activated using the

"physical" activation process and therefore the following discussion will relate to that method of preparation.

The degree to which an active carbon has been activated is gauged by a quantity known as burn-off, which is a measure of the percentage weight decrease of the sample during activation.

$$\text{BURN-OFF}(\%) = (1-m_f/m_i).100 \qquad (1.4)$$

where m_i and m_f are the masses of the carbon before and after activation respectively.

Much attention has been paid to the reactions of gas with carbon, not just because of the production of active carbon but also because carbon is used for the construction of items such as rocket nozzles and as a moderating material in nuclear reactors, where a lack of knowledge of the gas reactions involved could cause serious problems. Some of these reactions have been reviewed by Walker et al. (1959).

In the present study activation was carried out using carbon dioxide at 850°C. The reaction between carbon and carbon dioxide is an endothermic process (heat of reaction $\Delta H(1000K) = +170.7 kJmol^{-1}$ (Kapteijn and Moulijn, 1986)). This effect can be observed from the temperature drop that occurs in the system when the activation reaction has begun.

The rate of the carbon-carbon dioxide reaction is generally agreed (Gadsby et al., 1948; Lewis et al., 1949; Marsh, 1951; Reif, 1952(b)) to take the form:

$$\text{Rate} = \frac{k_1 P_{CO_2}}{1 + k_2 P_{CO} + k_3 P_{CO_2}} \qquad (1.5)$$

where P_{CO_2} and P_{CO} are the partial pressures of carbon dioxide and carbon monoxide and k_1, k_2 and k_3 are empirically determined rate constants.

There are two proposed reaction mechanisms fitting this rate expression which can be simplified to the form shown here. One has been suggested by Reif (1952(a)) and Ergun (1956) and takes the form:

$$\begin{aligned} C_f + CO_2 &\rightleftharpoons C(O) + CO \\ C(O) &\rightarrow CO + C_f \end{aligned} \qquad (1.6)$$

The other mechanism was proposed by Gadsby et al. (1948) and is of the form:

$$\begin{aligned} C_f + CO_2 &\rightarrow C(O) + CO \\ C(O) &\rightarrow CO + C_f \\ C_f + CO &\rightleftharpoons C(CO) \end{aligned} \qquad (1.7)$$

Where the subscript f denotes an active site and terms in parenthesis represent adsorbed species.

Both of these mechanisms begin with the dissociation of a carbon dioxide molecule and the formation of a solid carbon-oxygen complex. The actual removal of carbon occurs in the second step, with the removal of the carbon-oxygen complex from the body of carbon to form carbon dioxide and leave a new active site behind.

Many authors have claimed that carbon monoxide has an inhibiting effect on the carbon-carbon dioxide reaction (Gadsby et al., 1948; Reif, 1952(a); Ergun, 1956, 1965; Laine et al., 1963). The basic difference in the two schemes shown above is the way in which they account for this effect. In the first model, the reverse reaction of the first step is considered to be significant. Thus, the effect of the presence of carbon monoxide is to displace the reaction equilibrium to the left. In the second model however, this reverse reaction is thought to be negligible and the inhibiting effect of carbon monoxide is explained by the addition of a third step which shows that active sites are blocked by the adsorption of carbon monoxide molecules.

Much discussion has taken place as to which of these reaction mechanisms is correct, however from experimental results it is still not possible to discriminate between them (Walker Jr. et al., 1959).

1.2.5 Previous Studies

Carbon porosity has been studied using a wide range of techniques such as gas adsorption, immersion calorimetry, electron microscopy, small angle X-ray diffraction, mercury porosimetry and gas chromatography.

Using combinations of small angle X-ray diffraction, adsorption analysis and immersion calorimetry with molecular probes, consistency of results has been shown for the micropore sizes in certain carbons (Stoeckli, 1979, 1980; Stoeckli and Huber, 1977; Janosi and Stoeckli, 1979, Dubinin and Stoeckli, 1980).

Electron microscopy was initially used in the study of crysotile asbestos fibre to produce a correlation between the pore sizes resulting from it and those determined from gas adsorption data (Scholten et al., 1973, 1975; Scholten and DeWit, 1975). However, the pores involved here were of a relatively large size (2-6 nm). When carbon was studied, initially attention was paid to the meso- and macropores only (Fryer, 1970, 1974; Baird and Fryer, 1974) as observation of micropores was limited by the resolution of the microscope. The imaging of lattice fringes in graphite (Baird et al., 1971; Millward and Jefferson, 1978) and in disordered carbons (Ban et al., 1975) led to observations of some microporous structure. With improved instrumentation and a clearer understanding of microscopical techniques it became possible to study the

structure of microporous samples by high resolution electron microscopy (HREM) and make direct measurements of micropore sizes (Fryer, 1979, 1981; Evans and Marsh, 1979).

As an alternative to HREM, it is also possible to utilise the dark field technique of Oberlin (Oberlin et al., 1974), whereby well defined information is obtained on d_{002}, the spacing between the aromatic sheets of carbonaceous material.

1.2.6 Aim of the Present Work

The present work was carried out on a series of carbons produced in the laboratory by activating a charcoal precursor to varying degrees. The aim of this study was to examine the porous structure and particularly the micropore size distribution of this carbon series using some of the techniques mentioned above, especially HREM and immersion calorimetry.

Immersion calorimetry is a macrotechnique from which the average pore size distribution can be deduced. In comparison HREM reveals the structure of individual pores but, of course, is less statistically representative. The comparison of these two techniques used on the same carbons, should show complementary information on the micropore structure, as well as a commentary on the two techniques.

ELECTRON MICROSCOPY

2.1 Introduction

The development of the wave-particle duality theory (de Broglie, 1924) and of wave mechanics (Schrödinger, 1926) suggested that the wavelength of an electron would be less than that associated with light and therefore the construction of an electron microscope should provide an instrument of higher resolving power than that of a light microscope. X-rays are also of a lower wavelength than light, however, being uncharged unlike electrons, they cannot be focussed with the magnetic or electrostatic lenses employed in electron microscopy. Another advantage of using a beam of electrons to image a sample is the fact that the wavelength associated with the electrons can be varied vastly. The wavelength associated with an electron accelerated through a potential of 100kV is 0.0037nm whereas if a potential of 1MV is utilised, a wavelength of 0.00037nm is obtained.

The first electron microscope was built by Knoll and Ruska in 1931 (Knoll and Ruska, 1932) who later in 1933 went on to construct an instrument capable of resolving 0.05μm. From this point in time attempts have been made to create more and more powerful microscopes. There have been many reviews, both on the theories of electron optics and on instrumental development (Zworykin et al., 1945; Hillier and Vance, 1945; Cosslett, 1951, 1970, 1981; Hall, 1953; Hirsch et al., 1965). Electron microscopes available

today, for suitable specimens, are capable of resolving atoms and atom clusters (Hall and Hines, 1970; Murata et al.,1976; Iijima, 1977; Fryer, 1983; Smith et al.,1983).

With modern day electron microscopes, in addition to the normal bright field mode of operation which will be described in more detail later, there are other special modes of operation. The dark field mode is a technique whereby the unscattered electrons are removed by a physical aperture leading to an image of high contrast but diminished intensity. The objective aperture may be used to allow the passage of scattered electrons resulting from a specific reflection to form an off-axis dark field image. This means that the illumination in the resulting image arises purely from the reflection that had been chosen. The off-axis electrons which are scattered through large angles are subject to larger aberrations due to lens defects thus resulting in an image of poor quality. However, in modern microscopes, the incident beam may be tilted at a chosen angle allowing the selected scattered beam to be transmitted axially through the objective aperture resulting in the formation of an axial dark field image. Since such a technique minimises the effect of aberrations, high resolution dark field images may be obtained. Aspects of dark field imaging, in relation to the structure of thin crystals have been discussed by Hirsch et al. (1965). A similar technique is that of tilted bright field imaging. The theory of image formation using this method has been presented by Howie et al. (1973); Ast et al. (1974) and Krivanek and Howie (1975).

The technique has been applied to both lattice imaging (Komoda, 1966) and to study short range order in amorphous material (Rudee and Howie, 1972; Krakov et al., 1976). To use the tilted bright field method to resolve lattice fringes, the incident electron beam is tilted such that the undeviated beam and the Bragg reflected beam specific to the lattices, subtend equal angles at the optic axis. An aperture is inserted in the back focal plane of the objective lens so that the image is composed from these two beams. The symmetric arrangement of the beams means that the effects of the objective lens spherical aberration and chromatic aberration are minimised. However, in such a mode, the contrast effects resulting from inelastically scattered electrons can be significant (Parsons and Hoelke, 1974) thus complicating image interpretation.

A method of improving the resolution available from an electron microscope is to increase the accelerating voltage, thereby reducing the electron wavelength. Dupouy and Perrier (1962) and Cosslett (1969) outlined the advantages of high voltage electron microscopy. As the energy of incident electrons increases, the penetration of the electrons through the sample also increases, therefore useful information may be obtained for samples that are too thick to be studied by 100kV microscopy. As there is less interaction of the electron beam with the specimen in high voltage microscopy, less radiation damage will occur, although this improvement is not linear (Kobayashi and Sakaoku, 1965; Kobayashi and O'Hara, 1966) and the

probability of nuclear displacement increases. High voltage microscopes such as the 600kV instrument at Cambridge University (Nixon et al., 1977) have achieved lattice resolution of less than 0.1nm. The instrument employed in the present work was a JEOL 1200EX electron microscope with an accelerating voltage of 120kV. This equipment routinely gives a resolution of better that 0.3nm. The microscope was used in the bright field mode therefore a more detailed discussion on such a method will ensue.

2.2 Construction of the Microscope

The basic structural feature of an electron microscope are shown in figure 2.1. The electrons are generated from a source within the electron gun. Ideally, this source would produce a coherent beam of monochromatic electrons, however in practice this is not possible. In general, the electron source is a thin tungsten hairpin filament which is heated electrically. Such a filament is employed due to its high melting point, low vapour pressure and high mechanical strength. The brightness available from such an electron source may be improved upon by using a pointed tungsten filament (Wolf and Joy, 1971) although such a piece of apparatus must be carefully aligned. Other sources of electrons are lanthanum hexaboride (LaB_6) cathodes (Ahmed, 1971) which give a great increase in both coherence and brightness as well as a greater filament lifetime, and field emission cathodes (Crewe et al., 1968) which are also of superior quality. However, field

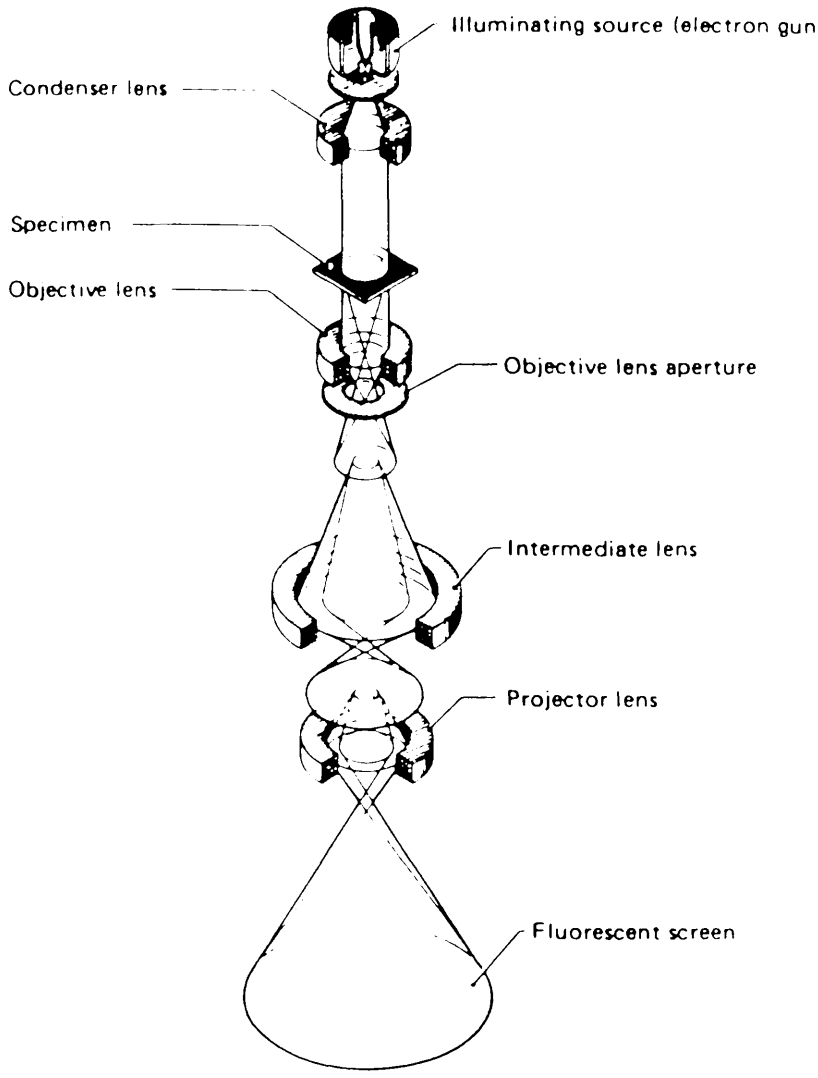

Figure 2.1

Basic structural design of a transmission electron microscope.

emission guns require extremely high vacuum and are very expensive.

From the electron gun the electron beam is accelerated through a potential of many thousands of volts, the exact value depending on the type of microscope and its mode of operation. It is then brought to a focus on the sample by the condenser lens system. For high resolution work the condenser system generally consists of two electromagnetic condenser lenses. The first of these lenses produces a highly demagnified image of the electron source, which is projected onto the surface of the specimen by the second of the lenses. This results in a very small minimum spot size and thus vastly increased brightness concentrated over a small area. In addition to the lenses, the condenser system also possesses a fixed and a variable aperture which allow control of the angular convergence of the beam on the specimen.

The objective lens focuses the electrons that are scattered by the specimen and as it magnifies the electron beam and transmits it to the remaining lens systems its performance is crucial to the overall performance of the microscope. In light microscopy, individual lens defects may be corrected by using a series of convergent and divergent lenses. However, unlike optical glass lenses, electromagnetic lenses are always convergent and thus lens defects in the electron microscope can not be compensated for in an analogous manner. Therefore, in electron

microscopy, the lenses must be manufactured to an extremely high quality, especially the objective lens in view of its critical position in the lens system. The scattered electrons within the microscope travel close to the optic axis, therefore aberrations such as coma and distortion are not of great importance. However, as a magnetic lens field is not sherically symmetric, spherical aberration is an important lens defect. The objective lens system also contains electromagnetic stigmator lenses to compensate for the effects of astigmatism. In the back focal plane of the objective lens, the objective aperture is situated. This device is used to limit the quantity of scattered electrons reaching the recording device as any electrons scattered to a greater angle than that subtended by the aperture will be unable to contribute to the final image.

The remaining lens systems, the intermediate and projector lenses, further magnify the image produced by the objective lens resulting in a range of possible magnifications of up to one million times. The final image is generally produced on a fluorescent screen or image intensifying camera or for a more permanent and detailed record, a photographic plate can be used.

2.3 Electron Scattering

When an electron beam passes through a substance it is scattered due to Coulomb interactions. These electrons may be affected in a variety of ways. They may be changed into

transmitted electrons, backscattered electrons or adsorbed electrons by their interaction with the specimen. It is the transmitted electrons that are of importance in electron microscopy and this category can be classified into three types. There are the directly transmitted electrons which pass through the sample with little change to their wavelength or direction, elastically scattered electrons which undergo a directional change but retain their energy and inelastically scattered electrons which undergo both a change of direction and a partial loss of energy.

Elastic scattering occurs when there is an interaction between the incident electrons and the atomic nuclei within the specimen resulting in deflection of the electrons with no loss of their energy. In crystalline specimens, this scattering obeys the Bragg relationship. The elastic scattering of electrons is increased as the atomic number or thickness of the specimen increases. If the electrons are scattered at very large angles to the optical axis they will be stopped by the microscope column and thus will not contribute to the final image. The insertion of an objective aperture results in a similar condition, with those electrons interrupted by the aperture failing to contribute to the image. This process results in contrast in the image as, those electrons deriving from high scattering areas of the sample will appear dark, and is known as amplitude contrast or for periodic samples, diffraction contrast. The degree of such contrast can be controlled by the size of the objective

aperture that is utilised. This type of contrast, in general, is only important at low to medium resolution.

Inelastic scattering occurs when the incident electrons interact with the orbital electrons of the sample. This results in only a small deflection of the electrons but they loose some energy in the process and hence their wavelength is changed. These inelastically scattered electrons may recombine with either the transmitted electrons or the elastically scattered ones resulting in either increased or diminished regions of contrast in the final image. This phenomenon only becomes visible at slightly out of focus conditions and is known as inelastic phase contrast. A similar process may occur for the elastically scattered electrons provided they are allowed to pass through the objective aperture. Again the amplitude in the image contrast may be increased or diminished if suitable focus conditions are selected to allow recombination with the undeviated beam of electrons.

If the specimen contains a crystalline structure with a set of lattice planes oriented parallel to the beam direction, then recombination of the electrons scattered elastically by this specimen may result in a periodicity in the image that is related to that of the sample. This type of imaging is only applicable for images that are normal to the electron beam and is the basis of "lattice imaging" in high resolution electron microscopy. Samples containing small periodicities will elastically scatter the electrons at large angles. Provided a sufficiently

large objective aperture is used, these electrons will be transmitted. However, they will travel in areas distant to the optical axis of the objective lens and will thus be subject to lens aberrations which severely affect the phase contrast image retrieval and interpretation.

The interpretation of elastic and inelastic phase contrast effects can only be carried out with relative ease for thin specimens (less than 10nm). Electrons passing through thin specimens can be considered to undergo only a single scattering event and thus they conform to kinematic approximations (Whelan, 1959; Hirsch et al., 1965). Kinematical theory should only be considered an approximation, in reality multiple scattering of electrons does occur and a more accurate theory has been developed to account for the scattered amplitudes and phases resulting from this situation (Cowley and Moodie, 1957).

2.4 Phase Contrast

To obtain contrast at higher resolution than that obtained from diffraction contrast, elastically scattered electron beams are recombined and the phase difference between them enhanced by defocussing the objective lens. The inelastically scattered electrons will also undergo some phase recombination, however the defocus value for which this is significant is far removed from that required for the elastically scattered electrons (Misell, 1976).

The electrons, scattered elastically through a variety of Bragg angles by the specimen, form a diffraction pattern in the back focal plane of the objective lens. This Frauenhoffer diffraction pattern corresponds mathematically to a Fourier transform of the object expressed in terms of spatial frequency, areas of which may be removed by insertion of the objective apertures. In order to obtain the final image, the diffraction pattern undergoes a further Fourier transform to the image plane which is then further magnified by the remaining lens systems of the microscope. The photographic plate records the intensity distribution, therefore if multiple scattering has occurred in the object this will be visible in the image as changes in contrast. This contrast reflects phase differences caused by multiple scattering in the object rather than structural features of the object. For this reason it is apparent that the image of a thick specimen does not reflect the structure of that specimen.

Scherzer (1949) considered the theoretical resolution limit of the transmission electron microscope and derived a wave mechanical formulation of image formation which took account of how the incident electron wave interacts with the specimen and how the resulting wave is transformed to the image plane by the electron optical system. This is the basis for the idealised linear transfer theory of electron microscopy, the limiting case of the more rigorous dynamical approach (Cowley and Moodie, 1957). This theory may be applied provided the

specimen can be regarded as a weak phase object (Grinton and Cowley, 1971; Lynch and O'Keefe, 1972), single scattering conditions apply and scattered wave amplitudes are considered to be much smaller than those of the primary wave. Such assumption may only be made for a thin specimen of less than around 10nm.

The image contrast can be quantitatively explained by considering the amplitude of the elastically scattered electrons as they pass through the specimen to form a diffraction pattern in the back focal plane of the objective lens. These beams are then combined, allowing for phase modulations induced by the specimen and the objective lens defects to form an amplitude distribution in the image plane. The amplitude distribution is then represented on the screen as an intensity distribution.

In mathematical terms the image formation in the objective lens can be presented as a two-dimensional projection (xy) that initially gives an amplitude distribution (diffraction pattern) in the back focal plane of the objective lens and this is expressed by (Cowley, 1975; Erickson, 1973):

$$\Psi_{(uv)} = F\,[e^{-i\sigma\phi}(xy)] \qquad (2.1)$$

where σ is the interaction constant, $\phi_{(xy)}$ is the projection of the potential distribution of the specimen in the beam direction, F is the Fourier transform operation and e and i have their usual mathematical

significance. The co-ordinates u and v are reciprocal space co-ordinates in that $u = x/f\lambda$ and $v = y/f\lambda$, where f is the focal length of the lens and λ is the wavelength of the electron beam.

Magnetic lenses are not perfect and because of this the electrical and mechanical defects are allowed for by the introduction of a phase modulator, $\chi_{(uv)}$. The major factor contributing to $\chi_{(uv)}$ is spherical aberration. Equation 2.1 now becomes:

$$\Psi_{(uv)} = F\,[e^{i\sigma\phi}(xy)]e^{i\chi}(uv) \qquad (2.2)$$

As the objective aperture is situated in the back focal plane of the objective lens, an aperture function $A_{(uv)}$ must also be inserted. This function has a value of one inside the aperture and zero elsewhere. The wave function now takes the form:

$$\Psi_{(uv)} = F\,[e^{-i\sigma\phi}(xy)]e^{i\chi}(uv)A_{(uv)} \qquad (2.3)$$

When only one scattering event takes place per electron passing through a specimen, i.e. a thin specimen, the resultant amplitude distribution in the back focal plane of the objective lens is the sum of transmitted unscattered beam $\delta_{(uv)}$, and the elastically scattered beam represented by equation 2.3. This results in:

$$\Psi_{(uv)}\text{total} = \delta_{(uv)} + [\sigma\phi_{(xy)}\sin\chi_{(uv)} - i\sigma\phi_{(xy)}\cos\chi_{(uv)}]A_{(uv)} \qquad (2.4)$$

A second, inverse Fourier transform of 2.4 corresponds to the image plane and gives rise to the resultant amplitude distribution at the image plane (i.e. real space, xy):

$$\Psi_{(xy)} = 1 + FA_{(uv)}[\sigma\phi_{(xy)}\sin\chi_{(uv)} - i\sigma\phi_{(xy)}\cos\chi_{(uv)}] \quad (2.5)$$

and the intensity distribution in the image plane (that observed in the micrograph) is given by:

$$\begin{aligned} I_{(xy)} &= \Psi\Psi^{*}_{(xy)} \\ &= 1 + 2\sigma\phi_{(xy)} * FA_{(uv)}\sin\chi_{(uv)} \end{aligned} \quad (2.6)$$

where * indicates a convolution integral. This equation represents the intensity distribution in the image plane, within the limits of the weak phase approximation or in other words for a thin specimen. The term $\sin\chi_{(uv)}$, called the phase contrast transfer function, determines the transfer of object information to the image plane. For a perfect lens $\sin\chi_{(uv)} = 1$ and thus equation 2.6 reduces to:

$$I_{(xy)} = 1 + 2\sigma\phi_{(xy)} \quad (2.7)$$

and the object and the image are linearly related. Due to the defects present in magnetic lenses however, this is not experimentally possible. The main lens defects can be accounted for by the inclusion of an instrumental phase adjustment factor χ first derived by Scherzer (1949):

$$\chi = \frac{2\Pi}{\lambda}\left(\Delta f\frac{\alpha^2}{2} - C_s\frac{\alpha^4}{4}\right) \qquad (2.8)$$

where α is the scattering angle, C_s is the spherical aberration coefficient and Δf is the value of the lens defocus. The objective aperture subtends the maximum angle α of scattered electrons that can be used for image formation. If this aperture is decreased in size, then the effect of spherical aberration is also reduced but the information carrying part of the expression, that containing $\phi_{(xy)}$ is also diminished.

The final image contrast is therefore dependent on the oscillatory function $\sin\chi$ which has different values at different spatial frequencies, depending on the scattering angle for the particular frequency, the defocus value and the spherical aberration of the objective lens. $\sin\chi$ plotted against reciprocal periodicity [$1/d$ nm^{-1} ($= \lambda/\alpha$)] is shown in figure 2.2, assuming that the illumination is coherent over a range of defocus values. The diagram relates to a JEOL JEM 100C microscope operated at 100kV with a coefficient of spherical aberration, C_s of 0.67mm and a 50μm objective aperture.

When the microscope is in operation, it is desirable to select a defocus value with the maximum possible continuous range of spatial frequencies of the same contrast. This is known as the "optimum defocus" value or "Scherzer" focus Δf and is given by:

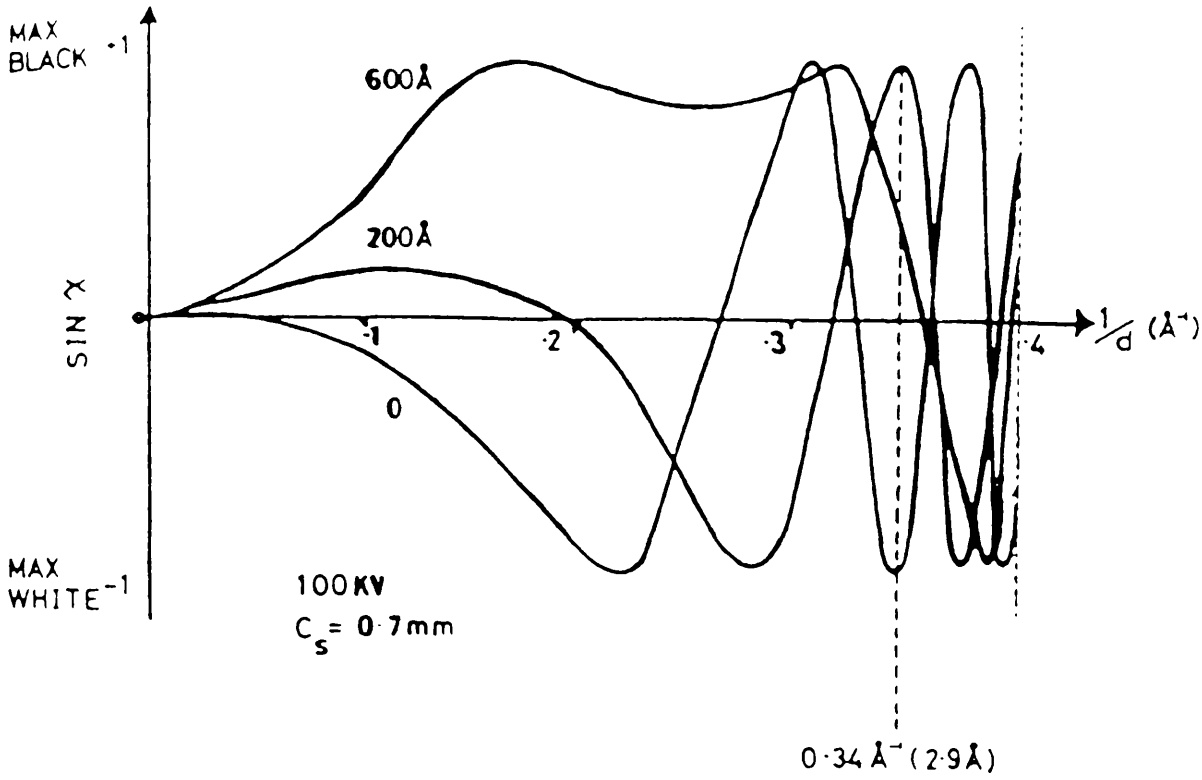

Figure 2.2

Phase contrast transfer functions for a range of defocus values, Δf = 0nm, 20nm and 60nm underfocus, with a 50μm objective aperture cut-off.

$$\Delta f = 1.2\sqrt{(C_s \lambda)} \qquad (2.9)$$

In the case of the JEOL 100C microscope, Δf is equal to 60nm and this is apparent when examining figure 2.2. The resolution loss that occurs as the value of C_s is increased for optimum defocus values is presented in figures 2.3(a),(b) and (c).

Eisenhandler and Siegel (1966) calculated the Scherzer cut-off d_{min} to be:

$$d_{min} = 0.65\ C_s^{0.25}\ \lambda^{0.75} \qquad (2.10)$$

The optimum defocus defines the limit of the most faithful reproduction over the maximum range of spatial frequencies. It is possible to resolve smaller structures however, if the correct defocus value is selected. An example of this can be seen in figure 2.2. At 20nm defocus a structural periodicity of 0.29nm ($3.4nm^{-1}$) would be imaged with high contrast whereas at zero defocus the same periodicity would have reversed contrast. Extreme caution must be exercised when interpreting such images however, as the absence of detail from other periodicities can lead to wrong assumptions being made as to a structure that is being observed.

The transfer functions described so far have assumed an electron source of perfect temporal and spatial coherence. In reality however, the electron microscope has a finite source size and a gaussian distribution of incident

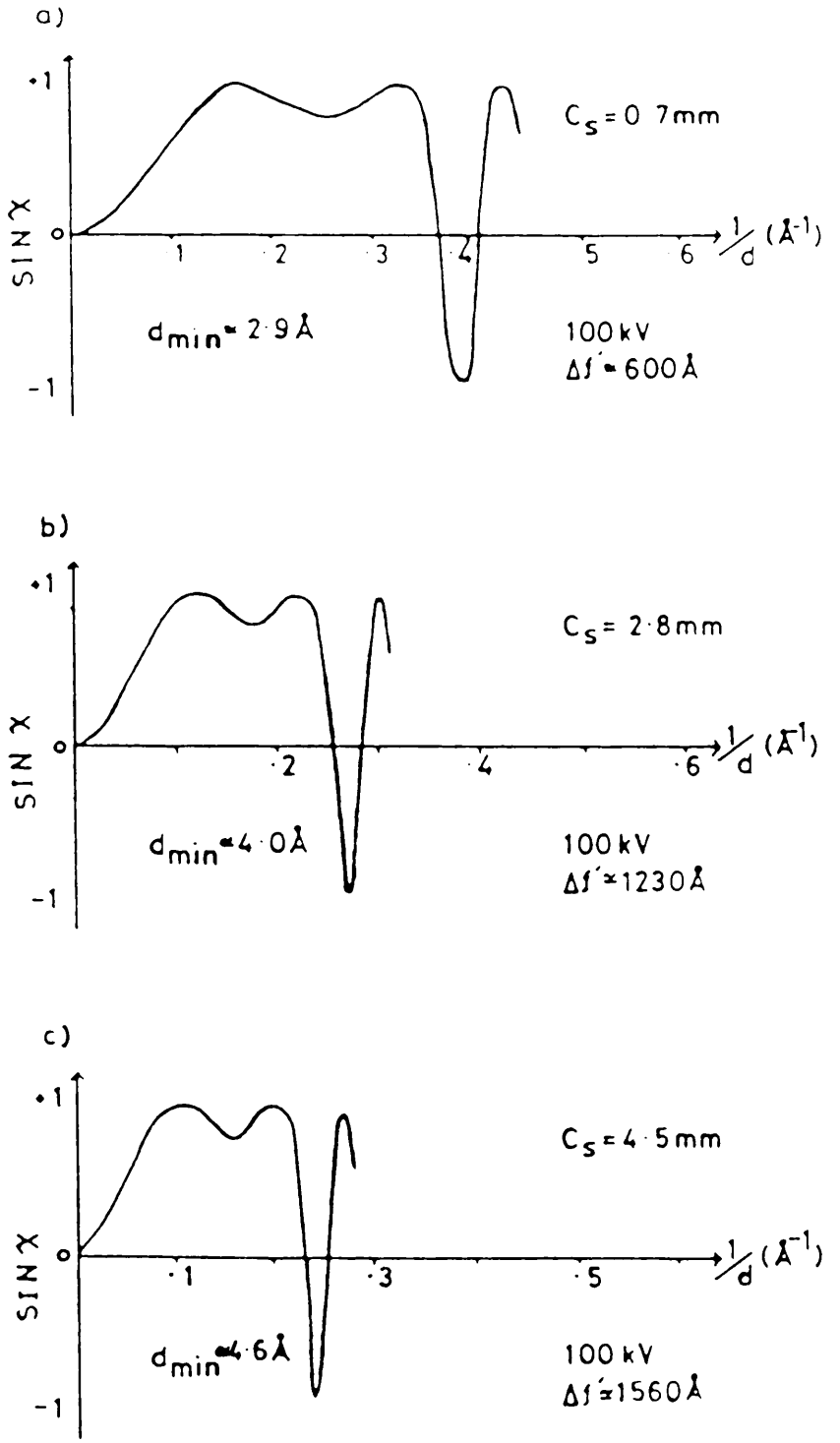

Figure 2.3

Optimum defocus phase contrast transfer curves for increasing spherical aberation coefficient.

(a) C_s = 0.7mm (b) C_s = 2.8mm (c) C_s = 4.5mm

electron energies. In order to account for these factors, envelope functions must be included in the expressions for the transfer functions (Hanzen, 1971; Hanzen and Trepte, 1971; Missel, 1973; Frank, 1973; Boerchia and Bonhomme, 1974).

The electron source can be approximated to a small disc shape defined by the final condenser lens aperture and chromatic aberration assumed to arise from sinusoidal modulations of the high voltage system and the objective lens current. The phase contrast transfer function can then be modified to account for these factors resulting in:

$$\sin\chi(s)_{\alpha,\epsilon} = \sin\chi(s).E_{\alpha}(s).E_{\epsilon}(s) \qquad (2.11)$$

where $E_{\alpha}(s)$ is the damping envelope function representing limited coherence width and $E_{\epsilon}(s)$ represents the modification due to chromatic fluctuations. However, as the partial coherence function is defocus dependent, this equation is only an approximation. The coherence and chromatic envelopes were shown by Frank (1973) to take the form:

$$E_{\alpha}(s) = \frac{2J_1[(2\Pi/\lambda)\alpha(C_S\alpha^3-\Delta f\alpha)]}{(2\Pi/\lambda)\alpha(C_S\alpha^3-\Delta f\alpha)} \qquad (2.12)$$

and

$$E_{\epsilon}(s) = J_o[(\Pi\lambda/d^2)\epsilon] \qquad (2.13)$$

where J_o and J_1 are the zero order and first order Bessel

functions respectively, α is the specimen illumination angle and ϵ is the focal variation due to high voltage (V) and lens current (I) fluctuations given by:

$$\epsilon = [(\Delta V/V) + (2\Delta I/I)]C_c \qquad (2.14)$$

where C_c is the chromatic aberration coefficient.

The coherence is also dependent on the illumination angle α. Figure 2.4(a) shows the effect on the potential coherence envelope functions of varying this angle and in figure 2.4(b) the optimum defocus phase contrast transfer function modified for a specimen illumination angle α of one milli-radian can be found. The effect of the coherence envelopes is shown in figure 2.5(a) for several focal variations (ϵ) and the optimum defocus contrast transfer function modified for chromatic focal variation ϵ equal to 5nm is shown in figure 2.5(b).

Within the limits of the stated approximations the above theory provides good evidence of the resolution that may be obtained. However, in reality some of these approximations do not always hold and in such cases a more rigorous dynamical treatment must be applied. No detail will be given here to such a theory but mathematical treatments have been outlined by various authors (Cowley and Moodie, 1957; Lynch and O'Keefe, 1972; Allpress et al., 1972; Goobman and Moodie, 1974; Cowley, 1975).

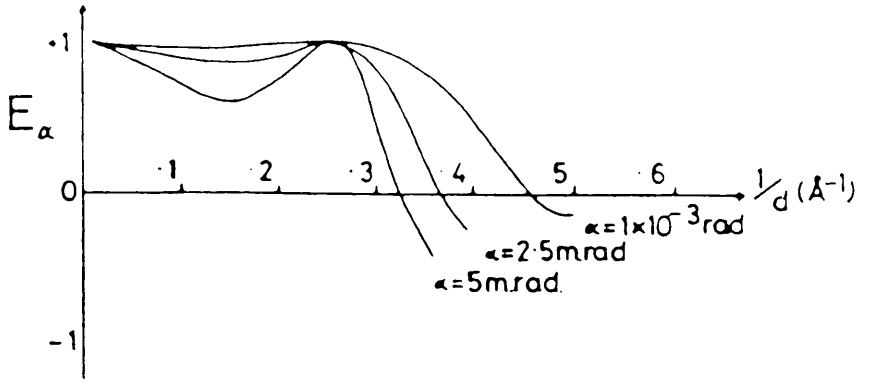

Figure 2.4(a)

Partial coherence envelope functions for various specimen illumination angles (α).

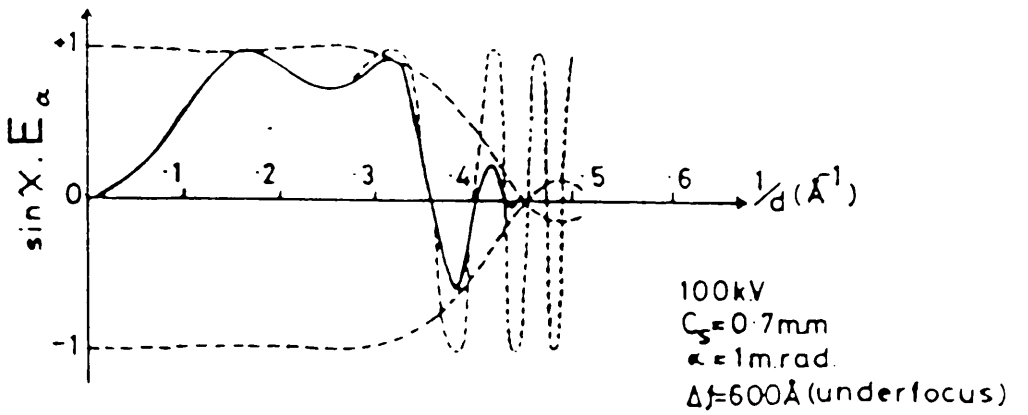

Figure 2.4(b)

Optimum defocus phase contrast transfer function, modified for specimen illumination angle α = 1 m.rad.

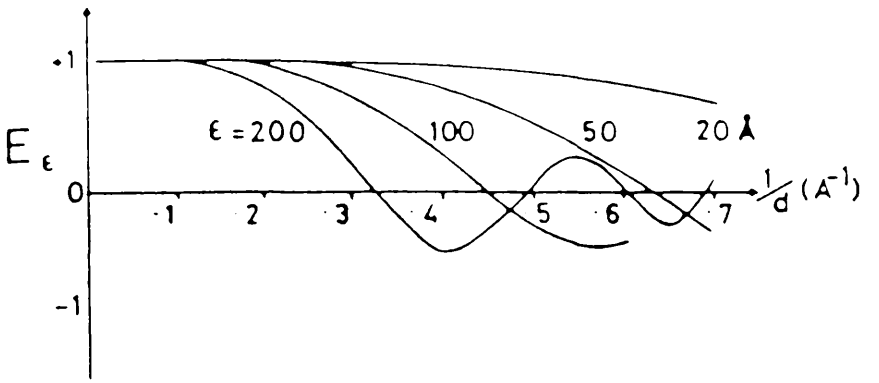

Figure 2.5(a)

Chromatic aberration envelope functions for several focal variations (ϵ).

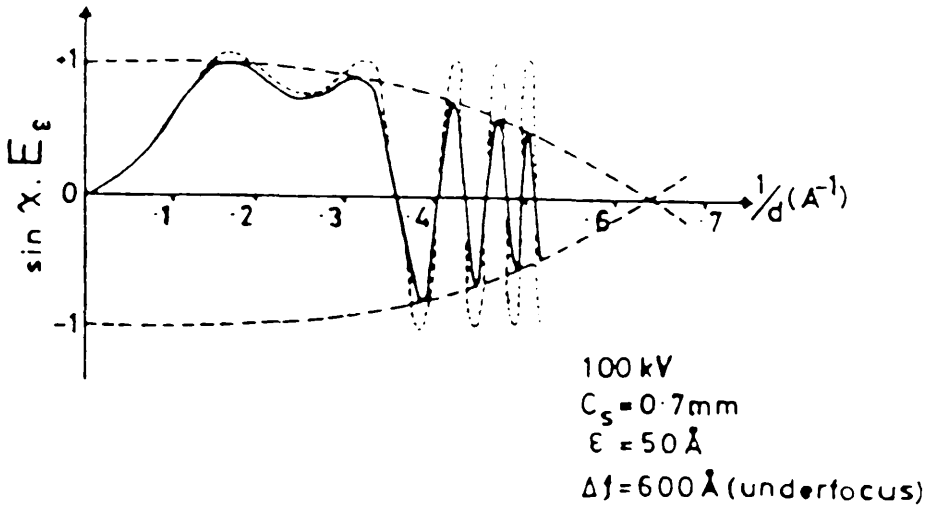

Figure 2.5(b)

Optimum defocus phase contrast transfer function, modified for focal variation ϵ = 50.

2.5 Factors Affecting the Retrieval of High Resolution Information

In addition to those factors discussed in the previous section, other factors exist which limit the retrieval of high resolution information, these are the following.

2.5.1 Astigmatism

Astigmatism arises from rotational variations in the focal length of the lens due to an asymmetric magnetic field. It may be caused by a number of factors such as the lens not being perfectly machined, the soft iron pole piece not being homogeneous or by the charging of contamination within the microscope leading to distortion fields. If extreme cleanliness of all surfaces exposed to the electron beam is ensured then the latter of these effects may be kept to a minimum. The effect of astigmatism is most critical in the objective lens. This lens also contains a system of stigmator lenses which may be used to apply a compensating field and thus correct the effects of astigmatism. This process of correction is undertaken by the operator who manipulates the stigmator lenses until the grains of the carbon support film appear symmetrical or else until a symmetrical fresnel fringe can be obtained around a hole in a "holey" carbon film.

2.5.2 Specimen Contamination

The build up of amorphous, usually carbonaceous, material on the specimen can give rise to charging effects which obscure the detail of the specimen. The residual atmosphere within the microscope column contains, in addition to normal atmospheric gases, some quantity of hydrocarbons which may have arisen from sources such as vacuum pumping fluids, gaskets, photographic plates or any parts which have been directly handled by the operator. These hydrocarbons will adsorb on all internal surfaces of the microscope including the specimen. The surface film is polymerised by electron bombardment and fixed in place. This process is constantly occurring as the specimen is viewed because the hydrocarbon layer is replenished by condensing vapour and by diffusion of already condensed material. This permanent deposit which builds up on a sample during examination is referred to as "contamination".

Modern electron microscopes reduce this problem by the incorporation of an anti-contamination device - generally a nitrogen cooled jacket surrounding the sample which removes the contaminants by preferential condensation. Another method employed in some microscopes is the production of an extremely high and clean vacuum by means of pumps of the sputter ion or turbomolecular types.

2.5.3 Mechanical Stability

Drifting of the specimen stage as well as thermal or mechanical vibrations can cause a reduction in image quality, especially during high resolution imaging. Modern microscopes generally employ secure mounts, with a hydraulic damping system supporting the column which minimises the effects of mechanical vibrations. When a new area of specimen is to be observed, time must be allowed for re-equilibration. If mechanical stability remains a problem then another measure which may be undertaken is the use of X-ray film since with the reduced exposure time necessary with such film the instability presents less of a problem.

2.6 Electron Diffraction

Another mode in which an electron microscope may be operated is that of electron diffraction. This technique was not greatly employed in the course of the present work so a very detailed description of it will not be given. Electron diffraction provides a very rapid visual assessment of the degree of structural ordering within a specimen. It can also be used to determine the nature of substances present within the sample by comparison with tabulated X-ray data in the A.S.T.M. index (1965). As mentioned earlier, a diffraction pattern is formed in the back focal plane of the objective lens. To operate an electron microscope in the electron diffraction mode the intermediate lens, instead of being focussed on the

intermediate image as is the case in the transmission mode, is focussed on the diffraction pattern and thus this pattern is magnified to the final image screen.

In the diffraction mode the electron microscope may be considered as a simple electron diffraction camera. Figure 2.6 shows diffraction from a set of lattice planes of spacing (d), lying at an angle θ to the incident beam. From the diagram:

$$\tan 2\theta = D/2L \qquad (2.15)$$

and using the Bragg law for first order diffraction (n=1):

$$\lambda = 2d\sin\theta \qquad (2.16)$$

Theta is exaggerated in this diagram and normally is less than 3°. Thus the approximation:

$$\tan 2\theta = 2\sin\theta = 2\theta \qquad (2.17)$$

can be invoked and combining with 2.12 and 2.13 leads to:

$$Dd = 2\lambda L \quad \text{or} \quad Dd = K \qquad (2.18)$$

where $2\lambda L$ (or K) is known as the camera constant, where λ is the electron wavelength and L is the camera length given by:

$$L = f_o M_1 M_2 M_3 \qquad (2.19)$$

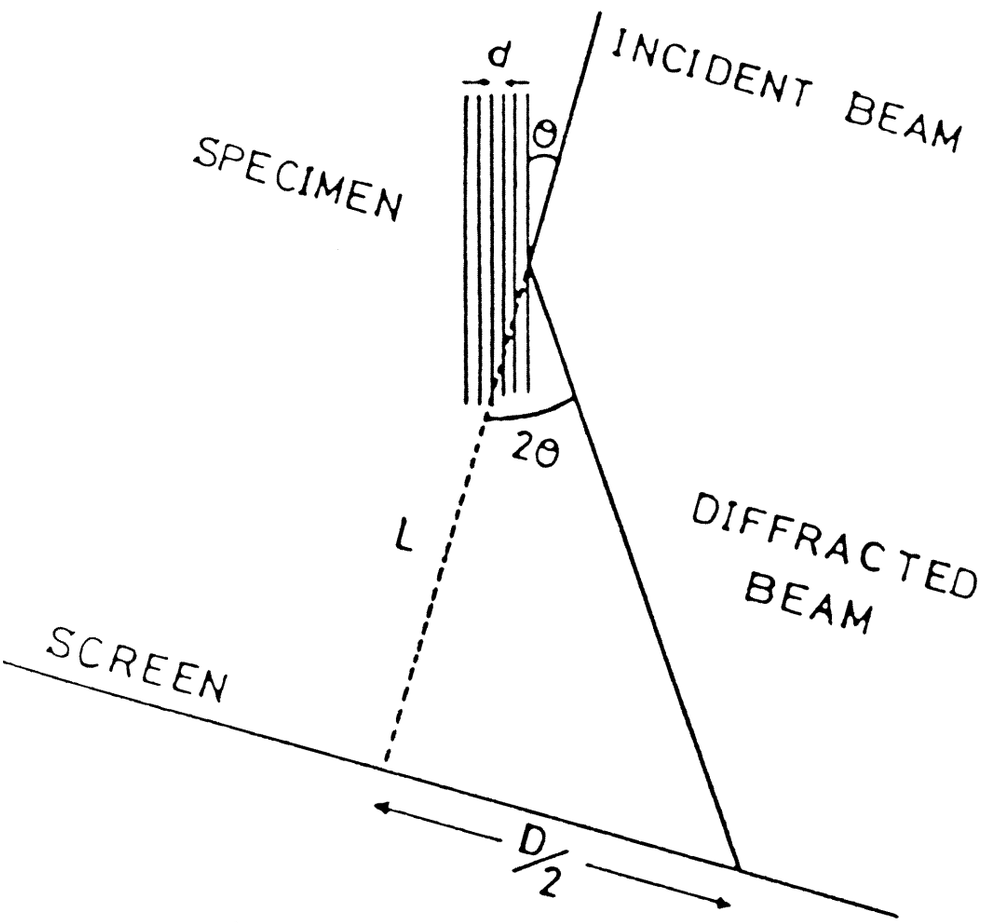

Figure 2.6

The electron microscope as a simple diffraction camera.

where f_o is the focal length of the objective lens and M_1, M_2 and M_3 are the magnification factors of the intermediate and projector lenses.

In practice the camera constant is determined from the diffraction pattern of a standard. Once this value has been established, lattice spacings may then be determined from measuring the spacings of the rings or spots on the diffraction pattern and then employing equation 2.15.

ADSORPTION

3.1 The Gas-Solid Interaction

3.1.1 Introduction

The study of the adsorption of a gas by a solid is, in general, intended to furnish information on the specific surface area of the solid and on its porous structure. The quantity of gas Na retained by a given sample depends on the mass m of the adsorbent, the temperature T, the pressure p of the vapour and the nature of the gas and solid.

$$Na = f(p, T, gas, solid) \qquad (3.1)$$

For a particular system at a particular temperature, the adsorption isotherm is an expression of the quantity of vapour adsorbed as a function of pressure.

$$Na = f(p)_{T,\ gas,\ solid} \qquad (3.2)$$

The majority of isotherms resulting from physical adsorption can be grouped into five classes, proposed initially by Brunauer, Deming, Deming and Teller (1940) and generally known as the Brunauer classification. The different curves that may be obtained are represented in figure 3.1.

The isotherms of type IV and V possess hysteresis loops,

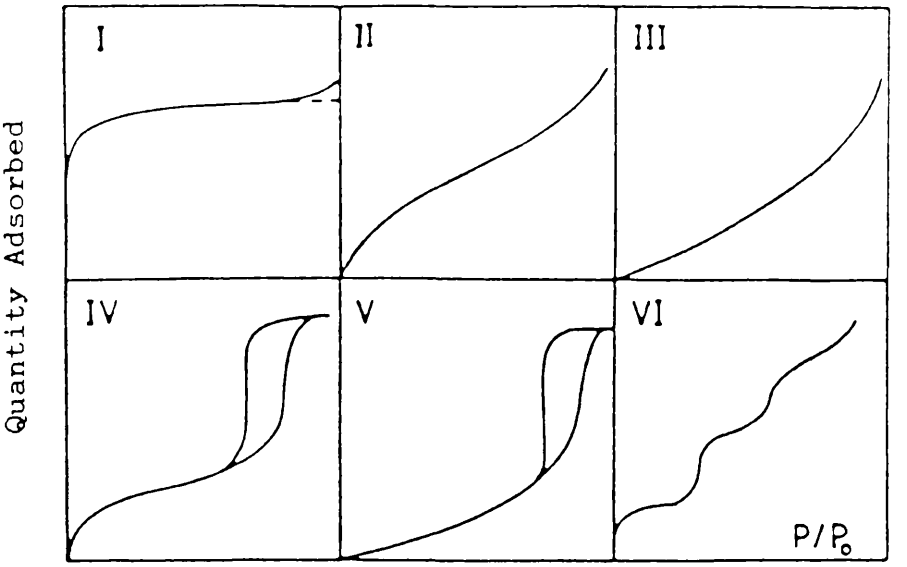

Figure 3.1

Different types of isotherms generally encountered.

the lower branch corresponding to adsorption and the upper branch to desorption of the gas from the surface of the solid. The step-wise isotherm, designated as type VI is relatively rare.

The type I isotherm is characteristic of a microporous adsorbent or of chemical adsorption. From it, a very good estimation of the micropore volume can be obtained. An isotherm of type II indicates that the solid is non-porous, however one of type IV is characteristic of a mesoporous solid. From these two types it is generally possibly to calculate the specific surface area of the solid. The type III and V isotherms indicate a system in which the interactions between the adsorbent and the adsorbate are weaker than the adsorbate-adsorbate interactions.

3.1.2 Intermolecular Forces

Adsorption occurs due to the forces between the gas molecules and the atoms or ions composing the solid. These include dispersion forces which are attractive and repulsive forces at short distances. Electrostatic forces must also be included if the solid or the gas are of a polar nature.

Dispersion forces, characterised originally by London (1930(a) and (b)), result from the rapid fluctuation of electron density in each atom, which induces an electric moment in a near neighbour and causes attraction between

the two atoms. Using the quantum mechanical theory of perturbations and neglecting dipole-quadropole and quadropole-quadropole interactions the following equation can be obtained (Honig, 1954; Young and Crowell, 1962):

$$U_d(r) = -Cr^{-6} \qquad (3.3)$$

where r is the interatomic distance and C is a constant associated with the dipole-dipole interaction. An expression for the repulsive forces can equally be derived from quantum mechanical considerations (Young and Crowell, 1962):

$$U_R(r) = Br^{-m} \qquad (3.4)$$

where B is an empirical constant and m is generally equal to 12. The total potential energy between the two atoms is therefore:

$$U(r) = -Cr^{-6} + Br^{-12} \qquad (3.5)$$

This relationship is generally known as the Lennard-Jones potential (Lennard-Jones, 1937) or "6-12" potential. Figure 3.2 shows the kind of representation produced when U(r) is plotted as a function of r.

The relation can equally be written in the form:

$$U(r) = \epsilon[(r_o/r)^{12} - 2(r_o/r)^6] \qquad (3.6)$$

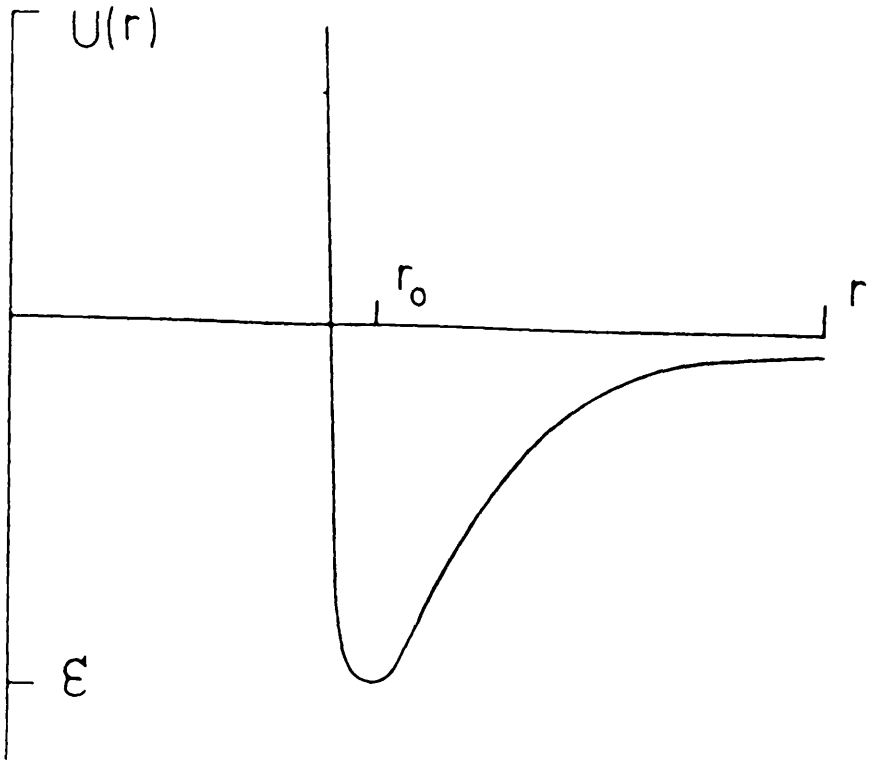

Figure 3.2

Representation of U(r) as a function of r.

where r_o is the separation for which dU/dr is zero and ϵ is the value of U when the separation is r_o.

A number of relations have been formulated in order to calculate parameter C from molecular properties of the atoms present. Notably, the relations derived by Kirkwood (1932) and Muller (1936), London (1930(a)) and Slater and Kirkwood (1931). All of these authors make use of the polarizability of the atoms. The other terms involved depend on the author, with such properties as diamagnetic susceptibilities, characteristic frequencies from the optical dispersion curves and the number of electrons participating in the interaction being utilised.

In order to obtain the adsorption potential Φ, the repulsion and dispersion energies being additive, the total energy for a large number of molecules can be expressed as the sum of the interactions of pairs, for all the distances r_i. For such a summation over a planar solid, it is possible to replace the sum by an integral (Honig, 1954) and assume a uniform density of ρ atoms per unit volume. In the case of the "6-12" potential, the following relationship is obtained (Young and Crowell, 1962):

$$\Phi(Z) = -(\rho\pi/3)(C/2Z^3-B/15Z^9) \qquad (3.7)$$

where the minimum is:

$$\Phi_o = \Phi(Z_o) = -(\rho\pi C/9Z_o^3) \qquad (3.8)$$

For a continuous solid Z_o is related to r_o by

$$Z_o = 0.765 r_o \qquad (3.9)$$

3.1.3 The Isosteric Heat of Adsorption

When the adsorbed phase is in equilibrium with the gaseous phase, it can be written:

$$\mu_a = \mu_g \qquad (3.10)$$

or

$$d\mu_a = d\mu_g \qquad (3.11)$$

where μ is the chemical potential of the gas. From purely thermodynamic considerations, the following relation, similar to that of Clausius-Clapeyron, can be obtained (Gregg and Sing, 1982):

$$\left(\frac{\delta \ln p}{\delta T} \right)_{Na} = \frac{q^{st}}{RT^2} \qquad (3.12)$$

The isosteric heat of adsorption q^{st} has a positive value. By integrating this equation, it is possible to calculate q^{st} with the aid of adsorption isotherms carried out at two or more temperatures. If only two temperatures are used, the value of q^{st} is given by:

$$qst = \frac{RT_1T_2(\ln p_2 - \ln p_1)_{Na}}{T_2 - T_1} \qquad (3.13)$$

where p_1 and p_2 are the equilibrium pressures at

temperatures T_1 and T_2 for a fixed quantity of adsorbed material Na (isostere).

If the isotherm has been measured at several temperatures, then:

$$(\ln p)_{Na} = - \frac{q^{st}}{RT} + \text{constant} \qquad (3.14)$$

which represents an adsorption isostere i.e. the relationship between p and T for a given adsorbed quantity Na. A representation of ln(p) as a function of 1/T immediately furnishes the value of q^{st}. It should also be noted that replacing p by p/p_o in the above two relations leads to the net heat of adsorption, $q^{st}-q^{L}$, where q^{L} is the molar heat of condensation.

It is clear that the value of q^{st} varies with the amount of vapour adsorbed due to the combined effects of the energetic heterogeneity of the adsobent surface and the interaction of the adsorbate molecules with the adsorbed phase film. The shape of the curve $q^{st}(Na)$ gives important information on the energetic state of the surface.

3.1.4 BET Equation

Physical adsorption on a non-porous solid leads, in the majority of cases, to an isotherm of type II. The adsorption begins with the creation of a statistical monolayer at the surface of the solid. The specific

surface S_m is related to the quantity adsorbed in the monolayer Na_m by the simple relation:

$$S_m = A_m N_{AV} Na_m \qquad (3.15)$$

where A_m is the specific surface of the adsorbed molecule and N_{AV} is Avogadro's number.

The theoretical model which best describes type II isotherms is that of Brunauer, Emmett and Teller (1938) based on a kinetic model of the adsorption processes.

$$\frac{p}{Na(p_o-p)} = \frac{1}{Na_m c} + \frac{c-1}{Na_m c}\frac{p}{p_o} \qquad (3.16)$$

in which the parameter c is given by:

$$c = \exp[(q_1-q_L)/RT] \qquad (3.17)$$

where q_1-q_L is the net heat of adsorption.

The BET equation can be linearised by representing $p/[Na(p_o-p)]$ as a function of p/p_o, which permits the quantity adsorbed in the statistical monolayer to be calculated and therefore the specific surface area of the solid.

One inconvenience of this model is the hypothesis that the adsorption sites of the surface are energetically identical. This is the reason why the equation is not

linearisable at low pressure. Another disadvantage is that the model is restrained to forces between the adsorbent and adsorbate and it neglects the lateral interactions between neighbouring molecules. This becomes more important once the monolayer is completed and explains the non-linearity of the expression at relative pressures superior to 0.5.

3.2 Adsorption by Microporous Solids

3.2.1 Polanyi Potential Theory

The basis of the theory of gas and vapour adsorption by microporous solids are the Polanyi adsorption potential theories (Goldman and Polanyi, 1928; and Polanyi and Kwelke, 1928). These define a thermodynamic adsorption potential ϵ as being the work necessary to make a molecule pass from the gas phase to a point considered to be at the surface, that is, the differential molar work of adsorption. For a flat and homogeneous surface, all the points of equal potential are found at the same distance from it, forming an equipotential plane. The potential diminishes with distance and finally becomes zero. The volume W contained between an equipotential plane and the surface corresponds to the volume in which adsorption can take place, the limiting volume of adsorption W_o corresponding to an equipotential plane of zero. Each equipotential plane is characterised by a value of ϵ. According to Polanyi (Goldman and Polanyi, 1928):

$$\epsilon = RT\ln(p_2/p_1) \qquad (3.18)$$

which is in fact, the free energy $-\Delta G$. Considering the adsorbed phase to be in the liquid state and there to be an equilibrium between the liquid and its saturated vapour, then:

$$A = RT\ln(p_o/p) = -\Delta G \qquad (3.19)$$

The calculation of W now reduces to:

$$W = Na\ M.Wt/\rho = Na\ V_m \qquad (3.20)$$

where M.Wt is the molecular weight of the adsorbate and ρ and V_m its density and molar volume in the liquid state at temperature T respectively.

The principal proposition of the Polanyi theory resides in the invarience of ϵ with T for a fixed W:

$$\left(\frac{\delta\epsilon}{\delta T}\right)_W = \left(\frac{\delta\Delta G}{\delta T}\right)_W = \left(\frac{\delta A}{\delta T}\right)_W = 0 \qquad (3.21)$$

and its validity has been largely confirmed, notably by Dubinin and his collaborators (Zaverina and Dubinin, 1939; Dubinin and Timofeev, 1946 and 1948; Dubinin, 1955). They have added, on the basis of a great number of experiments, a second complementary postulate to that of Polanyi: for two different adsorbates, the ratio of the values of ϵ is constant for identical adsorbed volumes.

$$(\epsilon_A/\epsilon_B)_W = \beta \qquad (3.22)$$

This ratio called the affinity coefficient, does not depend on the adsorbate and is independent of temperature. Benzene has been arbitrarily chosen as the reference substance and its affinity coefficient is taken to be equal to one.

3.2.2 Dubinin-Astakhov Equation

As has been already shown, the theory of volume filling of micropores (TVFM) contains the notion of the adsorption limit a_s, corresponding to the filling of all the adsorption space W_o by the adsorbate molecules. The dependence of a_s with temperature is, over a large temperature interval:

$$\alpha = -\frac{1}{a_s}\frac{da_s}{dT} \qquad (3.23)$$

where α is the thermal coefficient of limiting adsorption. It can in general be assimilated with the coefficient of thermal expansion of the liquid as indicated by Bering, Dubinin and Serpinsky (1966).

The value of a_s can be calculated in a very precise manner, so it is possible to replace the quantity adsorbed (a), by a parameter θ with dimensions which express the degree of filling of the micropores. By definition:

$$\theta = a/a_s \qquad (3.24)$$

The degree of micropore filling θ as a function of the thermodynamic value A described earlier, becomes (Dubinin, 1972 and 1975):

$$\theta = f(A/E,n) \qquad (3.25)$$

where E is the characteristic free energy of adsorption. The second parameter n is a constant for a particular system. The characteristic curve defined as the variation in A with the degree of filling, takes the form:

$$A = E\phi(\theta,n) \qquad (3.26)$$

If the function ϕ and the constant n remain identical for different vapours, then:

$$(A/A_o)_\theta = (E/E_o)_\theta = \beta \qquad (3.27)$$

The consequence of (3.22) and (3.27) is therefore the invariance of the characteristic curve with temperature. This has been verified by adsorption of benzene on an active carbon by Dubinin and Polstyanov (1966). Dubinin and Astakhov (1971(a),(b) and (c)) utilised the Weibull distribution function (Weibull, 1951) to give:

$$\theta = \exp[-(A/E)^n] \qquad (3.28)$$

or alternatively,

$$A = E[\ln(1/\theta)]^{\frac{1}{n}} \qquad (3.29)$$

Introducing in equation (3.28), equations (3.24) and (3.27), it becomes:

$$a = a_o \exp[-(A/E)^n] \qquad (3.30)$$

or in terms of volume:

$$W = W_o \exp[-(A/E)^n] \qquad (3.31)$$

This final form is known as the Dubinin-Astakhov equation. It can be linearised to the form:

$$\ln W = \ln W_o - (A/E)^n \qquad (3.32)$$

These relationships are used principally for the study of adsorption on microporous solids for which n is not equal to two.

3.2.3 Dubinin-Radushkevich Equation

An analysis of numerous adsorption experiments by diverse vapours on active carbons of different structures has shown that for the most part n is equal to two (Dubinin and Zaverina, 1949; Radushkevich, 1949). Dubinin and Radushkevich have proposed a relation describing

adsorption of vapours on these active carbons.

$$W = W_o \exp[-B(T/\beta)^2 \log^2(p_o/p)] \qquad (3.33)$$

This equation is related directly to that of Dubinin-Astakhov by:

$$E_o = 0.01915/B^{1/2} = 2.303X10^3 R/B^{1/2} \qquad (3.34)$$

The parameters B and E_o are related to an average dimension of the micropores. When concerned with the reference vapour (benzene) the characteristic energy is called E_o but for all other vapours it is defined as:

$$E = E_o\beta \qquad (3.35)$$

i.e. β is equal, by convention, to one for benzene. The value of the affinity coefficient (sometimes called the similarity coefficient) β can be calculated empirically using the molecular properties and physical constants of the adsorbate. The relationships most widely used are the ratio of the molar volumes (Dubinin and Timofeev, 1947):

$$\beta = V_m/V_m(C_6H_6) \qquad (3.36)$$

and the ratio of the parachores (Dubinin and Zaverina, 1950):

$$\beta = P/P(C_6H_6) \text{ where } P = M.Wt\ \gamma^{1/4}/\rho \qquad (3.37)$$

3.2.4 Determination of the Value of n

The parameter n of the Dubinin-Astakhov equation in fact describes the energetic heterogeneity of the adsorbent surface (Rand, 1976), and its value increases as the sample becomes more homogeneous. For most systems encountered the value of n is known and therefore does not have to be determined but in some cases it is unknown and must be found.

In principal, for an isotherm of type I, it is relatively easy to make an approximate determination of W_o without using the Dubinin-Radushkevich representation. This is carried out by multiplying the limiting quantity adsorbed by the molar volume of the liquid.

$$W_o = Na_o V_m \qquad (3.38)$$

The precision obtained with this procedure is sufficient for a good determination of n. A simple mathematical transformation of (3.31) leads to:

$$\ln\ln(W_o/W) = n\ln(A) - n\ln(E) \qquad (3.39)$$

Representing $\ln\ln(W_o/W)$ as a function of $\ln(A)$ permits the calculation of n.

3.2.5 Physical Significance of B

Dubinin and Zaverina (1949) reported that the structural constant B of the Dubinin-Radushkevich equation increased with the degree of activation of a given material. Two equations have been proposed for the existence of a relation between B and the average dimension of the micropores by Stoeckli (1974) and Dubinin (1979) independently at first and then in collaboration (Dubinin and Stoeckli, 1980).

A graphical representation of B as a function of $\overline{Rg}^2$, the mean square gyration radius of the micropores, obtained from small angle X-ray diffraction, suggested to Stoeckli the empirical relation:

$$\overline{Rg}^2 = (62.B.10^6)^{\frac{1}{2}} \qquad (3.40)$$

Dubinin however, showed that the product of Rg with the characteristic energy E_o is constant.

$$\overline{Rg}.E_o = (14.8\pm0.6)\text{nmkJ/mol} \qquad (3.41)$$

In fact these two approaches are equivalent, as E_o is proportional to B by the relation (3.34).

Dubinin and Stoeckli (1980) have proposed the following alternative empirical relation, valid for a certain number of active carbons.

$$x = k/E_o \text{ where k has units nmkJ/mol} \qquad (3.42)$$

x being a characteristic dimension of the micropores, that is the half-width of slit shaped pores. k(nmkJ/mol) is taken to be 12.5 when E_o is less than 22-23kJ/mol and to be 8.5 when E_o is greater than 23-24kJ/mol. The value x may also be used to calculate the geometric surface area (S_g) of an active carbon (Dubinin, 1980), where,

$$S_g\ (m^2/g) = 2W_o/L = W_o/x \qquad (3.43)$$

where L is the micropore width expressed in nm (L = 2x).

More recently, formula (3.42) has been amended by Kraehenbuehl (1984-86). Using results from a series of experiments on CEP carbons and on molecular sieves MSC-5 and MSC-7 the following formulae were obtained:

$$\bar{k} = 59.3 + 15.85L \qquad (3.44)$$

in terms of micropore width or alternatively in terms of the characteristic energy:

$$\bar{k} = 410 - 9.54E_o \qquad (3.45)$$

3.3 Immersion Calorimetry

3.3.1 Introduction

The amount of heat released, when a degassed powder is immersed into a liquid, is directly proportional to the surface area of the solid. The heat of immersion is a good method for rapidly determining the surface area of a solid, provided the amount of heat released per unit surface area of this solid is already known. The direct proportionality relating the surface area and enthalpy of immersion is applicable principally to solids that possess an open surface (e.g. graphite, graphitised carbon black). When concerned with active carbons, or more generally, microporous solids, more factors are involved in the release of heat, such as the structure and volume of the micropores or the possible presence of an external surface (meso- and macropores).

3.3.2 Immersion of Microporous Solids in Organic Liquids

It can be shown (Kraus, 1955; Chessick and Zettlemoyer, 1959; Zettlemoyer and Narayan, 1967; Clint, 1973) that for the case of microporous solids which do not possess an external surface area, the enthalpy of immersion ΔH_i is related to the isosteric heat of adsorption q^{st} by the expression:

$$-\Delta H_i(T) = \int_0^1 q^{st}(T;\theta)d\theta - \Delta H_{vap}(T) \qquad (3.46)$$

where θ is the degree of micropore filling W/W_o. The negative sign arises because by convention q^{st} is a positive quantity but the calorimetric value ΔH_i is negative.

It has been shown (Dubinin, 1975) that the net heat of adsorption q^{net}, defined by:

$$q^{net} = q^{st} - \Delta H_{vap} \tag{3.47}$$

can be obtained from the Dubinin-Astakhov or Dubinin-Radushkevich equations. For a general case where n is variable the Dubinin-Astakhov equation leads to:

$$q^{net} = E[(\ln a_o/a)^{1/n} + (\alpha T/n)(\ln a_o/a)^{(1/n)-1}] \tag{3.48}$$

where α is the coefficient of thermal expansion of the adsorbate. For the case of active carbons, with n = 2, the following expression is obtained using (3.24) and (3.35).

$$q^{net} = \beta E_o[(\ln 1/\theta)^{1/2} + (\alpha T/2)(\ln 1/\theta)^{-1/2}] \tag{3.49}$$

With (3.47), the relation (3.46) becomes:

$$-\Delta H_i = \int_0^1 q^{net} d\theta \tag{3.50}$$

Combining (3.47), (3.49) and (3.50) leads to:

$$-\Delta H_i = \beta E_o \int_0^1 [(\ln 1/\theta)^{1/2} + (\alpha T/2)(\ln 1/\theta)^{-1/2}] d\theta$$

$$= \beta E_o \int_0^1 (\ln 1/\theta)^{1/2} d\theta + (\alpha T \beta E_o/2) \int_0^1 (\ln 1/\theta)^{-1/2} d\theta \qquad (3.51)$$

The solution to this type of integral is the gamma function $\Gamma(x)$ (Gradshteyn and Rhyzik, 1980; Abramonitz and Stegun, 1965).

$$\int_0^1 (\ln\ 1/x)^p dx = \Gamma\ (p + 1) \qquad (3.52)$$

$$\Gamma\ (p + 1) = \begin{cases} \text{for } p = 3/2 : \Gamma\ (3/2) = \sqrt{\pi}/2 \\ \text{for } p = 1/2 : \Gamma\ (1/2) = \sqrt{\pi} \end{cases} \qquad (3.53)$$

The solution of (3.51) is as follows, depending on the chosen units of the enthalpy of immersion:

$$-\Delta H_i = E_o \beta \sqrt{\pi} (1 + \alpha T)/2 \qquad J/mol \qquad (3.54a)$$

$$-\Delta H_i = E_o \beta \sqrt{\pi} (1 + \alpha T)/2V_m \qquad J/cm^3 mi. \qquad (3.54b)$$

$$-\Delta H_i = E_o W_o \beta \sqrt{\pi} (1 + \alpha T)/2V_m \qquad J/g\ solid \qquad (3.54c)$$

3.4 Measurement of the External Surface of an Active Carbon

Very frequently there is an appreciable external surface area associated with microporous active carbons, in the form of mesopores, macropores and open surface. It is important to be aware of both types of surface that are present because the adsorption phenomena taking place on them are different, particularly from an energetic point of view.

The adsorption isotherm is subject to modifications due to the presence of an external surface as can be seen in figure 3.3. Isotherm 1. corresponds to adsorption on a microporous adsorbent. Isotherm 2. represents adsorption uniquely in the micropores and isotherm 3. shows the coverage of the external surface of the solid (i.e. the difference between the first two).

There are a number of methods to enable the calculation of the external surface area of a microporous carbon, such as the Gregg-Langford method (Gregg and Langford, 1969), t-curves (Schull, 1948; Lippens et al., 1964), α_s-curves (Sing, 1970) and the t/F method (Dubinin and Kadlec, 1975). However, it was the methods described in the following sections that were utilised in the present study. A comparison of the results that may be obtained by these different methods has been carried out by Kraehenbuehl (1983).

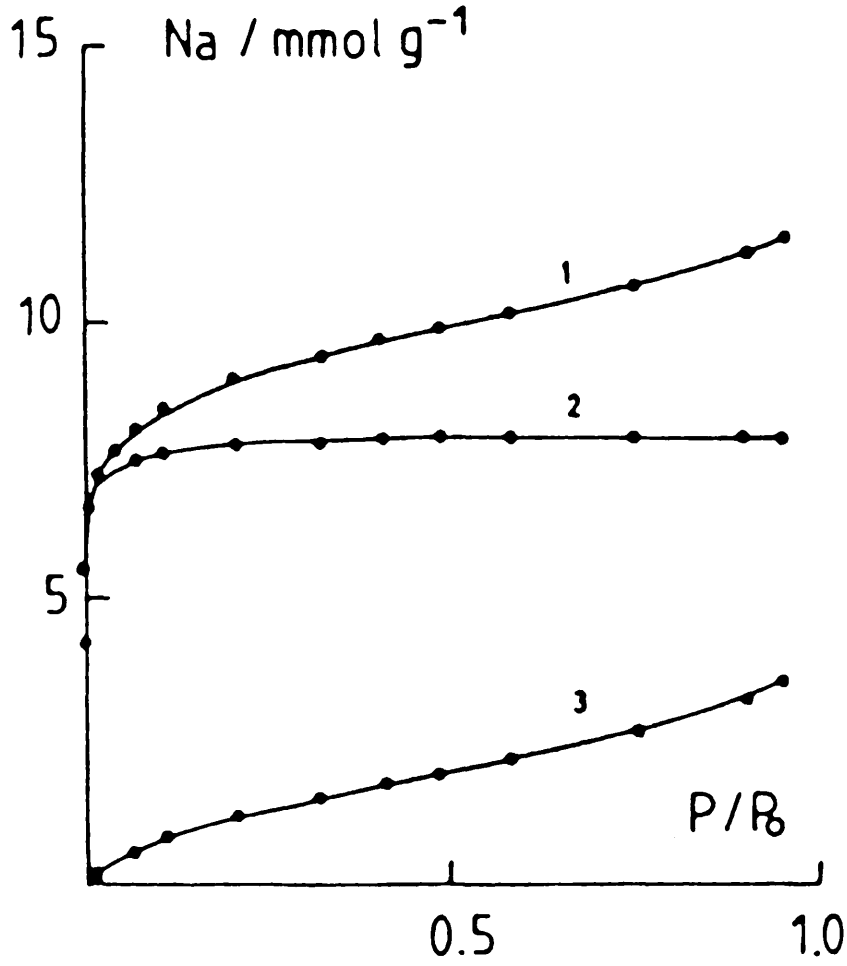

Figure 3.3

Adsorption isotherms of a microporous solid that contains an external surface area.

(1) Total isotherm. (2) Isotherm from adsorption in the micropores only. (3) Isotherm showing coverage of the external surface.

3.4.1 Decomposition of the Isotherm

In this method the experimental adsorption isotherm is decomposed into two distinct isotherms: the isotherm for the filling of the micropores and the isotherm for the coverage of the external surface. The micropore filling is described by the Dubinin-Radushkevich equation, which permits the values of the micropore volume W_o and the characteristic energy E_o to be obtained. Knowing these two values, the theoretical quantity adsorbed in the micropores for all relative pressures P/P_o can be calculated by the relation:

$$Na_{DR} = \frac{W_o}{V_m} \exp\left[-\left(\frac{RT\ln(p_o/p)}{\beta E_o} \right)^2 \right] \qquad (3.55)$$

where V_m is the molar volume of the liquid adsorbate. Each calculated quantity adsorbed is then subtracted from the corresponding total experimental quantity adsorbed. The result of this operation gives the quantity adsorbed on the external surface at the considered relative pressure (Ali and McEnaney, 1985).

$$Na_{ext} = Na_{exp} - Na_{DR} \qquad (3.56)$$

Applying the BET treatment to the couples (Na_{ext} ; p/p_o) gives the external surface area and the corresponding value of c. This method is applicable for relative pressures in the range 0.15 to 0.4 because outwith this domain deviations occur. For the low relative pressures,

the difference between Na_{exp} and Na_{DR} is very small, leading to elevated values of the relation $p/Na(p_o-p)$. For those relative pressures greater than 0.4 multilayers are formed and there is an increase in lateral interactions.

3.4.2 Decomposition of the Enthalpy of Immersion

The principle of this method is identical to that of the decomposition of the isotherm. In effect, the amount of heat released is the sum of the contributions from the micropore filling and the coverage of the external surface. It has been shown earlier that it is possible, knowing the physical properties of the microporous solid (W_o and E_o), to calculate the enthalpy of immersion of the micropores by the relation:

$$-\Delta H_{i\ mi}(J/g) = \frac{E_o W_o \beta \sqrt{\pi}}{2V_m}(1 + \alpha T) \qquad (3.54c)$$

If the experimental enthalpy is greater than the calculated one, this excess can have two origins:

(1) the presence of impurities in the solid which dissolve during immersion therefore liberating a certain quantity of energy.

(2) the presence of an external surface whose area is proportional to the amount of heat released.

The immersion enthalpies of external surfaces in a great number of liquids are well known making it possible to

calculate the area not contained in the micropores by subtracting the microporous contribution calculated by (3.54c) from the experimental enthalpy and dividing the result by the standard enthalpy (Jm^{-2} of open surface) (Stoeckli and Kraehenbuehl, 1984).

$$S_{ext}(m2/g) = \frac{\Delta H_{i\ exp}\ (J/g) - \Delta H_{i\ mi}\ (J/g)}{h_i\ (J/m2)} \qquad (3.57)$$

3.5 Distribution of the Mesoporosity

As was shown earlier, adsorption occurs in mesopores via capillary condensation and the pore radius can be calculated using the Kelvin equation (Gregg and Sing, 1982). For example, supposing the molar volume of the liquid to be independent of pressure (i.e. the liquid is incompressible), then for nitrogen at 77K the Kelvin equation can be used to calculate r_k in the domain of relative pressures superior to 0.4 in the form:

$$r_k = 4.14/\ln(p_o/p) \qquad (3.58)$$

where V = 34.68cm^3/mol, γ = 8.85 dyne/cm and ϕ = 0°. The effective radius of the pore may then be calculated via the simple relation (see figure 3.4):

$$r_p = r_k = t \qquad (3.59)$$

The desorption branch can be expressed in the form of a volume as a function of r_k. A decrease in relative

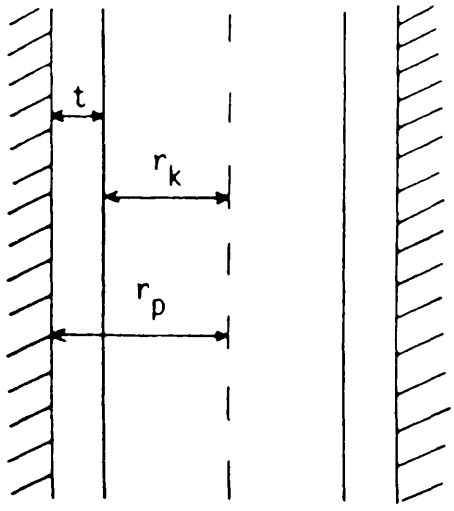

Figure 3.4

Cross-section of a pore, where t is the thickness of the adsorbed layer, r_k is the Kelvin radius and r_p is the effective radius of the pore.

pressure $\Delta(p/p_o)$ involves a decrease in the Kelvin radius Δr_k, the average Kelvin radius being $\overline{r_k}$. The change in volume ΔV_q associated with this decrease in radius is:

$$\Delta V_q(\overline{\overline{r_k}}) = \Delta V_k + \Delta V_t \qquad (3.60)$$

where ΔV_k and ΔV_t are respectively the volume desorbed from pores of internal radius $\overline{r_k}$ and the contribution to the desorption from the free surface. The real volume of the pores can be obtained by the relation:

$$\Delta V_p = \Delta V_k(\overline{\overline{r_p}}/\overline{\overline{r_k}})^2 \qquad (3.61)$$

for cylindrical pores and by the following relation for slit pores:

$$\Delta V_p = \Delta V_k(\overline{\overline{L_p}}/\overline{\overline{L_k}}) \qquad (3.62)$$

The porosity distribution curve is a representation of $\Delta V_p/\Delta r_p$ as a function of $\overline{r_p}$ (or alternatively for slit pores $\Delta V_p/\Delta L_p$ as a function of $\overline{L_p}$). The surface of the walls ΔS_p corresponding to the decrease in volume ΔV_p is directly proportional to $\Delta V_p/\overline{r_p}$, the proportionality factor being dependent on the choice of units (Gregg and Sing, 1982). The surface area of the mesopores is, by consequence, the sum of the increments ΔS_p of the desorption branch.

3.6 Distribution of the Microporosity

The micropore distribution may be obtained by using immersion calorimetry. The solid whose distribution is to be determined is immersed into several organic liquids of various molecular dimensions. Rearranging equation (3.54c) leads to (Kraehenbuehl et al., 1986):

$$W(L) = \Delta H_i/(\beta E_o(1 + \alpha T)\sqrt{\pi}/2V_m) \qquad (3.63)$$

assuming there to be no external surface area present. W(L) is the micropore volume seen by a liquid of molecular dimension L. In the above equation ΔH_i is measured by immersion calorimetry, E_o is calculated from the isotherm and the physical constants of the adsorbates are obtained from the literature.

When the values of W(L) have been calculated for a number of different liquids, a histogram of dW/dL as a function of L can be constructed showing the micropore size distribution.

EXPERIMENTAL

4.1 Static Adsorption

In the present work, adsorption of organic vapours was measured by the gravimetric method using apparatus of the McBain type (figure 4.1).

The sample was placed in a quartz cell, suspended from a thermostated quartz spring. It was then outgassed by means of a turbomolecular pump (Pfeifer TRH 110) connected in series with a rotary pump (Ewards EDM 2).

The pressure within the system was measured by two Barocel pressure sensors connected to a Datametrics 1173 electronic manometer and a Solartron 7045 digital voltmeter. A Servogor 210 chart recorder was used to ascertain when the pressure had attained equilibrium. The pressure sensors were fixed to a copper plate and both this and the quartz spring were thermostated at 37±0.05°C using a Julabo V12B thermostat.

The temperature stability of the sample was ensured by using a Lauda GP-D8/17 thermostat, circulating water (15-50°C, stability ±0.03°C) through a large Dewar flask placed around the sample. During the outgassing process this set-up was replaced by an electric oven heated to around 400°C.

The extension of the spring during the experiment was

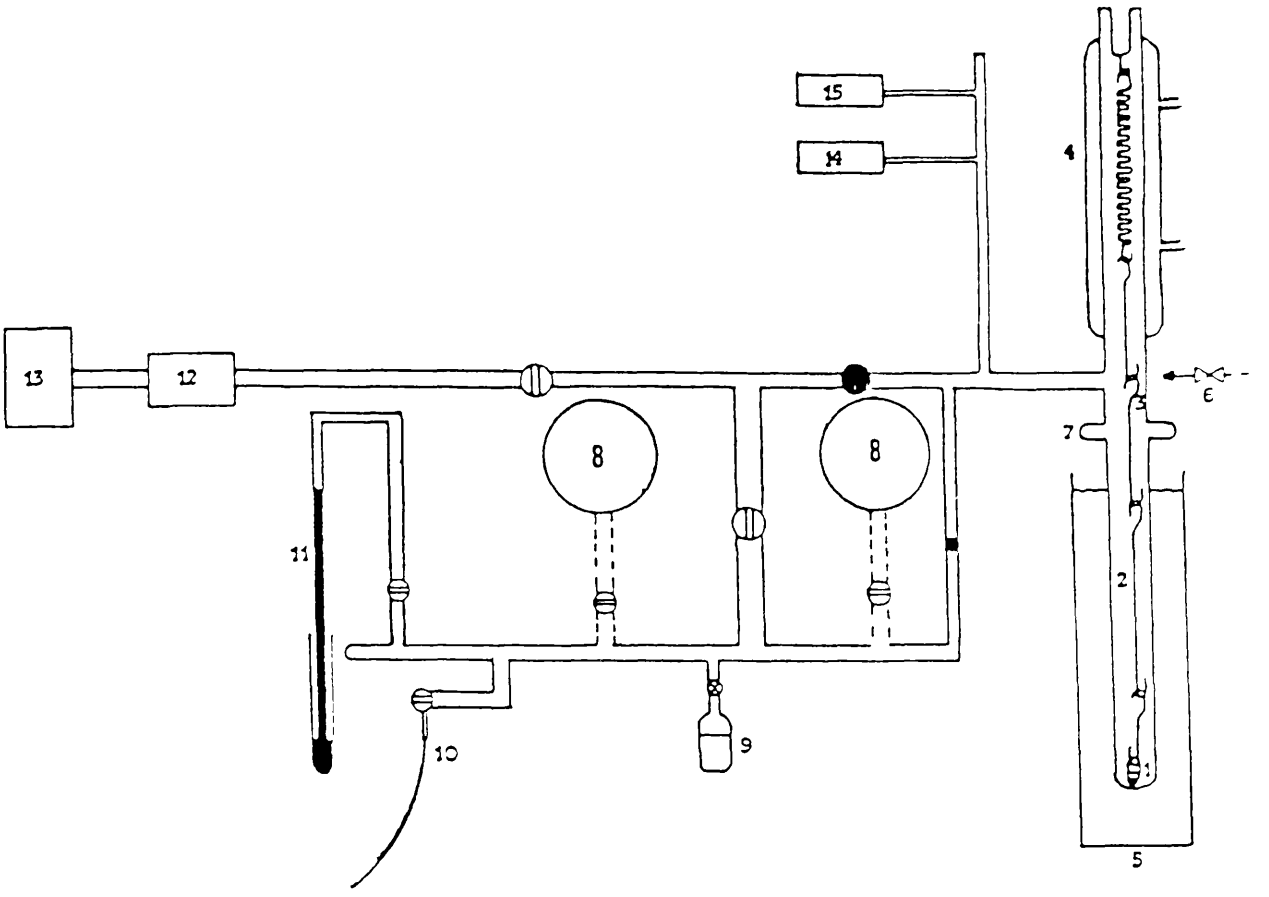

Figure 4.1

Gravimetric adsorption apparatus of the McBain type.

Key to figure 4.1

1. Quartz container which holds sample and a glass wool plug.
2. Quartz spring.
3. Marker on which micrometer is focussed.
4. Water jacket.
5. Water bath.
6. Micrometer.
7. Metal joint.
8. Gas reservoirs.
9. Liquid reservoirs.
10. Tap allowing introduction of air or gas.
11. Mercury manometer.
12. Turbo-molecular pump.
13. Rotary pump.
14. and 15. Pressure sensors.

measured by means of a Leitz micrometer.

All taps leading directly into the enclosure containing the quartz spring were constructed of metal (L'Air Liquid RXA-3 and X12) ensuring that no grease was required in this section and thus facilitating the production of high vacuum.

Before being placed within the system the sample was first placed within the pre-weighed quartz cell and weighed on a Mettler AE 166 balance. It was then suspended on the spring, the system was sealed and the pumping system operated. The material was outgassed at 400°C for approximately 20 hours, before being surrounded by a water bath stabilised at 20°C. The weight loss of the sample was then determined using the equation:

$$\text{Weight loss} = \frac{\Delta\text{div} + \text{Ar}}{\text{Cr}} \qquad (4.1)$$

where Δdiv is the difference in the micrometer readings before and after outgassing. Cr is the spring constant (e.g. 29200 divisions/g for one of the sets of apparatus used) and Ar is the Archimedes Force defined as:

$$\text{Ar} = \frac{\text{p V M.Wt. Cr}}{\text{R T}} \qquad (4.2)$$

where p is pressure, V is the volume of the sample, T is the temperature, R is the gas constant and M.Wt. is the

molecular weight of the gas present (assumed to be nitrogen for the outgassing process). With the weight loss of the sample now known it is a simple matter to calculate the actual weight of the outgassed sample.

The adsorption experiments were commenced by introducing a small quantity of the adsorptive vapour into the adsorption chamber. From the chart recorder it could be observed when equilibrium had been achieved and both the pressure and spring extension could then be measured. The quantity of vapour adsorbed (Na) was calculated using the following relationship:

$$Na\ (p,T)[mol\ g\text{-}1] = \frac{\Delta div + Ar\ (p/p_0)}{Cr\ M.Wt.\ Mc} \qquad (4.3)$$

where Δdiv is the extension of the spring measured in divisions, p is the equilibrium pressure, p_0 is the saturated vapour pressure of the adsorbate, Mc is the mass of the outgassed carbon and Ar, Cr and M.Wt. have the same meanings as above. The isotherm could then be constructed by plotting the quantity of gas adsorbed against the relative pressure. The construction of the isotherm and of the Dubinin-Radushkevich plots was carried out both manually and using a linear regression computer program to obtain the line of best fit.

4.2 Immersion Calorimetry

Enthalpies of immersion were measured using a calorimeter of the Calvet type, shown schematically in figure 4.2.

The thermal stability of the calorimeter was achieved by using a water jacket (1) surrounding an enclosure filled with copper powder (2). Within this assembly could be found 180 copper-constantan themocouples (3).

The solid to be examined (≈0.3g) was sealed under vacuum in a glass bulb (5) specially constructed to break easily within the calorimeter. This bulb, together with 5ml of the liquid into which immersion was to take place (6) were placed inside a brass cell of volume $8cm^3$ (7). The cell was then sealed by means of a stainless steel tube (8) terminating in a screw fitting. The plunger inside this tube (9) facilitated the breaking of the bulb. This section was isolated from the exterior by a Teflon plug (10). The thermal stability of the equipment was further aided by situating it in a water bath regulated to ±0.01K by a Lauda MS thermostat. The complete assembly was further isolated with a casing of polystyrene.

The calorimeter was calibrated using two means. Firstly, electrically using a 1000Ω resistance in place of a sample and secondly by immersing carbon UO-3 in benzene, an immersion for which the heat evolution had been previously tabulated.

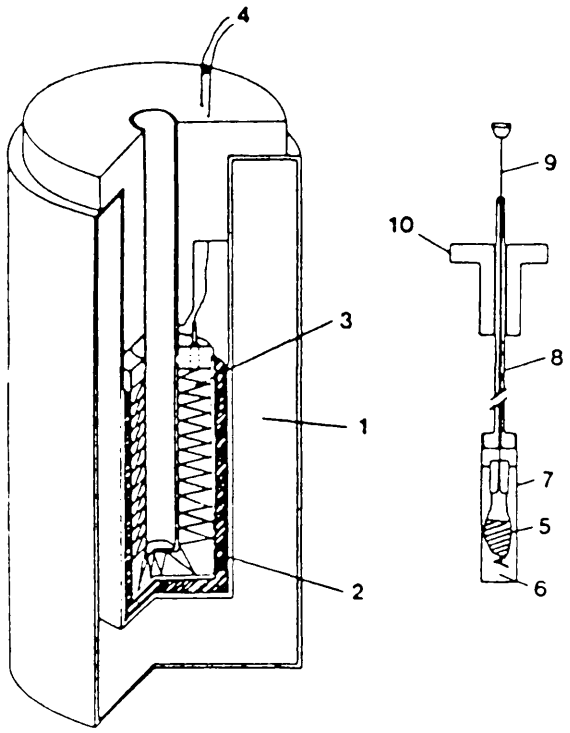

Figure 4.2

Calorimeter of the Calvet type used for measuring immersion enthalpies.

In order to carry out an enthalpy of immersion experiment, the cell was first left within the calorimeter for some time until the temperature had stabilsed. Next the bulb was broken and the value of the enthalpy was obtained by integrating the signal from the thermocouples with time by means of a Hewlett-Packard HP-85 computer.

4.3 Preparation of Holey Carbon Film

Holey carbon films were required because of the increased definition obtained when observing an area of sample protruding over a hole as compared with viewing an area situated on top of a region of carbon film. The following method was employed in their construction.

Sections of freshly cleaved mica were placed in the freezer compartment of a refrigerator. On removal from the freezer, the mica sections were coated with a 0.25% volume solution of Formvar (polyvinyl formal, molecular weight 24000-40000) in $CHCl_3$. The coating was carried out in a warm, humid environment in order to create small holes in the plastic film due to the condensation of water droplets.

The plastic films were subsequently floated off of the mica sections and were then picked up on copper electron microscope grids (400 mesh). They were then dried at around 30°C in a laboratory oven.

Once dry, the grids were placed in a coating unit (figure

4.3) which was evacuated to a pressure of around 10^{-4} Torr. An electric current (30 volts, 20 Amps) was passed through two carbon rods, evaporating the carbon which then coated the plastic film resulting in greater electron beam stability.

4.4 Sample Preparation For Electron Microscopy

All samples prepared for analysis by transmission electron microscopy were prepared in the following manner. The samples were first crushed using an agate mortar and pestle and then more finely ground between glass microscope slides. The samples were next dusted onto electron microscope grids which had been previously coated in holey carbon film.

4.5 High Resolution Electron Microscopy

In order to achieve meaningful results the electron microscope had to be carefully used and aligned. In the present work, samples were examined on a JEOL 1200EX microscope operated at an accelerating voltage of 120keV. Studies were carried out with both a standard tungsten hairpin filament and with a lanthanum hexaboride (LaB_6) filament for greater brightness and beam coherence. The instrument was fitted with an image intensifier system and frame storage facility to aid viewing. Final images were recorded on photographic plate film (Ilford E.M. film). To ensure both mechanical and electrical stability the

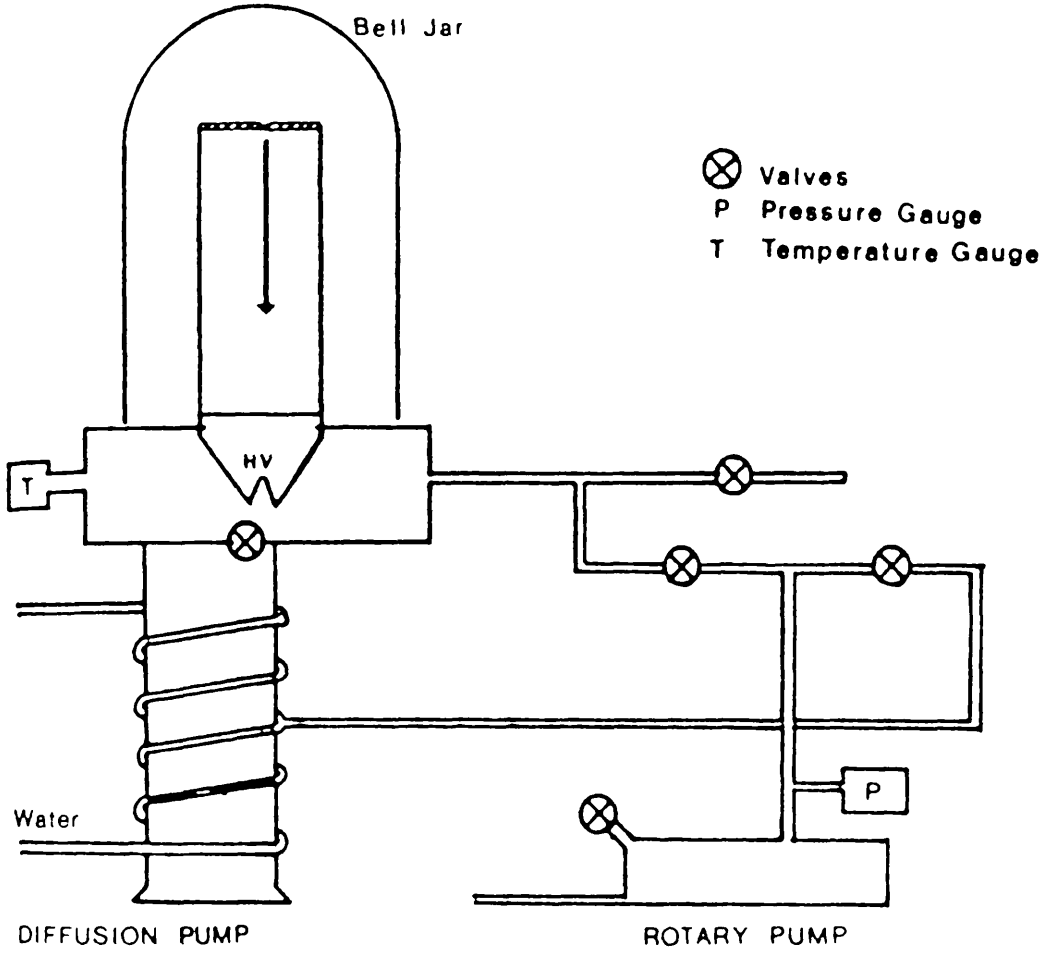

Figure 4.3

Edwards vacuum coating unit for preparation of "holey carbon film", by carbon evaporation, using spectroscopically pure graphite rods.

samples were placed in the specimen chamber and the accelerating voltage was applied for at least an hour before the microscope was operated. The specific manner in which the microscope was set up depended though, on which of the filaments was being employed at the time.

Every time the microscope was operated, certain routine alignment procedures were undertaken, involving such things as centering of the apertures and electron beam. The two stages of major importance and greatest difficulty during alignment of the microscope were setting the voltage center and correcting the objective lens astigmatism. Thus great care was taken to ensure that these were correctly aligned, the astigmatism being corrected at a magnification of 4-500000 times when micrographs of 300000 times magnification were required.

When observing a specimen using HREM, only the thin edge of wedge shaped particles protruding over holes in the carbon film were examined, making the micropores more easily observable. When recording an image, a focal series was taken at defocus values of 70-100nm underfocus, thus allowing for variations in specimen height and allowing the best of the micrographs to be later selected.

The micrographs that were obtained were examined using a graduated hand lens which was used to measure the distances between the centres of the pore walls. The resulting values were then put into different size intervals and used to construct histograms of the

micropore size distribution of the samples. The number of pores that were measured to produce the pore size distributions varied from sample to sample, however for the initial three samples it was in the order of one hundred pores, however for the rest of the carbons, larger samples of over two hundred pores were obtained.

4.6 Density Measurment

Densities were measured by pycnometry. The pycnometer that was used can be seen in figure 4.4. It was composed of a reservoir and a capillary tube held together by two metal springs. The diameter of the capillary (54.912×10^{-3}cm) and the volume of the pycnometer filled to a reference mark ($2.3441 cm^3$) had both previously been determined by using known weights of mercury.

In order to measure the density of a carbon it was first outgassed in a cell of the type used for immersion calorimetry. The outgassed weight of the carbon was then calculated and the cell immersed in the chosen liquid and broken. The wet carbon was then transferred to the reservoir of the pycnometer and some more liquid added. The pycnometer was next assembled and placed inside a glass tube standing in a water bath regulated to 0.02K using a Lauda MS thermostat. The apparatus was left for some time to allow the temperature to stabilise. Once this had occurred the difference between the height of the liquid in the capillary and the reference mark was measured with a cathetometer and the pycnometer was

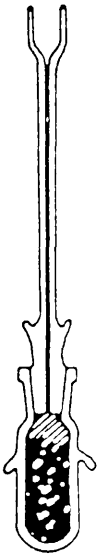

Figure 4.4

Pycnometer used to determine densities of coke samples.

weighed. Knowing the weight of the empty pycnometer and of the carbon and the combined weight of the pycnometer, carbon and liquid, the weight of the liquid could be determined. As the volume of the pycnometer, the diameter of the capillary and the density of the liquid were also known, it was a simple matter to calculate the density of the carbon.

These density measurements were carried out in benzene and its density was taken to be $0.8861 gcm^{-3}$ rather than that quoted on the bottle. This value was obtained by doing an experiment with no carbon present and is an apparent density as a result of the experimental set up.

4.7 Carbonisaton and Activation of Samples

The carbons were both carbonised and activated in a reactor of the type shown in figure 4.5. Such an apparatus allowed the activation of up to 13g of sample to be carried out. The reactor (1) was a stainless steel cylinder within which there was situated a cone (2) in which the samples were placed. Below the sample there was a quartz filter (3) through which the activating gas had to pass from the entry tube (4). This tube, constructed of stainless steel, was set in a number of spirals encircling the body of the reactor. This construction was to ensure that the gas was preheated before it reacted with the sample. There was an exhaust pipe (5) situated at the top of the reactor to enable the gas to leave. This whole assembly was placed within a furnace of the Solo type

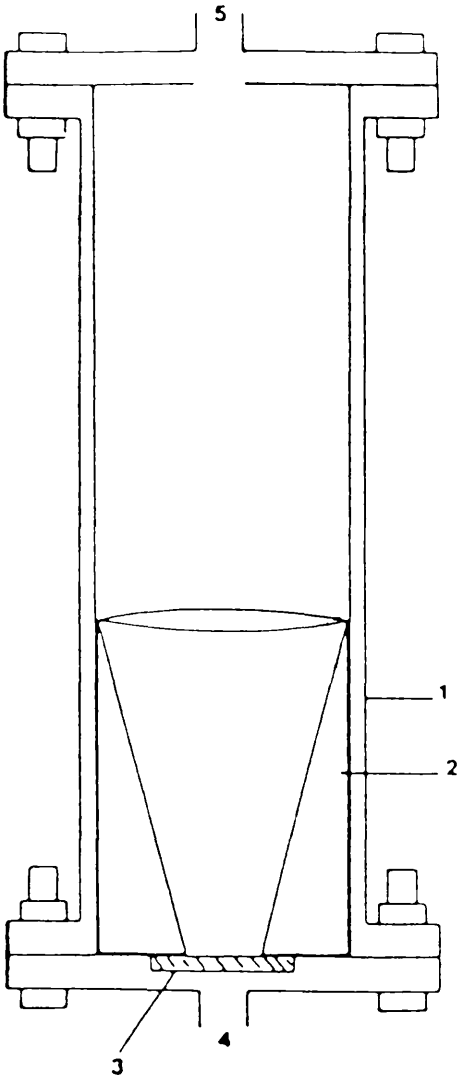

Figure 4.5

Reactor used for activation and carbonisation of samples.

which was capable of being heated to 1200°C.

The internal temperature of the reactor was measured using a chromel-alumel thermocouple connected to a voltmeter (Solatron 7045) and a chart recorder (Servoger 210). The flow of gas through the system was regulated using a GEC-Elliot flow rate meter.

The majority of activations were carried out on a commercial charcoal, "carbo-grill", which was denoted CEP-0 for the purpose of experiments. CEP-0 was a soft wood carbon of very low ash content with a helium density of only 2.00 g/cm and an external surface area of around $30m^2/g$. The carbon precursor was first crushed and sieved until it consisted of particles of between 0.6mm and 1.02mm. Around thirteen grams of this material were then placed inside the reactor which was then heated to 850°C over a period of around an hour. This temperature was maintained for a further hour before the furnace was allowed to cool. This whole procedure was carried out under a flow of nitrogen of 0.6-1.0 $lmin^{-1}$. After this carbonisation reaction had been carried out, the sample was reweighed (a weight loss of approximately 15% occurring in general) and then replaced into the reactor and again heated to 850°C under a flow of nitrogen. Only once the temperature had stabilsed was the nitrogen flow replaced by that of the activating gas, which in the present work was carbon dioxide at a flow rate of 1.5 $lmin^{-1}$. The amount of time the sample was subjected to the action of the carbon dioxide depended on the degree of

burn-off that was required. Once the desired time had been reached, the carbon dioxide was again replaced with nitrogen and the furnace was allowed to cool. The carbon was then weighed once more and from its weight loss during the activation reaction, the degree of burn-off could be calculated. The carbons produced from this precursor were denoted CEP-X, where X would be the degree of burn-off of that particular carbon.

The CEP-51 used in this work was activated under a flow rate of carbon dioxide of 1.5 $lmin^{-1}$ for a time of 129 minutes. The other CEP samples used in this work were produced by F. Kraehenbuehl and S. De Bernardini of the University of Neuchâtel.

The coke samples (Redcar I ex-tuyere and Redcar I feed) had to be activated for much longer times and at higher flow rates to achieve the same degree of burn-off as in the softer charcoals (table 4.1). These samples were also used in much smaller quantities, with 5g of material being used as opposed to the 13g used with the CEP series.

Table 4.1 Degrees of burn-off and the corresponding activation times and gas flow rates for CEP-51 and the coke samples.

SAMPLE	B-O(%)	CO_2 FLOW($lmin^{-1}$)	ACTIVATION(min)
CEP	51	1.5	129
REDCAR I ET	8	1.5	150
REDCAR I ET	22	3.0	360
REDCAR I ET	39	4.5	720
REDCAR I FEED	7	1.5	120
REDCAR I FEED	19	3.0	760

RESULTS AND DISCUSSION

5.1 Studies of Samples CEP-18, CEP-35 and CEP-49

The preliminary studies in this work were carried out on a series of three carbons. Of these samples, CEP-18 and CEP-35 had been previously characterised by Kraehenbuehl et al. (1986) and CEP-49 had been studied by Ballerini (1986), both of whom used standard gravimetric and volumetric apparatus for adsorption experiments. The samples were also immersed into various organic liquids using a calorimeter of the Calvet type to obtain size distributions of the micropores present in the specimens.

The series of carbons was examined using high resolution electron microscopy. The initial microscopical studies were carried out using standard carbon coated electron microscopy grids. Such grids however, were not ideal for imaging active carbon samples as is illustrated in plate 1. The presence of the underlying sheet of carbon made it difficult to observe clearly the porous structure of the carbon that was actually being studied. After the problem associated with this type of microscope grid had been realised, grids coated with holey carbon film were used in preference. This action vastly improved the definition at the edges of the specimen that was under examination.

The three carbons in the series were initially investigated to give a qualitative analysis of their structural features. The sample to be studied first was

CEP-18. A characteristic of this carbon was its structural heterogeneity, although such a feature is not unexpected for a carbon obtained from a wood source. The heterogeneity is clearly apparent in the following set of micrographs. Plate 2 shows extensive lattice imaging, the fringes occurring in bands of various widths. The spacing between the lattice fringes is 0.335nm, i.e. a graphitic spacing, however they do not run in a continuous straight line but undergo a series of bends and directional changes. The structure contains a number of defects. Lattice fringes can be seen diverging from each other and the presence of edge dislocations can be observed.

Plate 3 however, although of the same sample, shows no particularly ordered graphitic structure. In the thicker region of the sample there is what appears to be a "swirling" pattern of lattice fringes. This is an extremely defective structure. It appears to consist of both short fringes and also of layer planes of considerable length. Although there is some degree of parallelism among the planes, it does not continue for any great distance along a particular fringe. Such a structure would, no doubt, leave many voids within the sample which could be considered to be micropores. Whether such porosity would be open or not, it is not possible to predict from the micrographs. The upper region of the micrograph shows a grainy "ribbon-like" structure and it is in regions such as this, at the edge of the sample, that the open microporosity becomes apparent. The micropores appear as breaks in contrast at the sample

edge. Some pore entrances have been indicated by arrows, however many more can also be observed all around the sample edge.

The length and shape of the micropores vary considerably as would be expected from visibility criteria discussed previously (Fryer, 1979). The twisting of a pore would move its walls from a position perpendicular to the electron beam, altering the contrast and rendering it impossible to image the pore along its full length. Thus it is not possible to make definite measurements of the pore length. However, some qualitative assessment of pore shape may be obtained. Some micropores appear as short slits whereas others continue for considerable distances within the sample, turning through sharp angular bends. Branches are also apparent in many pores. The entrances to most of the pores appear to be at their ends, however some of the pores are accessible at some point along their length other than at the end. Another feature of the pores that can be observed is that their width does not always remain constant along their length but can vary considerably.

The porous "ribbon-like" structure and the "graphitic" structure do not simply occur in separate areas as shown in the previous micrographs but may be found together as illustrated in plates 4 and 5. These two plates show exactly the same area but at different defocus conditions. Plate 4 shows a microporous structure not unlike that of plate 3, however on further defocusing the objective lens

the resulting image, plate 5, shows the presence of lattice fringes within the sample. The fringes, with spacings of 0.33 to 0.35 nm, occur in bands of varying thickness and run in many directions throughout the sample. Extremely short range fringes are also present, covering almost all of the right hand side of the specimen.

The variation in structure throughout the sample is illustrated more graphically in plate 6. In this area there are both porous and "graphitic" regions. However, there is also a third structural type present. This is shown more clearly in plates 7 and 8, enlargements of the previous micrograph. It is apparent that there are many lattice fringes occurring in bands much thinner than those of the previous micrographs. The bands consist of approximately 2 to 5 layer planes in thickness, with pairs of planes being the predominant feature. In plate 7 there is even what appears to be a single layer plane visible. From all the micrographs discussed above it would seem that CEP-18 is an extremely heterogeneous and complex material.

On examining CEP-35, similar features were observed, except for the extensive graphitic type structure. Although if the mechanism for carbon activation is to be accepted as a burning out along the layer planes then lack of extensive development of lattices would seem reasonable in a carbon of higher burn-off. The "ribbon-like" porous structure was still apparent, plate 9, as were the regions

of relatively short range lattice fringes, plate 10. These fringes seemed to favour groups of 4-5 rather than the pairs found with CEP-18. Another point worth noting was that some of the porous regions had a slightly different appearance to those described previously. Plate 11 shows such a region. The layer planes appear to be a little straighter than in the previously studied regions with the whole area perhaps looking a little more ordered.

CEP-49 was similar in appearance to the previous samples and possessed similar features. For this sample some areas of fairly extensive lattice structure were observed, plate 12, although such areas were by no means common to the sample.

After this initial qualitative study of the structural features of the samples had been made, the microporous structure was examined in greater detail so that a comparison study of the micropore size distributions obtained from the adsorption and immersion studies of Kraehenbuehl et al. (1986) and Ballerini (1986) could be made with the size distributions obtained by making direct measurements from electron micrographs.

In order to create micropore size distributions from the results obtained by high resolution electron microscopy, many pores were measured from a number of micrographs. Only those pores situated at the sample edge were measured and it was the width close to the entrance of the pores that was taken to be the pore width. When measuring the

pores it was the distance between the centres of the pore walls that was obtained. The values produced by using this method were grouped into size intervals. The percentage of pores in each size grouping that was obtained for the samples CEP-18, CEP-35 and CEP-49 can be seen in table 5.1.

Table 5.1 Percentage of pores in different pore width ranges obtained from HREM for CEP-18, CEP-35 and CEP-49. *

Sample	Pore Widths (nm x 10^{-1})					
	4.01-5	5.01-6	6.01-7	7.01-8	8.01-9	9.01-10
CEP-18	3.3	27.9	32.8	31.1	3.3	1.6
CEP-35	7.7	23.1	28.2	28.2	12.8	0.0
CEP-49	7.6	17.9	36.8	15.1	18.8	3.8

The figures in table 5.1 were used to construct histograms displaying the micropore size distribution of samples CEP-18, CEP-35 and CEP-49 (figures 5.1 to 5.3 respectively). The two carbons of lower burn-off, CEP-18 and CEP-35 (figures 5.1 and 5.2) show quite broad distributions. The pore sizes range mainly from around 0.5 to 0.8 nm for CEP-18 with a slightly wider range for CEP-35. The main bulk of the pores of CEP-49 lie in a similar size range, however there is an obvious peak in the 0.6 to 0.7 nm size range.

In their present form there was not a great deal of

* The error on these and all subsequent HREM results is ±1%

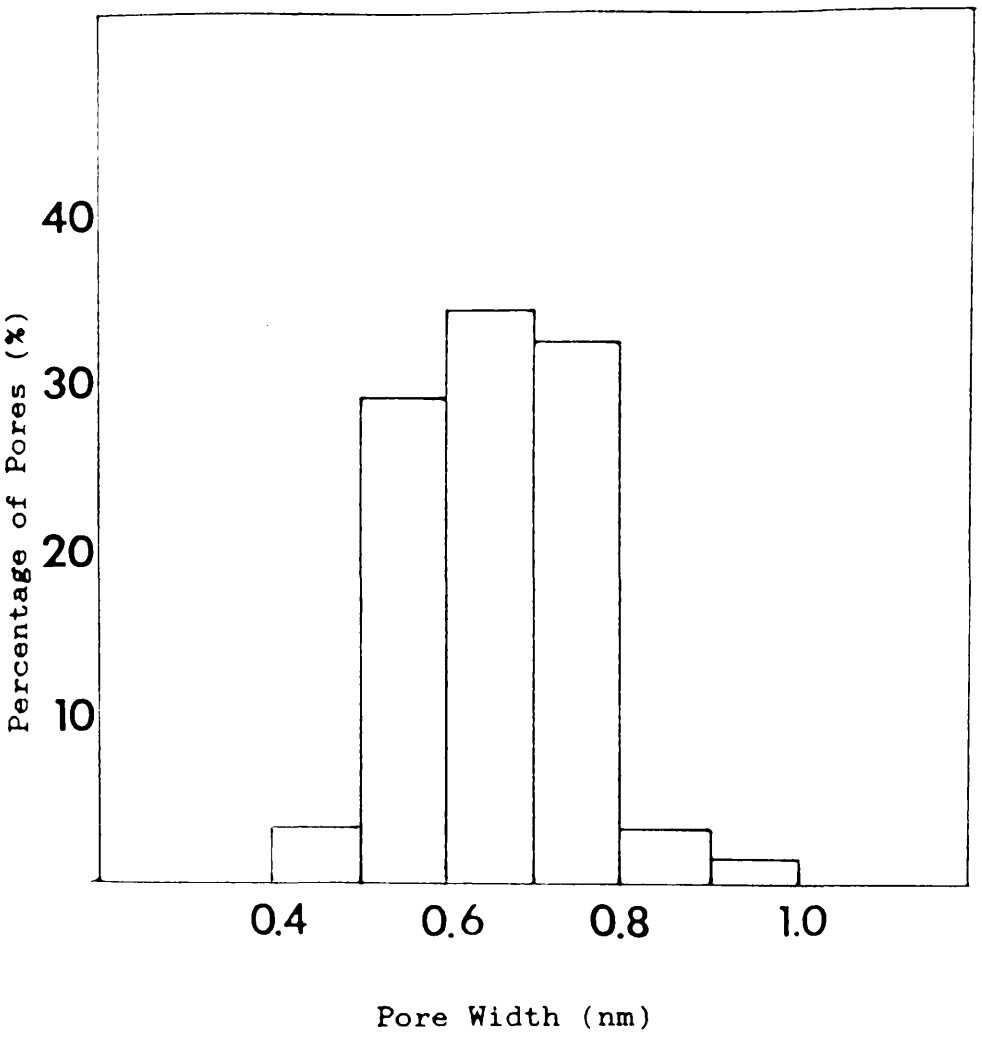

Figure 5.1

Micropore size distribution of CEP-18 that was initially obtained from HREM.

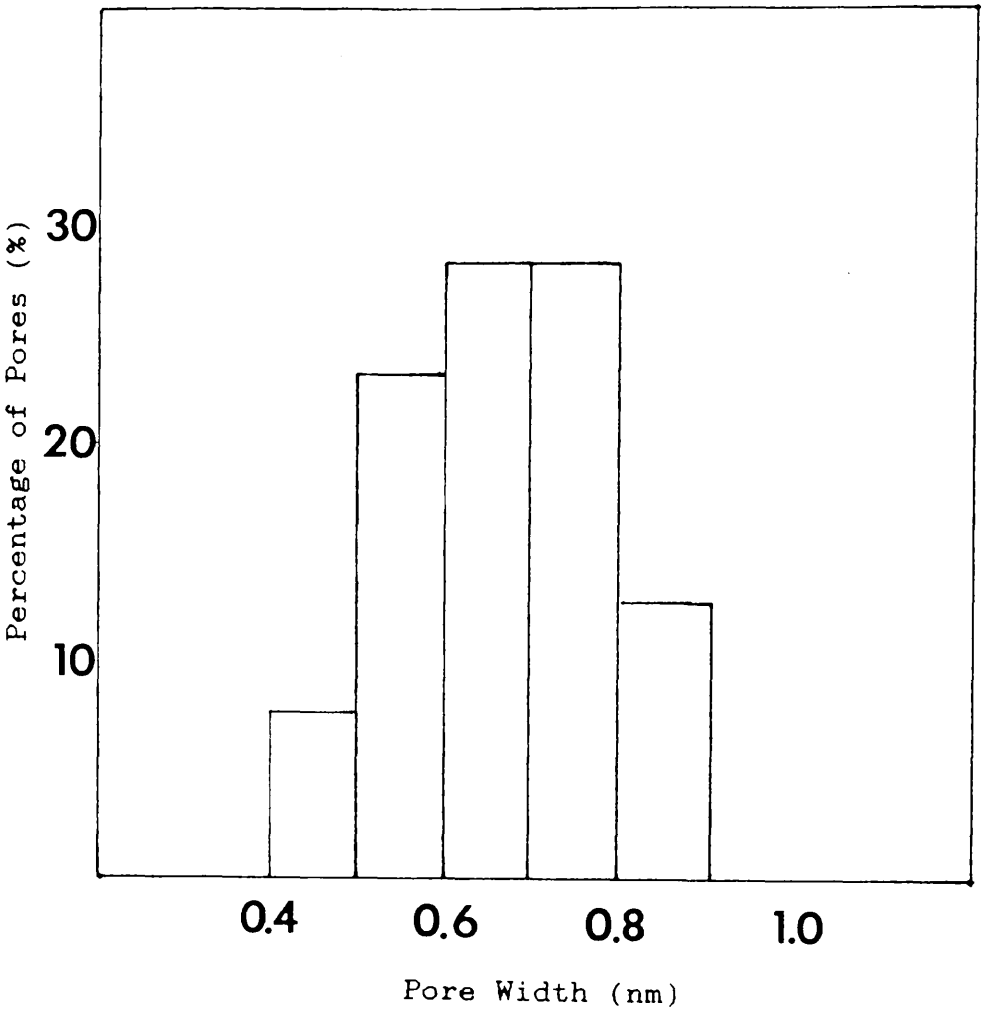

Figure 5.2

Micropore size distribution of CEP-35 that was initially obtained from HREM.

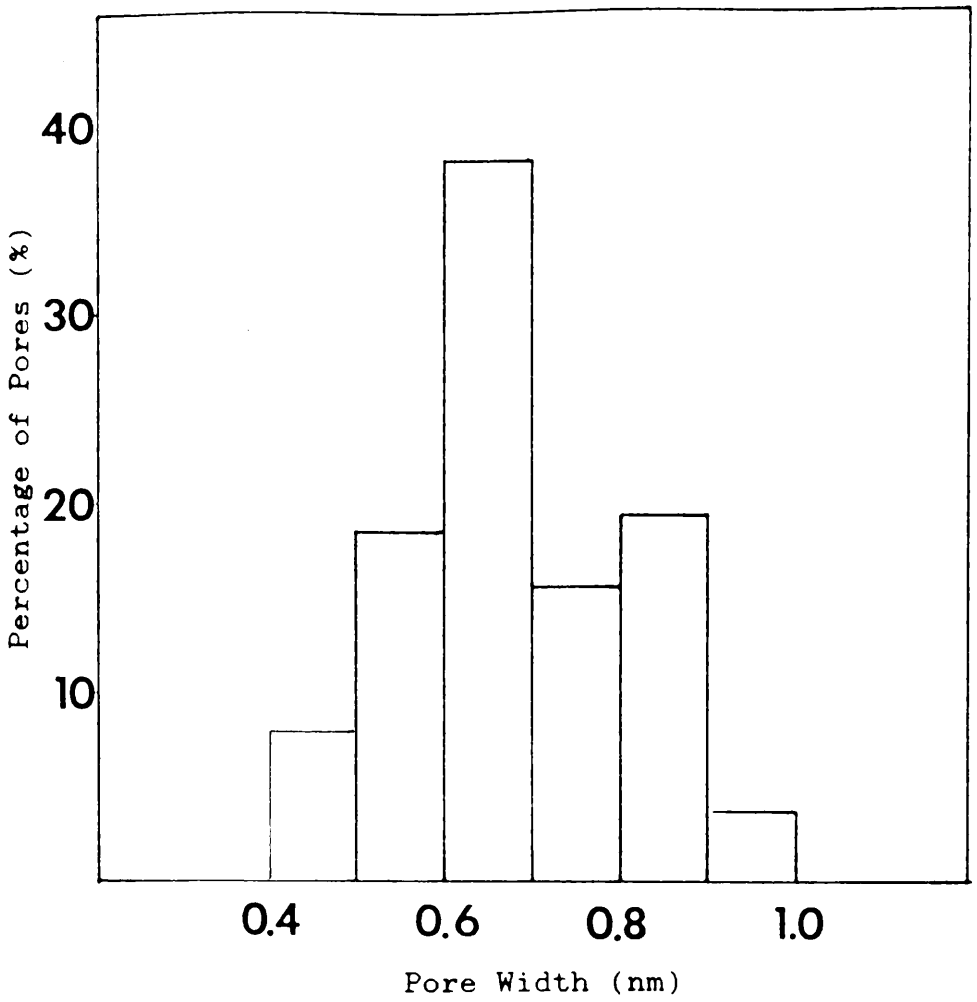

Figure 5.3

Micropore size distribution of CEP-49 that was initially obtained from HREM.

agreement between the size distributions obtained from immersion calorimetry and those obtained from high resolution electron microscopy. This is because values obtained for the pore sizes using high resolution electron microscopy cannot be compared directly with those deduced from immersion calorimetry, as the two techniques do not measure exactly the same quantity. Immersion calorimetry - as with all adsorption techniques - measures the space inside a pore that is accessible to the adsorbate, electron microscopy, on the other hand, measures the internuclear distance between two carbon sheets. In consequence, an adjustment must be made to the microscopy results if they are to agree with those obtained from immersion studies.

Unfortunately, the situation is not quite this simple because atomic radius is a variable quantity and the heat of adsorption of a gas in a pore implies that there is some interaction between the surface and adsorbate. The normal non-bonded (Van der Waals) radius of carbon is 0.17 nm, although small variations on this occur, e.g. in a hexagonal close packed environment such as graphite, the dimension is 0.168 nm and in aromatic hydrocarbons such as perylene, it is 0.174 nm.

Everett and Powl (1976) undertook theoretical calculations on the adsorption of gases by microporous solids. These calculations were carried out for both slit-pores and cylindrical pores and longer range effects such as whether a carbon layer was isolated or part of a graphitic matrix

were also considered. They claimed that the effective slit width W_e of a micropore would be given by:

$$W_e = W_d - 0.34nm$$

Where W_d is the internuclear distance between the carbon atoms constituting the micropore walls and the value 0.34nm is twice the effective radius of a carbon atom. However, they claimed, quantities calculated in this way would not reflect the available pore width W_a. This is due to the fact that because of the adsorption forces, the collision distance of a molecule with the surface of the pore would be reduced.

Using noble gases as adsorbates, Everett and Powl applied their calculations, using both 10:4 and 9:3 potentials, to experiments involving a number of carbons. The results that they obtained (Table 6, Everett and Powl, 1976) suggested that $W_d - W_a$ was approximately 0.23nm when the 10:4 potential was assumed and 0.133nm when the 9:3 potential was utilised for experiments involving argon and krypton. In the case of xenon, slightly smaller values were obtained although Everett and Powl stated that the error on these results was larger than for the other gases.

The 10:4 potential relates to the interaction of a gas phase molecule with a single solid lattice plane, whereas in the case of the 9:3 potential, the gas phase molecule is interacting with a semi-infinite slab of solid.

Consideration of the structure of active carbons has led to the suggestion (Everett and Powl, 1976; McEnaney, 1988) that it is the 10:4 potential that is most applicable to real samples, although this is a highly idealised condition which does not take full account of either the highly complex nature of carbons such as the presence of layer edges, heteroatoms and functional groups or the interactions that occur between the molecules that are adsorbed in the pores.

In view of the above observations, the approximate value 0.2nm was selected to be subtracted from the pore width values obtained from high resolution electron microscopy. This value of 0.2 nm was subtracted from the pore width intervals of table 5.1 and the histograms showing the micropore size distributions were reconstructed using the new values. This subtraction was also carried out in all subsequent microscopy results and any values quoted will be those to which the correction has already been made.

The reconstructed histograms were then superimposed on those histograms previously obtained by Kraehenbuehl et al. (1986) for CEP-18 and CEP-35 and by Ballerini (1986) for CEP-49. The results of this comparison can be seen in figures 5.4 to 5.6. The agreement for CEP-18 and CEP-35, the two carbons of lower burn-off (figures 5.4 and 5.5 respectively) is now much better. The maxima for the samples from each of the techniques coincide well and both samples do show the broad distribution that was found using immersion calorimetry although the fit for CEP-35 is

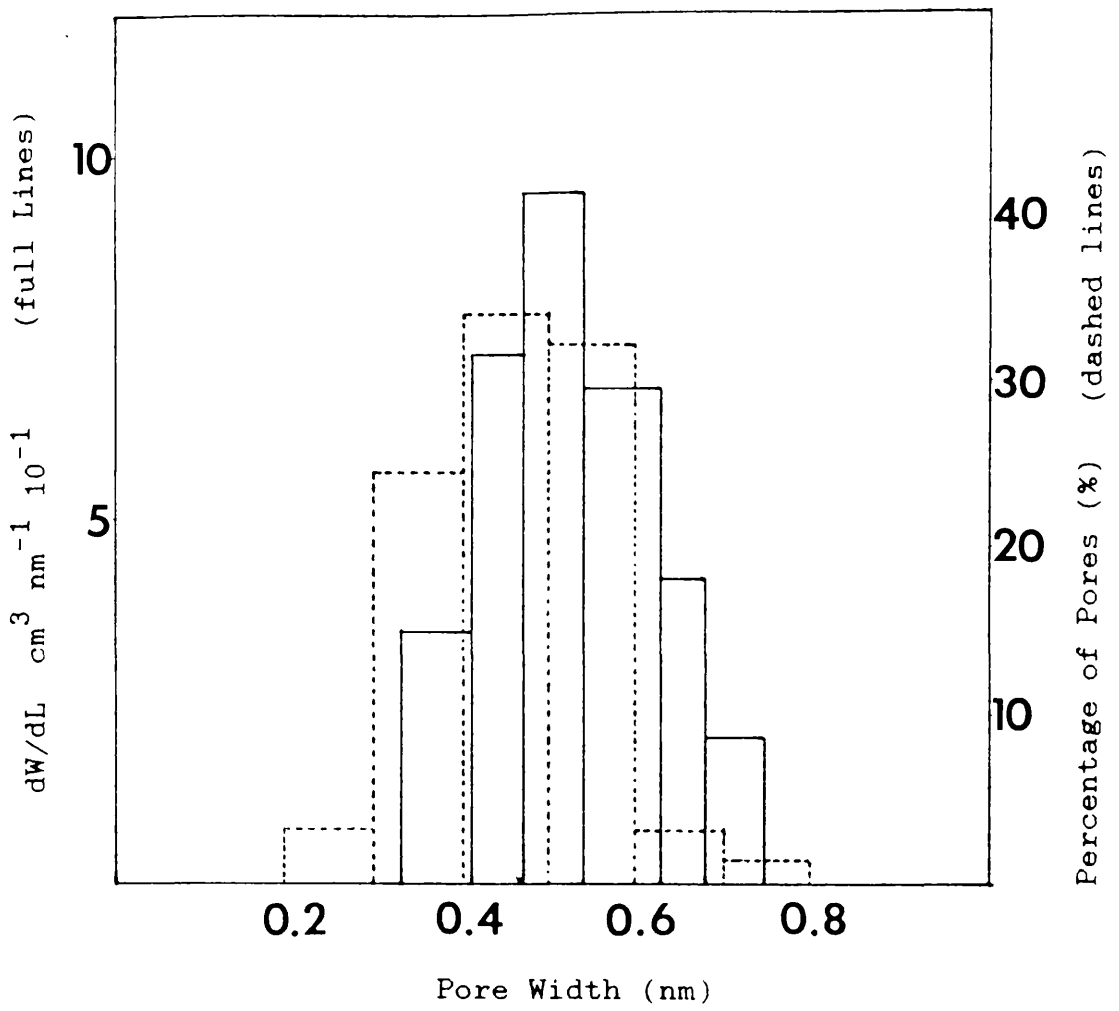

Figure 5.4

Micropore size distribution of CEP-18 obtained from immersion calorimetry and HREM (Full and dashed lines respectively).

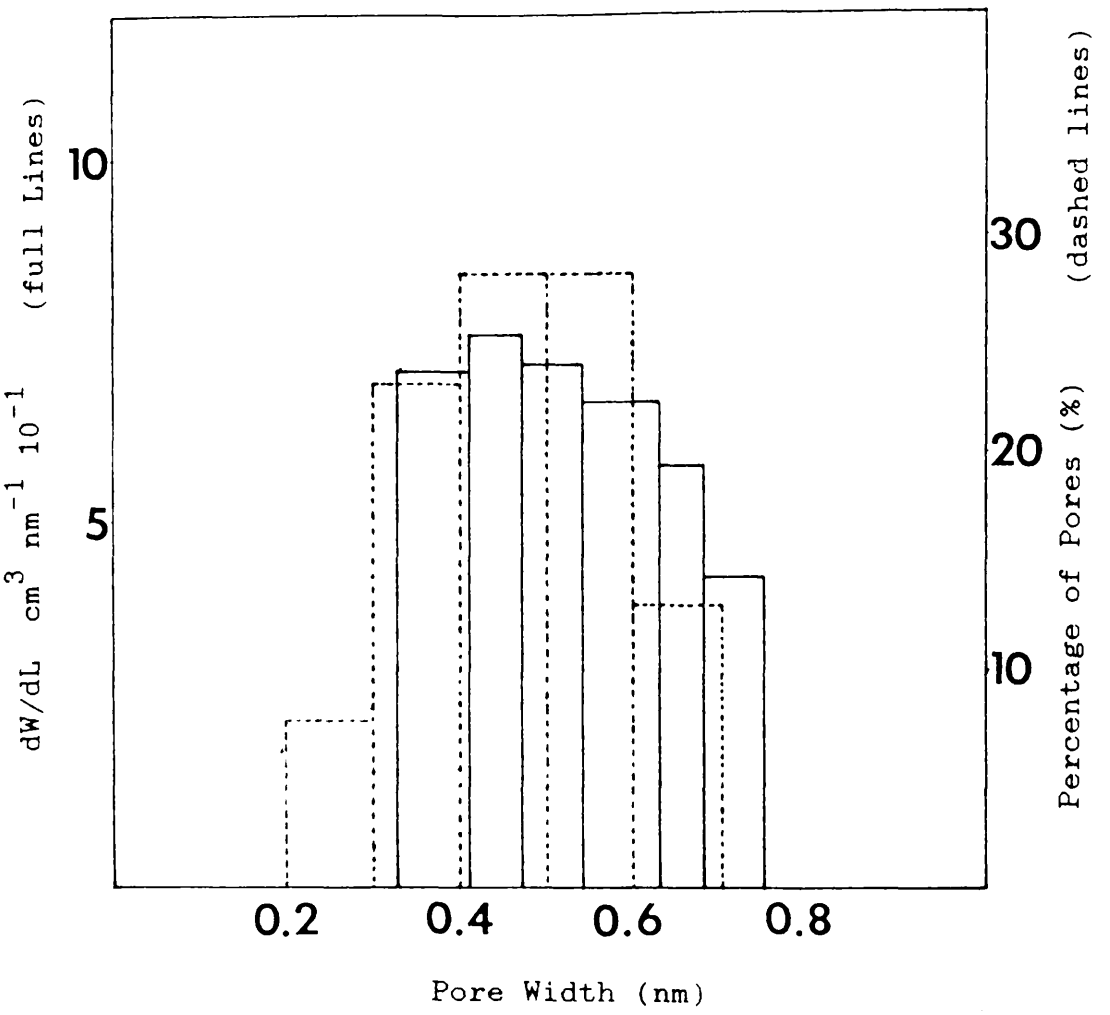

Figure 5.5

Micropore size distribution of CEP-35 obtained from immersion calorimetry and HREM (Full and dashed lines respectively).

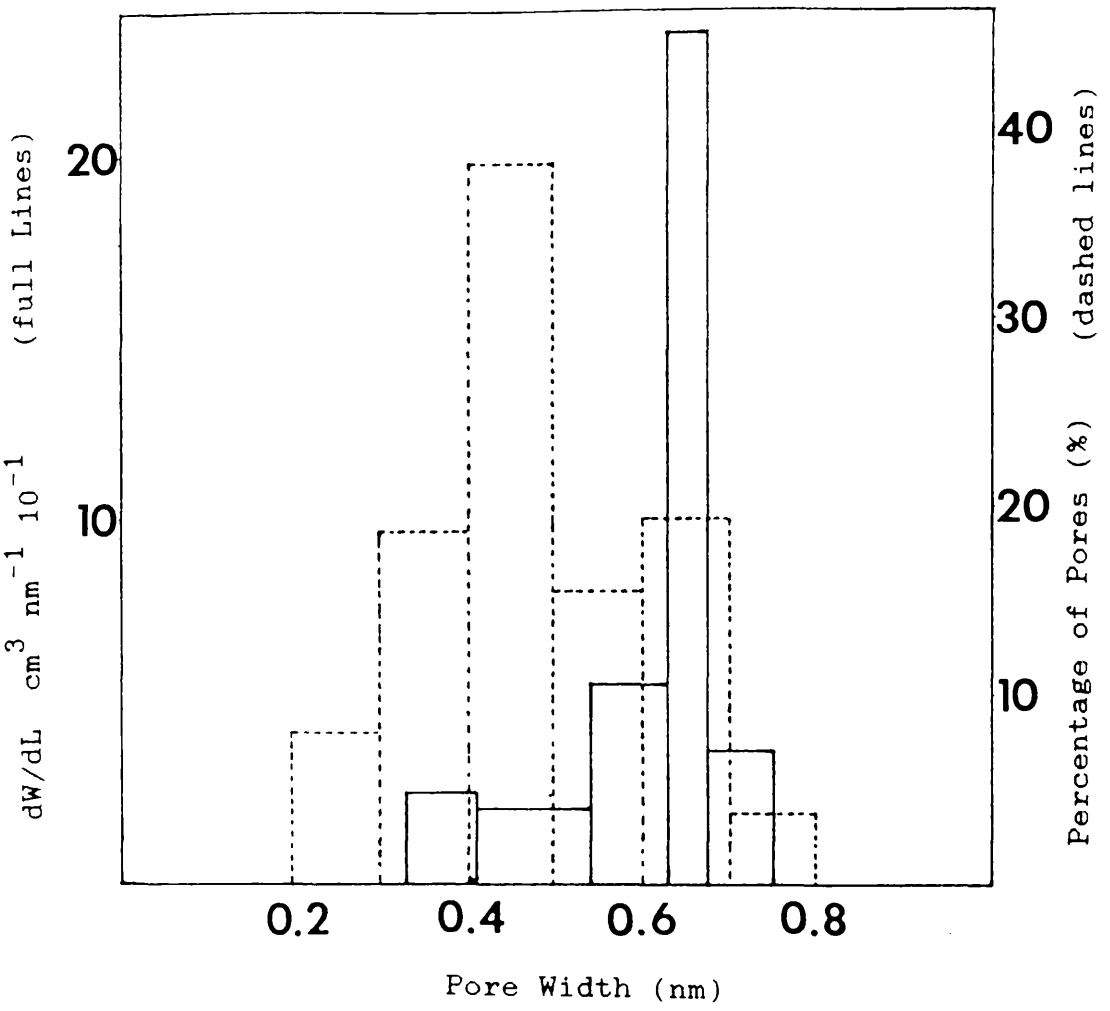

Figure 5.6

Micropore size distribution of CEP-49 obtained from immersion calorimetry and HREM (Full and dashed lines respectively).

a little better than that for CEP-18. The distribution derived from the microscopy results for CEP-18 does not peak to the same extent as that produced from immersion calorimetry and the maximum from the microscopy results is shifted slightly to a lower value. The pores greater in size than 0.6 nm do not show up well in the CEP-18 values obtained from microscopy measurements. However when it is considered that immersion calorimetry is a macrotechnique which gives a pore size distribution averaged over many pores, whereas with high resolution electron microscopy, individual pores are imaged and the technique is of course, therefore less statistically sound, this agreement between the techniques is good. In fact, for these early samples, relatively few pores were measured, so it is hardly surprising that a more accurate fit was not obtained.

Although the precise figure of 0.2 nm which was subtracted from the microscopy results is unlikely to be accurate for all situations, these results do seem to point to the validity of the Everett and Powl treatment. Had the Van der Waals value of 0.34 nm been subtracted from the CEP-18 results rather than the Everett and Powl value of 0.2 nm, then only 25% of the pores that were visible to microscopy would have been over 0.41 nm (i.e. large enough to accommodate a benzene molecule). This would mean that this small percentage of the porous structure accounts for a pore volume of 0.223 cm^3g^{-1}.The pores in the resulting size distribution would range mainly in the interval of 0.15 to 0.45 nm. This would mean that for adsorption of

the larger molecules into which the sample was immersed such as perchlorocyclopentadiene to occur, these pores would have to swell to almost twice their size. The occurrence of such processes would seem unlikely in a carbon of such a low degree of burn-off.

In the case of the carbon of higher burn-off, CEP-49 (figure 5.6) the agreement is less good. Both techniques do show a large peak rather than the broad distributions of the previous two samples, however the maximum found from microscopy occurs between 0.4-0.5 nm whereas that of immersion calorimetry is at a value of around 0.2 nm greater. A possible explanation for this phenomenon may be that the layer planes exfoliate in the presence of a gas or liquid and collapse under vacuum - as exists within the electron microscope. The ability of a material to undergo exfoliation depends very much on the flexibility of the layer planes. As CEP-49 is of higher burn-off than the other two samples, it would be expected that it would contain more flexible layer planes which would undergo exfoliation more easily. This is because the higher the burn-off, the "looser" the structure due to the fact that more of the carbon has been eaten away by the activating gas. This would explain why a deviation was observed for CEP-49 but not for the lower burn-off carbons CEP-18 and CEP-35.

In the above study only the microporosity of the sample was discussed. This is because adsorption results showed the external surface areas of these carbons to be

negligible and in examining the micrographs, this point was backed up by the fact that no mesoporosity was apparent.

5.2 Study of Sample CEP-0

After these initial studies of carbons CEP-18, CEP-35 and CEP-49 by high resolution electron microscopy had been carried out, further CEP samples were prepared and characterised by both this technique and by adsorption and immersion studies. As this work relates mainly to carbons of the CEP series, if was decided to examine CEP-0, the carbon of 0% burn-off. This is the last of the specimens dealt with here to have been previously characterised by Kraehenbuehl et al. (1986).

The micrographs of this sample yielded the results shown in table 5.2.

Table 5.2 Percentage of pores in different pore width ranges obtained from HREM for CEP-0

Sample	Pore Widths (nm x 10^{-1})					
	3.01-4	4.01-5	5.01-6	6.01-7	7.01-8	8.01-9
CEP-0	8.8	59.1	22.2	7.4	1.5	1.0

The values in table 5.2 were used to construct a histogram of the micropore size distribution which can be seen

displayed along with the distribution obtained from immersion calorimetry in figure 5.7. This diagram shows excellent agreement between the techniques. The large peaks coincide exactly in the 0.4-0.5 nm range and the spread of the distributions match well with neither technique displaying the presence of much porosity in either the lower or higher pore width ranges. This result adds much stronger evidence for the validity of the Everett and Powl model and of the utilised value of 0.2nm.

5.3 Studies of Saples CEP-17, CEP-31 and CEP-*35

To examine further the correlation between the two techniques, some more CEP samples were prepared. CEP-17, CEP-31 and CEP-*35 were prepared by De Bernardini at Neuchâtel University. The CEP-17 was first investigated using immersion calorimetry. The immersion enthalpies, their corresponding pore volumes and the variation in volume with pore width can be found in table 5.3.

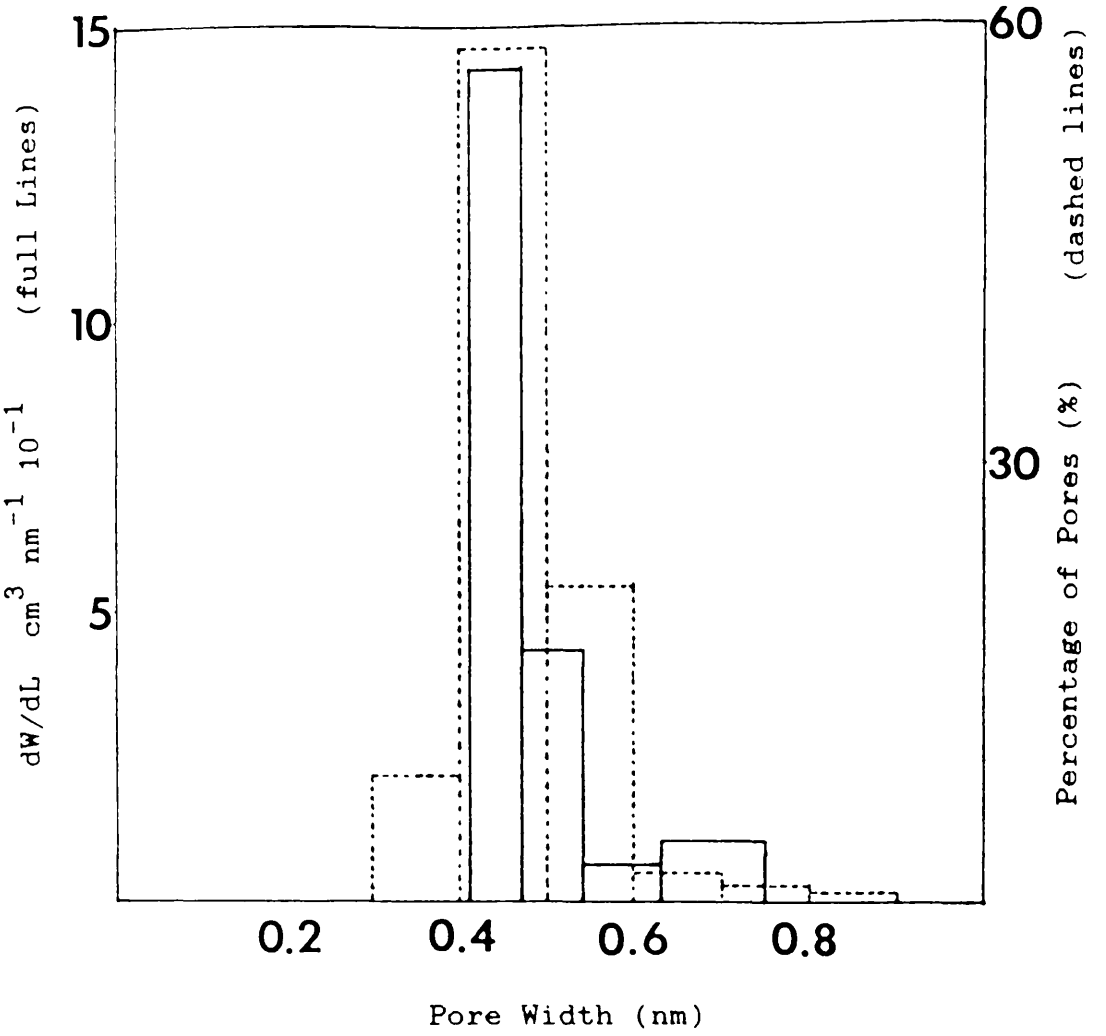

Figure 5.7

Micropore size distribution of CEP-0 obtained from immersion calorimetry and HREM (Full and dashed lines respectively).

Table 5.3 Immersion results for sample CEP-17

Probe	ΔH_i (Jg^{-1})	W(L) (cm^3g^{-1})	L(nm)	dW(L)	dL	dW(L)/dL *
CH_2Cl_2	116.1	0.266	0.33			
				0.029	0.08	0.36
C_6H_6	106.6	0.237	0.41			
				0.116	0.13	0.89
C_6H_{12}	43.9	0.121	0.54			
				0.045	0.09	0.50
CCl_4	32.7	0.076	0.63			
				0.014	0.05	0.28
$C_{10}H_{16}$	25.3	0.062	0.68			
				-0.001	0.07	-0.01
C_5Cl_6	29.6	0.063	0.75			

In order to calculate the volume terms in table 5.3 and all other volumes in this work from immersion enthalpies, the physical constants of the molecular probes shown in table 5.4 were employed.

Table 5.4 Physical constants of molecular probes.

Probe	V_m (cm^3mol^{-1})	β	α (x $10^{-3}K^{-1}$)	L(nm)
CH_2Cl_2	64.02	0.66	1.34	0.33
C_6H_6	88.91	1.00	1.24	0.41
C_6H_{12}	108.10	1.04	0.96	0.54
CCl_4	96.50	1.05	1.22	0.63
$C_{10}H_{16}$	158.75	1.70	1.02	0.68
C_5Cl_6	159.30	1.91	1.17	0.75

In addition to the physical constants listed in table 5.4, * L values obtained from Kraehenbuehl et al. (1986).

it was necessary to know the characteristic energy of the sample, E_o in order to calculate the volume terms W(L) for CEP-17. A value of 33 $kJmol^{-1}$ was employed in the calculations as this was the value found by Kraehenbuehl et al. in their characterisation of CEP-18. It was thought that with the closeness in the degrees of burn-off of these two samples, their characteristic energies should also be similar.

In order that the calorimetric results obtained here for CEP-17 could be compared with those of CEP-18, the CEP-18 results had to be recalculated, removing the results for C_6H_5Cl, leaving the histogram unchanged except that the bands from 0.41-0.47 nm and 0.47-0.54 nm were replaced by a single band in the region 0.41-0.54 nm. This recalculation had to be undertaken because in the immersion results obtained in the course of this work, the C_6H_5Cl values were thought to be unreliable and were therefore omitted. Other histograms constructed by Kraehenbuehl et al. were treated in a similar manner if they were to be compared directly with those obtained in the present work where C_6H_5Cl was not used.

Figure 5.8 shows the micropore size distributions obtained from immersion calorimetry with CEP-17 and CEP-18. These appear to be quite similar. The CEP-18 shows a slightly broader distribution but both samples do have their maximum value in the same region. The similarity of these distributions seems to validate the assumption as to the value used for the characterisic energy.

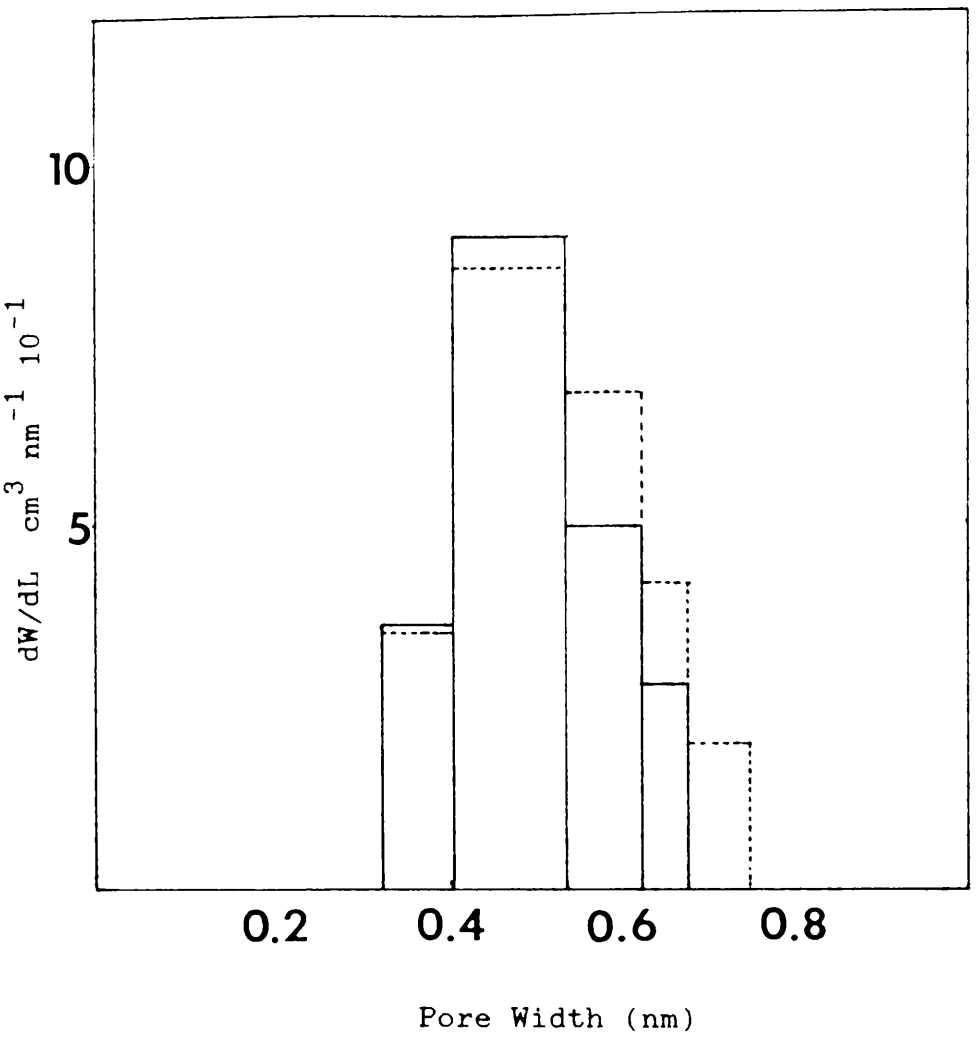

Figure 5.8

Micropore size distribution, from immersion calorimetry, of CEP-17 and CEP-18 (full and dashed lines respectively).

The CEP-17 had a similar structural appearance to the other CEP samples described earlier. Plate 13 shows a typical example of a micrograph of this specimen with the porous "ribbon-like" carbon being most clearly apparent in the top right of the picture. Again in this micrograph, short range lattice structure is visible with the planes occurring predominantly in pairs. Another feature worth noting is that seen in plate 14. The entire particle is covered with short range fringes. However, within the boxed area the order appears to be of longer range. This becomes clearer in plate 15, an enlargement of the boxed area. Lattice lines can now be clearly seen running in a variety of directions. There is quite a large variation in the spacing of the lattices (0.33 to 0.42nm). Such an appearance is unusual compared with the other carbons studied in the present work. In the case of most of the carbons, groups of lattice fringes of more than around 5 layer planes in thickness tend to occur in obvious bands which appear to be separate from the sample as a whole unlike this area where the lattice structure appears to be an integral part of the particle. When the pores found in the micrographs of this sample were measured, the results displayed in table 5.5 were obtained.

Table 5.5 Percentage of pores in different pore width ranges obtained from HREM for CEP-17

Sample	Pore Widths (x 10^{-1} nm)				
	3.01-4	4.01-5	5.01-6	6.01-7	7.01-8
CEP-17	14.1	53.5	17.4	12.0	3.0

The micropore size distributions that were constructed from tables 5.3 and 5.5 can be seen in figure 5.9. For this sample there is excellent agreement between the two techniques. The two distributions show an excellent overlap and both show a large peak in the 0.4 to 0.5 nm size range. The closeness of the overlap shown in this diagram presents even stronger evidence for the validity of the Everett and Powl treatment and suggests that the two techniques do in fact show a true representation of the microporous structure.

The next carbon to be studied was CEP-31. For this carbon to be characterised using immersion calorimetry, an adsorption experiment had first to be carried out to determine the value of the characteristic energy that would be used in calculations. Before an isotherm could be run on the CEP-31, the equipment was first checked using a standard because of earlier apparatus problems that had been incurred. The standard that was employed was a Norit-125 carbon with benzene being used as an adsorbate. The adsorption experiment yielded a standard type I isotherm

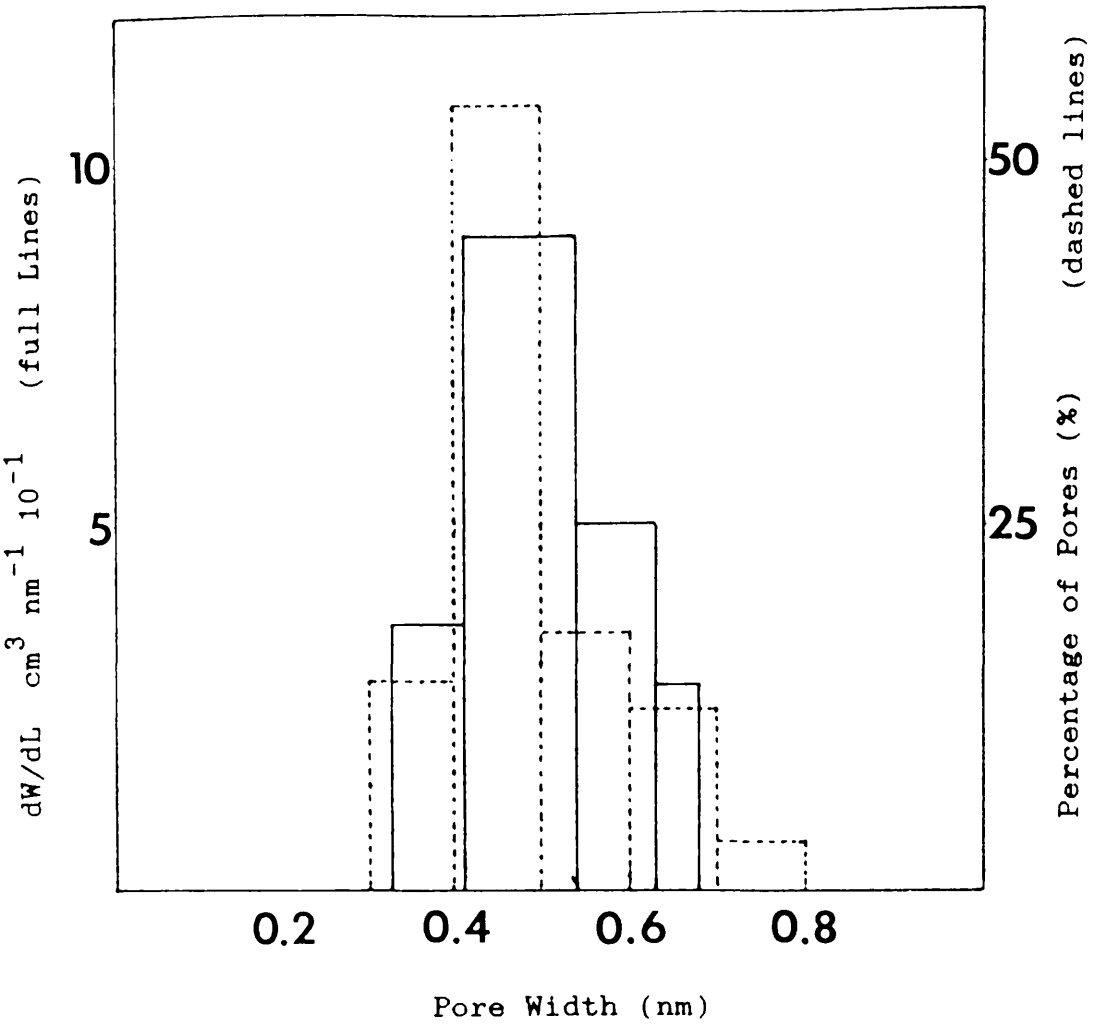

Figure 5.9

Micropore size distribution of CEP-17 obtained from immersion calorimetry and HREM (Full and dashed lines respectively).

which was used to construct a Dubinin-Radushkevich plot. From this the value 0.621 cm^3g^{-1} was obtained for W_o with the slope of the plot giving a value of 0.1301 x 10^{-5} K^{-2} for B. These results compared well with the standard values of 0.623 cm^3g^{-1} and 0.1305 x 10^5 K^{-2} for W_o and B respectively. The precision of the adsorption apparatus now having been ensured, an experiment using CEP-31 could be undertaken. The isotherm resulting from adsorbing benzene onto this sample is shown in figure 5.10. The results obtained for the quantity of benzene adsorbed and the relative pressures were used to construct the Dubinin-Radushkevich representation which can be seen in figure 5.11. This representation shows a downward deviation in the region of low relative pressure which is generally considered to illustrate some type of constriction in the micropore system which is preventing the adsorption of the quantity of gas expected, at low relative pressure. From the linear portion of the representation a value of 0.301cm^3g^{-1} was obtained for W_o from the intercept with the y-axis. The slope yields a value of 0.3903 x 10^{-6} K^{-2} for B, which can be converted to give the value 30.65 $kJmol^{-1}$ for E_o, the characteristic energy. The characteristic energy being known, it was then possible to make calculations on the results from the immersion experiments that were carried out.

Using the above values for W_o and E_o and the physical constants for benzene in the equation,

$$\Delta H_i = \beta E_o W_o (1+\alpha T)\sqrt{\pi}/2V_m$$

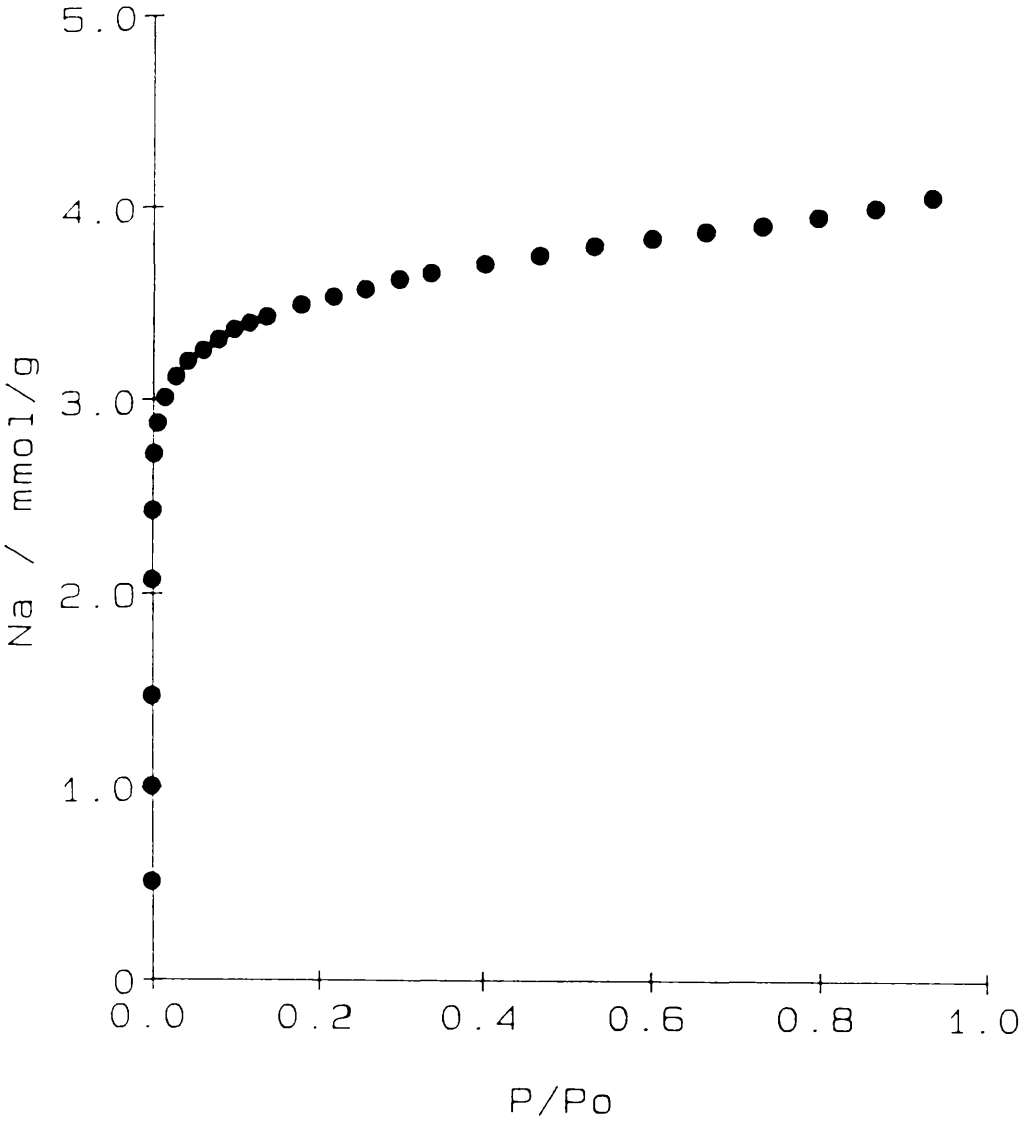

Figure 5.10

Adsorption isotherm of C_6H_6 on CEP-31 at 293K.

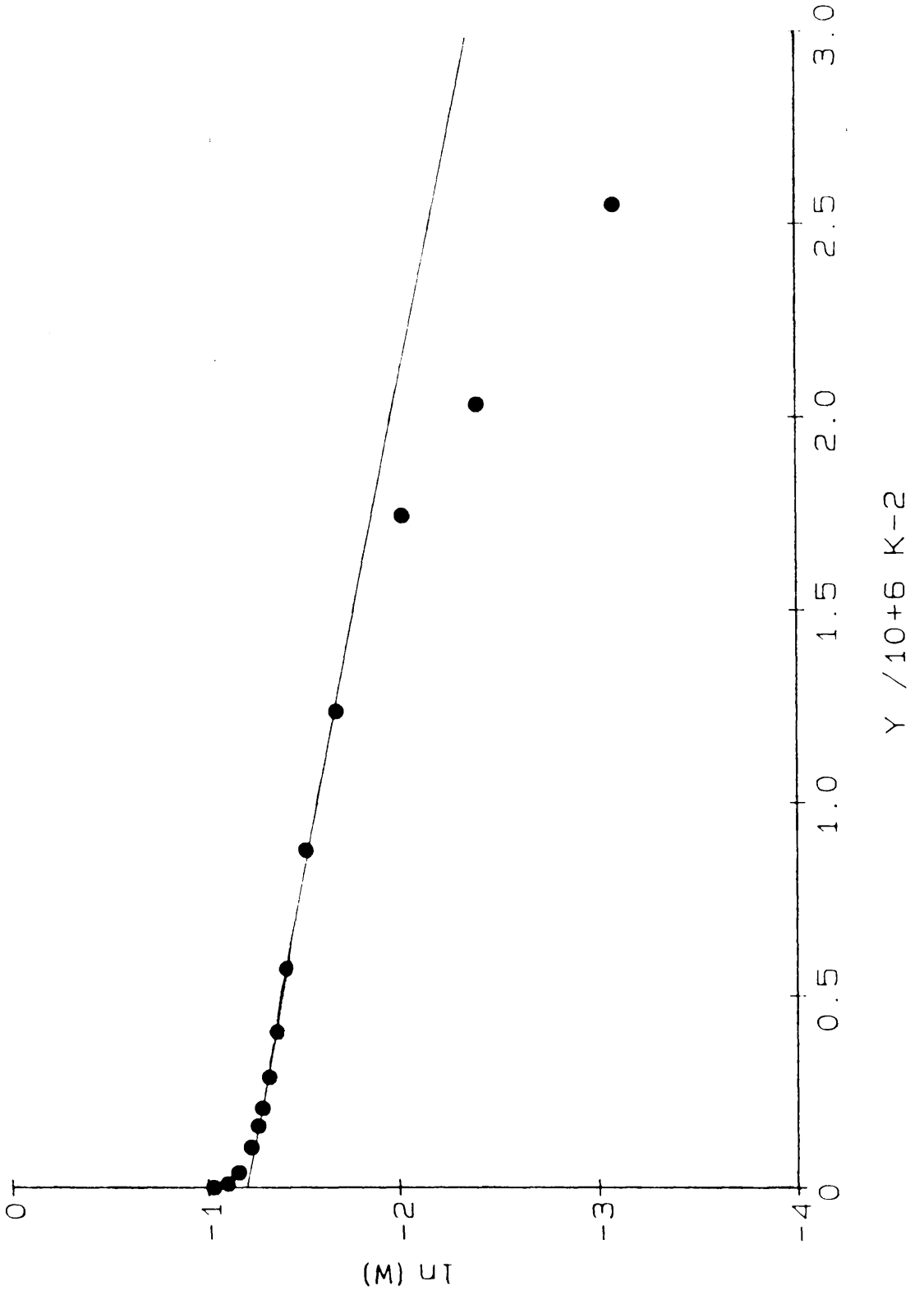

Figure 5.11

Dubinin-Radushkevich representation of C_6H_6 on CEP-31 at 293K.

gave a value of 125.5 Jg^{-1} for the calculated enthalpy resulting from immersing CEP-31 into benzene. When an immersion experiment was carried out using benzene, an experimental value of 129.0 Jg^{-1} was obtained. The closeness of these results suggests that the sample possessed a very small external surface area, especially in view of the fact that there is a ± 3 Jg^{-1} error on the experimentally determined immersion enthalpy value. The difference between the experimental and calculated immersion enthalpies is only 3.5 Jg^{-1}. If this difference in the two values is considered to be due purely to external surface area, then using the standard value of 114 mJm^{-2} of open surface (Kraehenbuehl, 1983), the external surface could be calculated to be around $30m^2g^{-1}$. This value could be neglected in any further calculations as could any value under around $40m^2g^{-1}$. Knowing that the effects of the external surface area could be neglected, the remaining immersion experiments were carried out leading to the results shown in table 5.6. In this table and all subsequent tables relating to immersion results, the values L and dL have been omitted as they were shown in table 5.3 and since the same molecular probes were used in all of the immersion experiments there was no variation in these values.

Table 5.6 Immersion results of CEP-31

Probe	ΔH_i	W(L)	dW(L)/dL
CH_2Cl_2	128.1	0.329	
			0.25
C_6H_6	129.0	0.309	
			0.29
C_6H_{12}	90.5	0.271	
			0.64
CCl_4	85.3	0.213	
			1.88
$C_{10}H_{16}$	44.8	0.119	
			-0.01
C_5Cl_6	52.6	0.120	

The negative value of dW(L)/dL has no real physical meaning but only arises from the closeness in the volume values obtained from immersion into $C_{10}H_{16}$ and C_5Cl_6. The fact that there is so little difference in these values means that errors in the immersion enthalpies, which are not normally noticed due to the greater differences generally involved, become noticeable. Effectively the value illustrates that there is no porosity in the size range 0.68 to 0.75 nm.

When this sample was studied by high resolution electron microscopy, the results displayed in table 5.7 were obtained for the percentage of pores in the various pore size ranges.

Table 5.7 Percentage of pores in different pore width ranges obtained from HREM for CEP-31.

Sample	Pore Width (x 10^{-1} nm)					
	3.01-4	4.01-5	5.01-6	6.01-7	7.01-8	8.01-9
CEP-31	11.1	16.3	26.8	41.9	2.6	1.3

Using the values presented in tables 5.6 and 5.7, histograms showing the micropore size distributions obtained using the two techniques were constructed and these can be seen in figure 5.12. This figure shows fairly good agreement for the basic trend of the distributions. Both distributions do show an increase in the quantity of porosity with increasing pore size and both show that there is very little porosity in the region above 0.7 nm.

Examination of the immersion results shows that there was still 0.12 cm^3g^{-1} of porosity accessible to C_5Cl_6, the largest of the molecular probes employed. This porosity must occur somewhere in the 0.8 to 2.0 nm range, as earlier calculations had shown there to be very little pore volume in the mesoporous range. Examination of micrographs such as plate 16 showed the presence of cavities in the thin region at the edge of the sample. These cavities were of varying size and it may be these areas that constitute the remaining quantity of porosity possessed by the sample. Unfortunately there is no way to quantitatively analyse this type of porosity from the

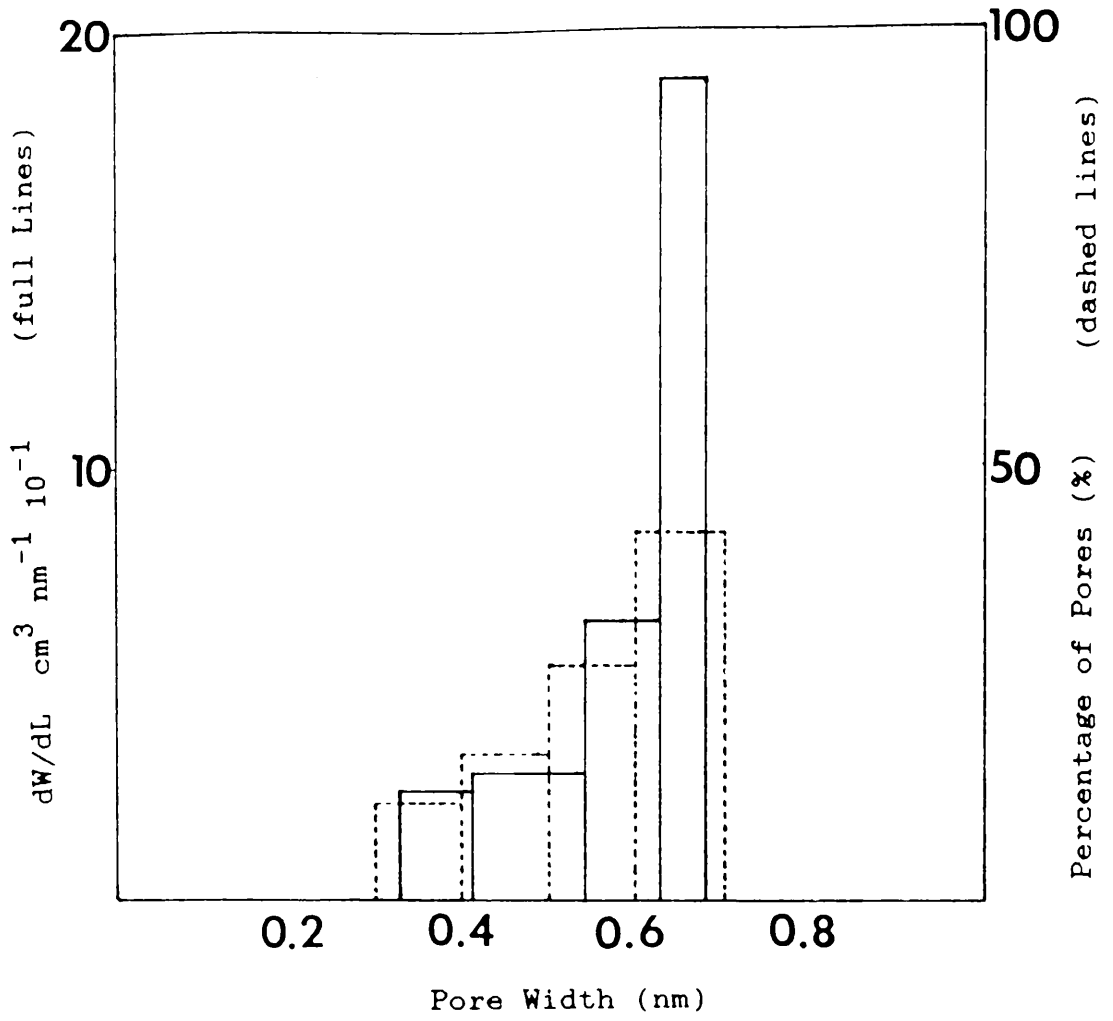

Figure 5.12

Micropore size distribution of CEP-31 obtained from immersion calorimetry and HREM (Full and dashed lines respectively).

electron micrographs alone.

Had immersion data been obtained for this size range, then the micrographs could have been examined in a manner analogous to that used in the 0.3 to 0.8 nm range and the statistics retrieved could have been fitted to those results obtained from immersion calorimetry. However no immersion data was produced for this range, therefore only a qualitative analysis of this type of porosity could be attempted. Another problem that would have arisen had the larger pore types been investigated quantitatively by electron microscopy is that the varying shapes of such pores would make the determination of their widths very difficult as a variety of values could be obtained depending on the way in which the pore was measured. In addition to this problem there is also the fact that it is difficult to image these pores extensively as increases in the sample thickness mean that detail of this pore type is obscured by overlying material. Returning to the micropore size distributions in the 0.3 to 0.8 nm size range, it is apparent that the distribution derived from microscopical measurements can be fitted well to that obtained from immersion calorimetry in the range below about 0.6 nm. However, this leaves the peak in the 0.6 to 0.7 nm range obtained from microscopy much smaller than the corresponding calorimetric result. At this point however, the reason for this difference was not apparent.

The next carbon to be studied was CEP-*35. This is a carbon of 35% burn-off, the presence of the star being to

differentiate this sample from the CEP-35 described earlier. This sample was first characterised using immersion calorimetry. In order to calculate the volume terms, a value of 30.0 $kJmol^{-1}$ was used for the characteristic energy, this being the value determined by Kraehenbuehl et al. (1986) from the characterisation of their CEP-35. The results obtained from the immersion experiments are displayed in table 5.8.

Table 5.8 Immersion results for CEP-*35

Probe	ΔH_i	W(L)	dW(L)/dL
CH_2Cl_2	139.8	0.367	
			0.40
C_6H_6	136.6	0.335	
			0.10
C_6H_{12}	105.4	0.322	
			0.28
CCl_4	116.6	0.297	
			0.94
$C_{10}H_{16}$	92.3	0.250	
			1.13
C_5Cl_6	73.3	0.171	

These values were then used to present the micropore size distribution in the form of a histogram which can be seen in figure 5.13. This diagram also contains the distribution obtained from immersion studies on the CEP-35 studied previously. Comparing these diagrams shows the micropore size distribution of the two samples to be very dissimilar. The pores of CEP-*35 are concentrated at the larger size range of the diagram. There also appears to be a double distribution with a small concentration of pores

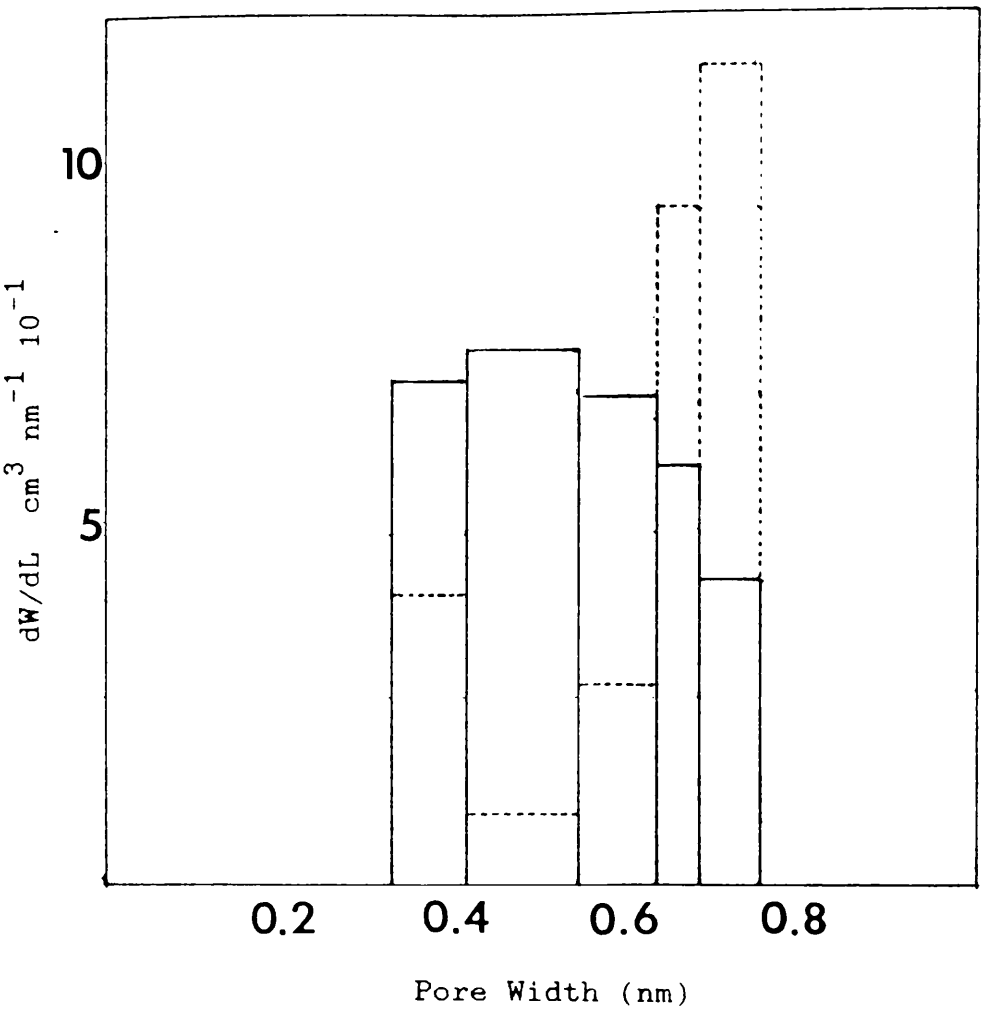

Figure 5.13

Micropore size distribution, from immersion calorimetry, of CEP-35 and CEP-*35 (full and dashed lines respectively).

in the range 0.3 to 0.4 nm. It appears that two carbons derived from the same precursor and activated in the same manner to the same degree can result in different pore size distributions. This lack of equivalence of the porous structures of the two materials meant that an adsorption isotherm of CEP-*35 had to be made in order to find the characteristic energy of the sample as the Kraehenbuehl value was unsuitable due to the difference in the distributions. Benzene was adsorbed onto the sample and the resulting isotherm (figure 5.14) was of type I in the Brunauer, Deming, Deming and Teller classification, typical of a microporous carbon. The Dubinin-Radushkevich equation was next used to construct the representation shown in figure 5.15. The representation shows some downward deviation in the region of low relative pressure. This phenomenon is characteristic of something causing the adsorbate difficulty on entering the pore network such as constrictions. The linear region of the representation resulted in a volume W_o of 0.334 cm^3g^{-1} and a characteristic energy E_o of 29.1 $kJmol^{-1}$. If these two values are used to calculate the value expected to result from immersion into benzene the value 132.2 Jg^{-1} is obtained. The experimental value, when an immersion experiment was actually carried out, was 136.6 Jg^{-1}. The experimental value is 4.4 Jg^{-1} larger than the calculated value. This difference is relatively small, implying that the sample did not posses an appreciable external surface area, therefore no correction had to be made for a mesoporous contribution in further calculations.

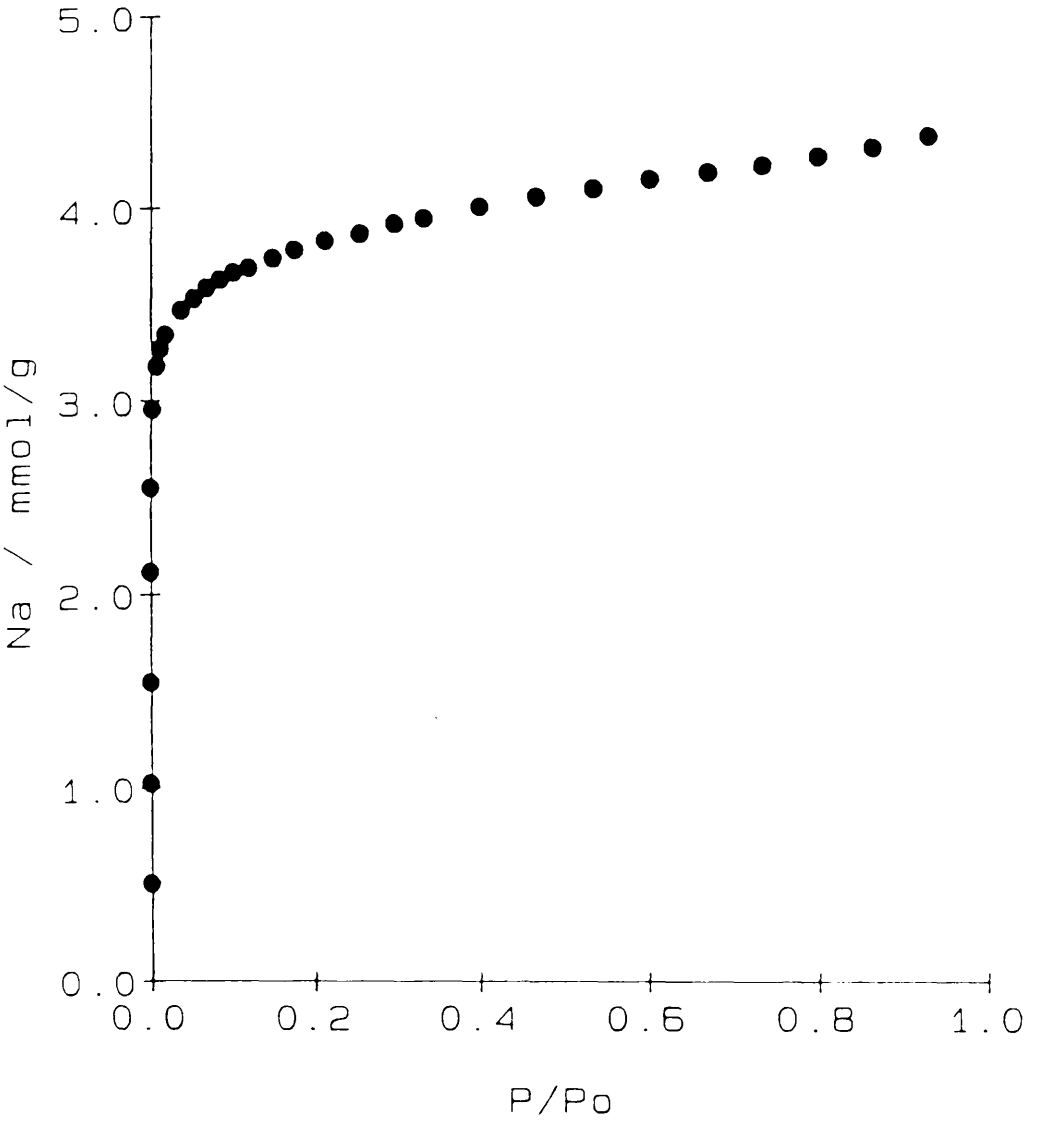

Figure 5.14

Adsorption isotherm of C_6H_6 on CEP-*35 at 293K.

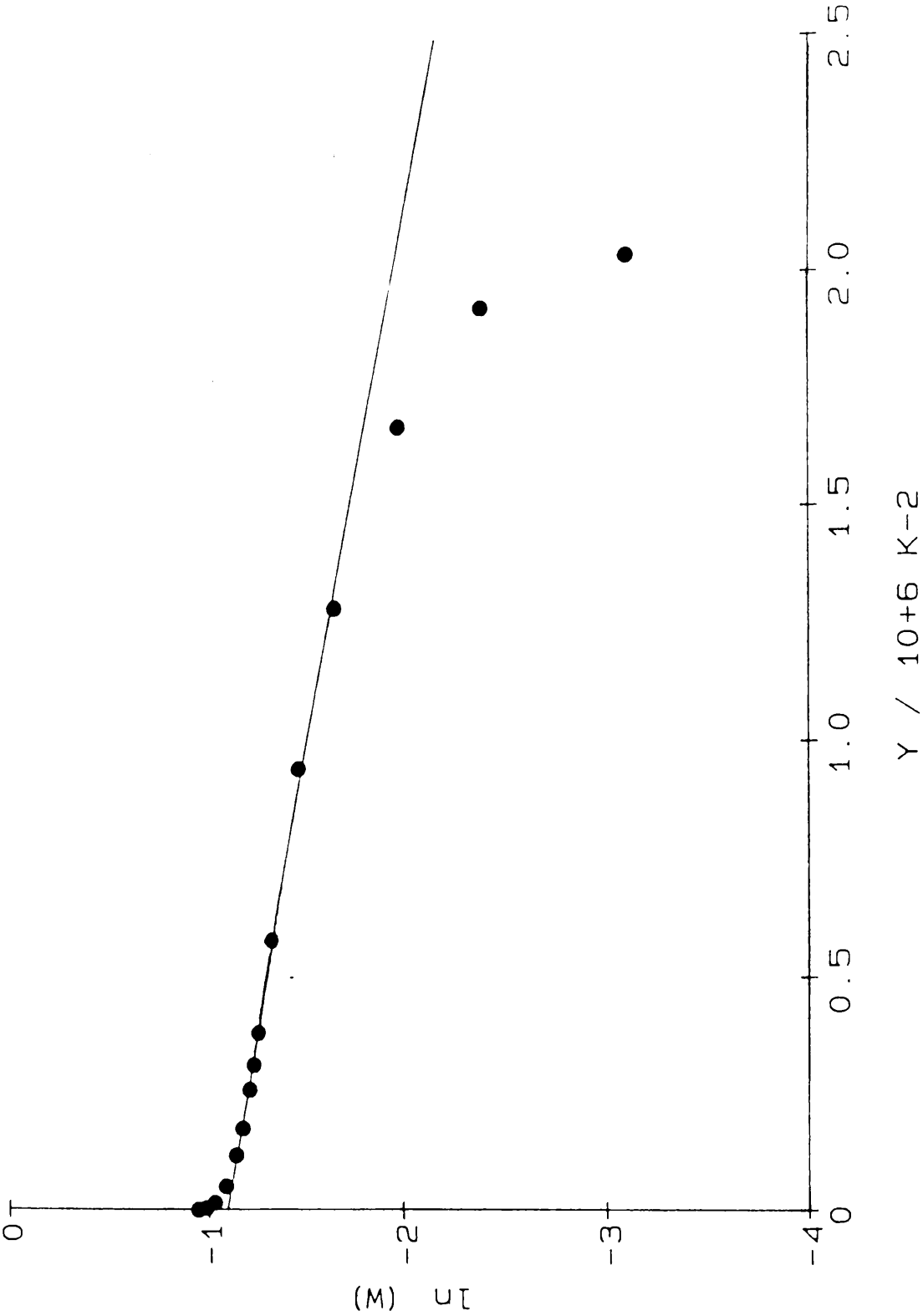

Figure 5.15

Dubinin-Radushkevich representation of C_6H_6 on CEP-*35 at 293K.

The information on the characteristic energy being known, it was then possible to recalculate the micropore size distribution from the immersion experiments into the various molecular probes. The results from these calculations are shown in table 5.9.

Table 5.9 Immersion results for CEP-*35, E_o = 29.1 $kJmol^{-1}$

Probe	ΔH_i	W(L)	dW(L)/dL
CH_2Cl_2	139.8	0.378	
			0.41
C_6H_6	136.6	0.345	
			0.10
C_6H_{12}	105.4	0.332	
			0.29
CCl_4	116.6	0.306	
			0.96
$C_{10}H_{16}$	92.3	0.258	
			1.17
C_5Cl_6	73.3	0.176	

Comparing the results in tables 5.8 and 5.9 shows there to be very little difference between them as would have been expected considering that the values for the characteristic energy for the two samples were quite similar.

When examined in the electron microscope it was discovered that this sample had a similar appearance to that of CEP-31, showing the same type of "loose" structure at thin edges (plate 17). This again may account for the 0.176 cm^3g^{-1} of porosity available to perchlorocyclopentadiene. When the pore sizes were measured from the micrographs of

this sample, the results displayed in table 5.10 were obtained.

Table 5.10 Percentage of pores in different pore width ranges obtained from HREM for CEP-*35.

Sample	Pore Width (x 10^{-1} nm)						
	2.01-3	3.01-4	4.01-5	5.01-6	6.01-7	7.01-8	8.01-9
CEP-*35	2.6	33.6	9.2	29.6	15.8	4.6	4.6

The values shown in tables 5.9 and 5.10 were used to construct the histograms showing the micropore size distribution that can be seen in figure 5.16. It is instantly apparent that the two distributions presented here do not show as good an overlap as those previously described. The microscopy results can be made to overlap those results obtained from immersion calorimetry in the lower pore sizes, below around 0.6nm. Both techniques do show a peak in the 0.3 to 0.4 nm range, then few pores from 0.4 to 0.5 nm followed by a rise in the quantity of porosity in the region 0.5 to 06 nm. However at higher values opposing behaviours are reflected. Microscopy shows the quantity of porosity to fall as the size of the pores increases, whereas the immersion results continue to rise with increasing pore size.

When the heat of immersion into perchlorocyclopentadiene is considered, it corresponds to a pore volume of

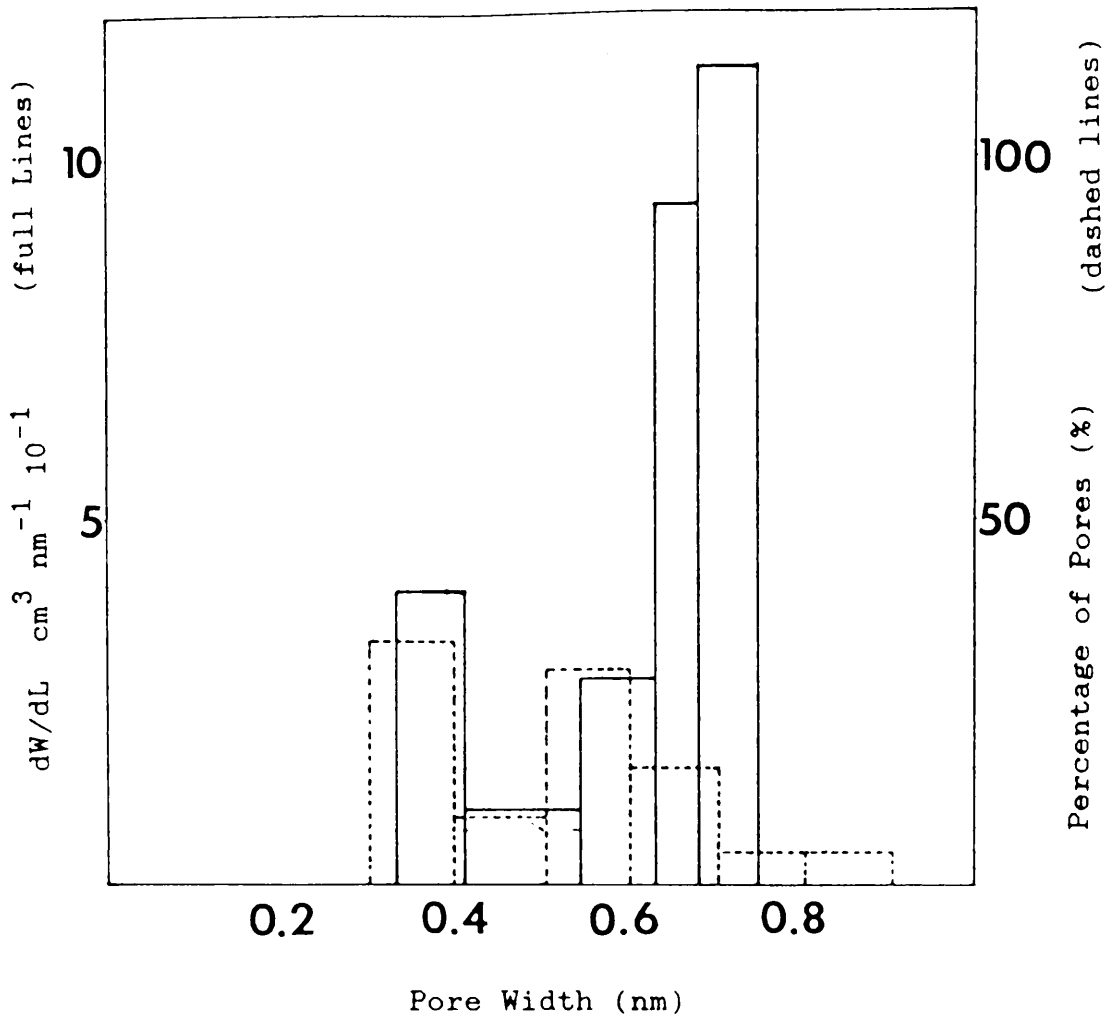

Figure 5.16

Micropore size distribution of CEP-*35 obtained from immersion calorimetry and HREM (Full and dashed lines respectively).

$0.176 cm^3 g^{-1}$. This is a considerable volume and it shows that there is still porosity in the region above 0.75 nm although from immersion calorimetry it was not possible to characterise this region. A possible explanation for this discrepancy is that used for the lack of agreement in the case of CEP-49. This explanation seems unlikely however, because in the case of CEP-*35 the two distributions are not similar with one simply shifted to a lower value than that obtained from the other, as was the case with CEP-49. It seems more likely that rather than being the product of the exfoliation of smaller pores, the pores of a size greater than 0.6 nm in the immersion results are not for some reason showing up in the conditions under which the pores were measured from the electron micrographs. This may be because in the present work only those pores observed to be exiting the sample at its edge were measured from the electron micrographs. The larger pores may be situated within the internal structure of the sample and may be of such a nature that only a small proportion of these pores can be imaged at the sample edge. If this were true it would mean that the microscopy results would not reflect the true proportion of the larger pores that are present. These pores may be like the "cavities" that can be seen in plate 17. These larger pores are accessed by smaller pores and these may possibly swell to allow the larger adsorbate molecules to enter the larger pores. Such a condition would explain the downward deviation observed on the Dubinin-Radushkevich representation. This is a different process to that suggested for CEP-49. In the case of CEP-49, it is

suggested that because of the looseness of the structure the pores exfoliate to allow the adsorption of larger adsorbate molecules within them. However, in the case of CEP-*35, this pore expansion would not simply allow adsorption of vapour within these pores themselves but more importantly it would let this vapour access the larger pores which themselves do not have to undergo exfoliation.

It is difficult to gauge quantitatively the extent of the porosity contained further from the edge of the sample because it becomes more difficult to image the structure as the specimen increases in thickness as was mentioned earlier. It could be claimed that another problem associated with the study of pores imaged within the sample is that it is not certain whether a pore is open or closed if it is surrounded by sample. This is because the nature of image formation is such that only layer planes perpendicular to the electron beam are imaged. Therefore a pore that appears to be totally enclosed in the micrograph may or may not be open either above or below the plane in which the image is situated. Even a pore that does not appear totally enclosed may not be an open pore unless it is connected to the outside of the particle via the rest of the pore network. However, when using electron microscopy certain assumptions must be made if any results at all are to be obtained. If this were not the case then even the pores seen to exit the edge of the particle could not be claimed to be open micropores. This is because many of those pores would only arise at a particle edge because

of the grinding process during sample preparation and there is no way of knowing their position before this had been carried out. When these points have been considered the difficulty that would be involved in trying to quantify the porosity other than that imaged at the sample edge becomes apparent. It seems possible that this "loose" structure observed at the sample edge occurs extensively throughout the sample interconnected by a network of smaller pores.

The explanation suggested here to explain the results obtained from CEP-*35 could also be referred back to the previous sample, CEP-31. This would explain the reason for the microscopy results not reflecting a similarly large peak to that derived from immersion calorimetry experiments for the pores larger than 0.6 nm.

5.4 Study of Sample CEP-51

The final CEP sample to be examined was CEP-51 which was characterised more comprehensively than the previous samples. An initial investigation was undertaken by adsorbing benzene onto the sample. The resulting isotherm is shown in figure 5.17. From this isotherm the Dubinin-Radshkevich representation for this sample was constructed and can be found in figure 5.18. This representation possesses quite a marked downward deviation in the lower pressure region. In case this deviation was not due to some kind of restriction on the access of the adsorbate to the micropore system but instead due to a lack of

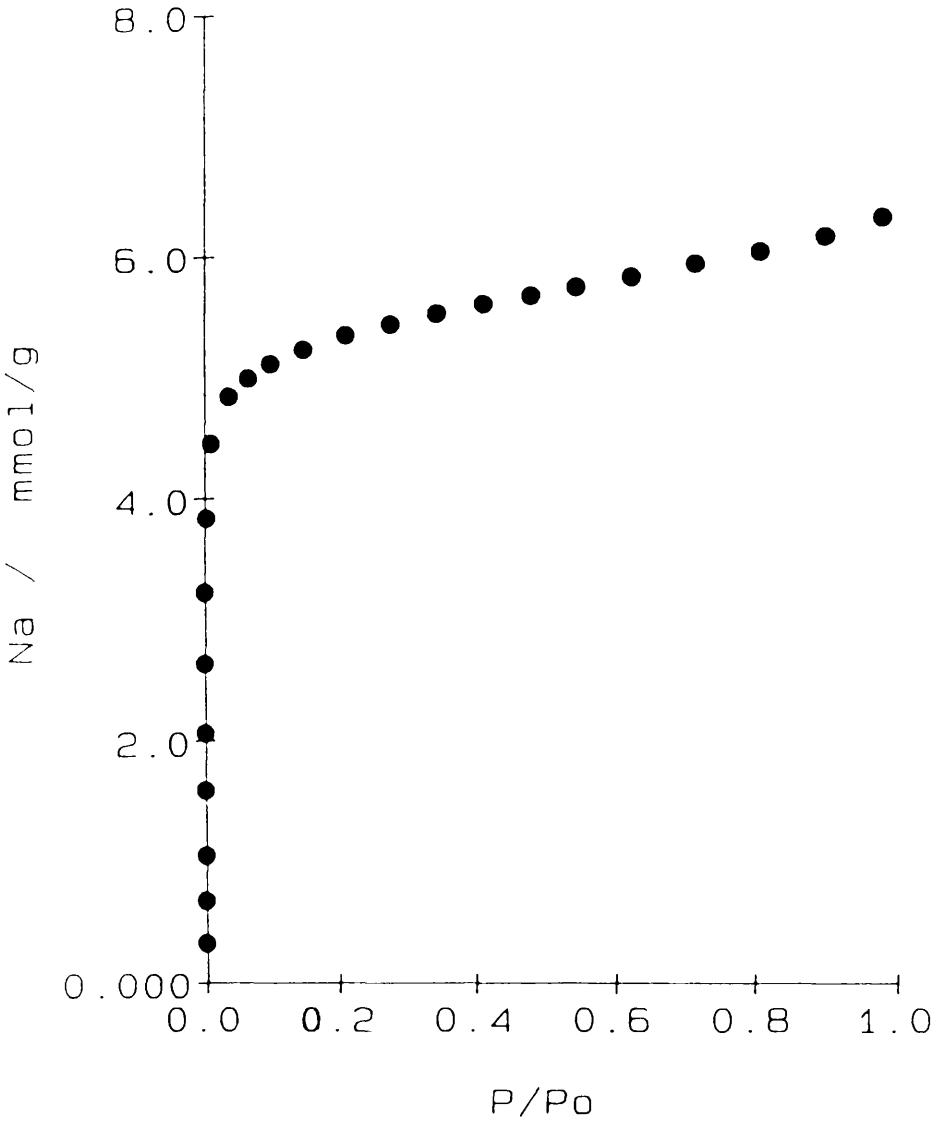

Figure 5.17

Adsorption isotherm of C_6H_6 on CEP-51 at 293K.

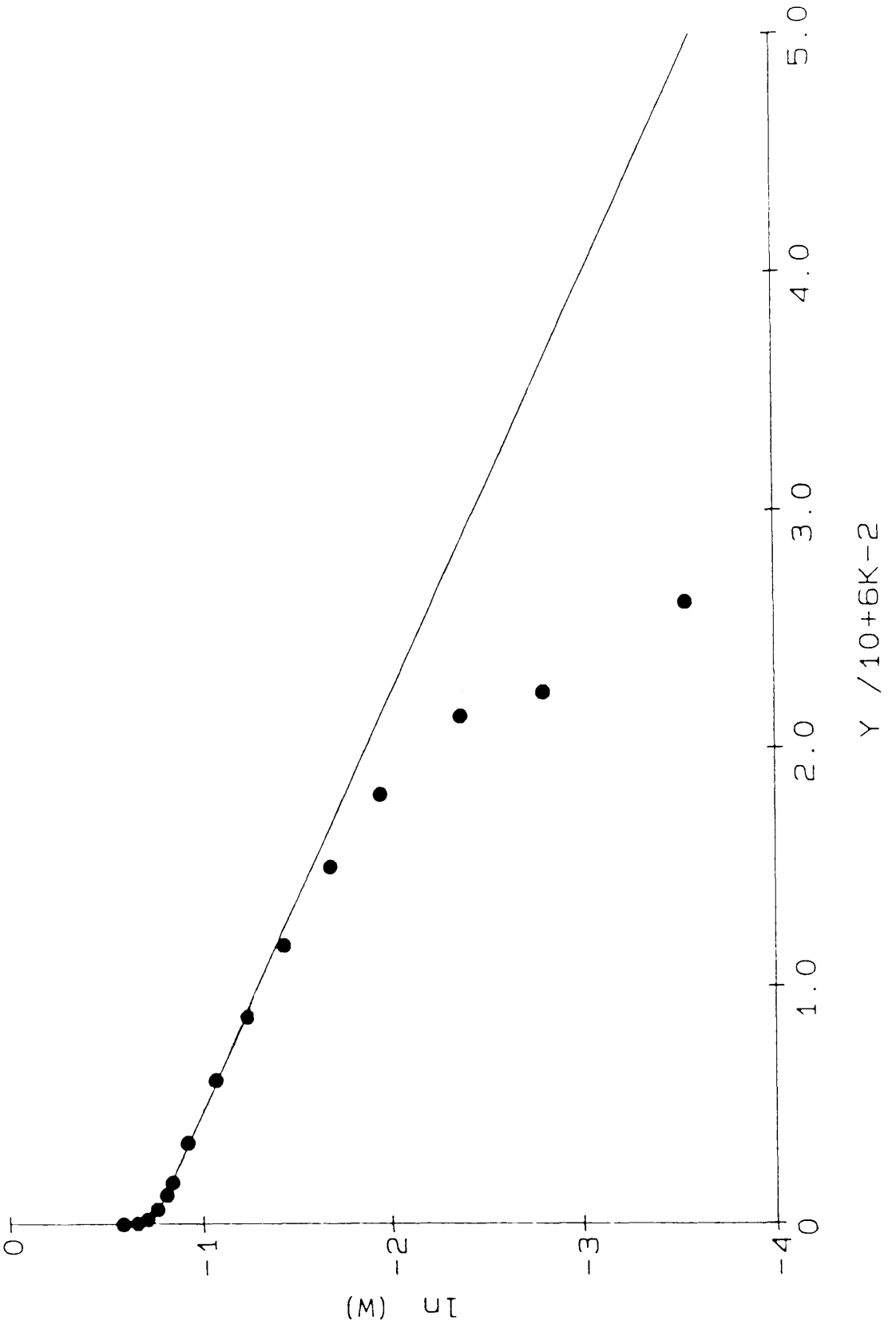

Figure 5.18

Dubinin-Radushkevich representation of C_6H_6 on CEP-51 at 293K.

applicability of the Dubinin-Radushkevich equation because the sample possessed a value of n other than 2, a determination of the value of n was undertaken.

Using the isotherm (figure 5.17), an estimate of the limiting quantity of vapour adsorbed was made resulting in a value of 5.35×10^{-3} $molg^{-1}$. Multiplication of this value by the molar volume of benzene, 88.91 cm^3mol^{-1}, led to a value of $0.476cm^3$ for the volume of the micropores W_o, accessible to benzene. As mentioned earlier it is possible to calculate the value of n using the equation:

$$\ln\ln(W_o/W) = n\ln(A) - n\ln(E) = n\ln(RT\ln p_o/p) - n\ln(E)$$

The quantities $\ln\ln(W_o/W)$ and $\ln(A)$ were calculated for some of the points from the CEP-51 isotherm. When presented graphically, these values resulted in the representation displayed in figure 5.19. The gradient of this line corresponds to n and was found to have a value of 2. This value of n means that the Dubinin-Radushkevich equation is indeed the applicable representation to be used for this sample rather than the Dubinin-Astakhov equation with a value of n other than 2. The linear region of the Dubinin-Radushkevich representation produced values of W_o equal to 0.478 cm^3g^{-1} and E_o equal to 25.36 $kJmol^{-1}$. The value of W_o is in extremely good agreement with that estimated from the adsorption isotherm. Knowing the values of W_o and E_o the theoretical immersion enthalpy was calculated using:

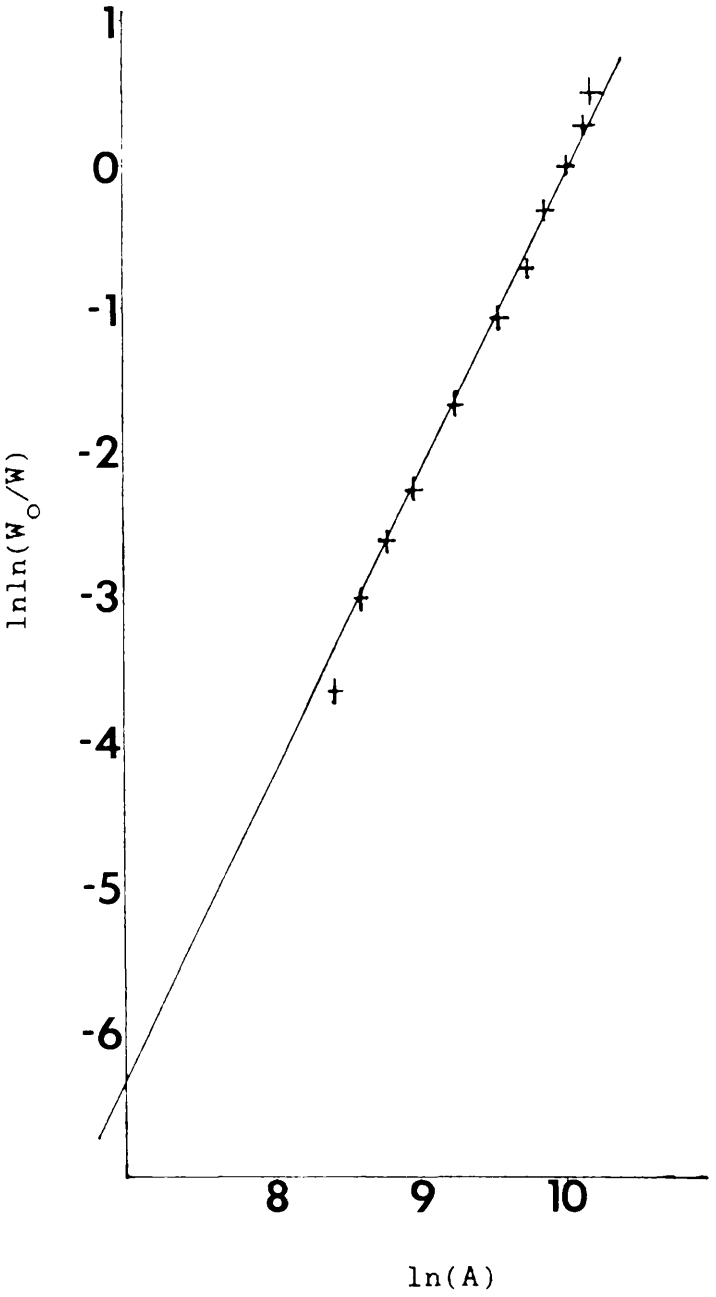

Figure 5.19

Evaluation of parameter n for CEP-51.

$$\Delta H_i = \beta E_o W_o (1+\alpha T)\sqrt{\pi}/2V_m$$

This equation yielded a value of $164.8 Jg^{-1}$, a result in excellent agreement with the value $164.6\ Jg^{-1}$ that was actually found when an immersion experiment was carried out using benzene. This result indicates that this sample does not possess an appreciable external surface area. Further evidence for the lack of an external surface area was produced when calculations were carried out by decomposing the isotherm into its internal and external contributions. These calculations pointed to an external surface area of around 20 to 30 m^2g^{-1}. The desorption cycle of the isotherm, shown in figure 5.20, when analysed, suggested a mesoporous contribution of around 30 to 40 m^2g^{-1}. The conclusion that can be drawn from these results is that the external surface area of CEP-51 is sufficiently small that it can be neglected in any further calculations.

Having established these conditions, calorimetric experiments were carried out using the remainder of the molecular probes which produced the results displayed in table 5.11.

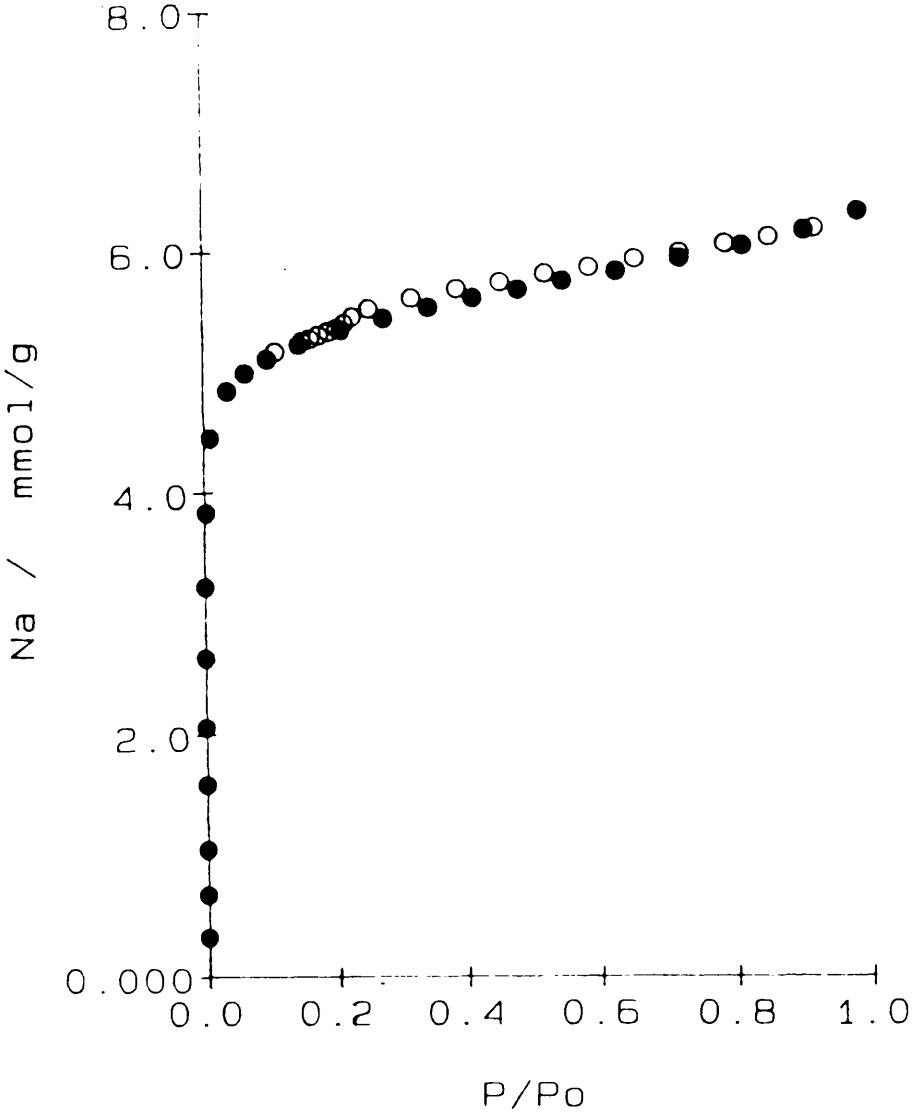

Figure 5.20

Isotherm of C_6H_6 on CEP-51 at 293K showing adsorption and desorption cycles (full and open circles respectively).

Table 5.11 Immersion results for CEP-51

Probe	ΔH_i	W(L)	dW(L)/dL
CH_2Cl_2	171.9	0.534	
			0.71
C_6H_6	164.6	0.477	
			0.02
C_6H_{12}	131.3	0.475	
			-0.04
CCl_4	158.9	0.478	
			0.00
$C_{10}H_{16}$	148.2	0.478	
			0.68
C_5Cl_6	160.2	0.442	

The micropore size distribution that resulted from these immersion results is shown in figure 5.21. The negative value of dW(L)/dL has been omitted from this diagram as it has no meaning. It probably arose because C_6H_6, C_6H_{12}, CCl_4 and $C_{10}H_{16}$ all have access to approximately the same pore volume, making small errors in the measured immersion enthalpies more obvious.

Care must be taken in the interpretation of the micropore size distribution shown here. Although it appears that there is a double distribution of micropores, one centred around 0.37 nm and the other centred at 0.72 nm, if must be remembered that the largest molecular probe employed, perchlorocyclopentadiene, with a width of 0.75 nm, still had access to a pore volume of 0.4418 cm^3g^{-1}. This is a considerable volume and is in fact greater than the total pore volume possessed by many active carbons. This implies that either the peak at 0.68 to 0.75 nm is the beginning

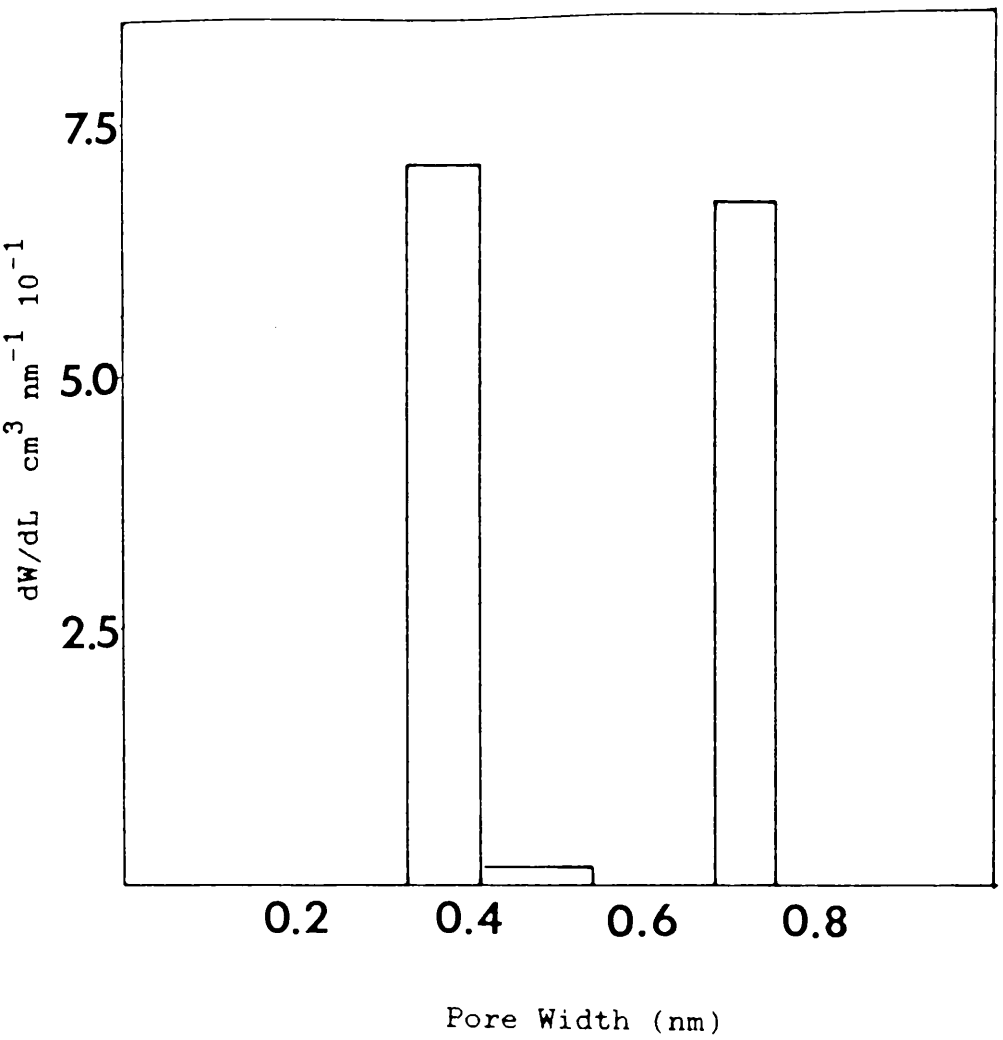

Figure 5.21

Micropore size distribution of CEP-51 from immersion calorimetry.

of a broader distribution of pores or else there are further separate distributions of pores somewhere in the 0.75 to 2.0 nm range. It is not possible to make any greater detailed comments on this area of porosity as that size range was not examined using immersion calorimetry.

To further investigate the adsorptive properties of sample CEP-51, an isotherm was undertaken using a larger molecule, carbon tetrachloride. The resulting Dubinin-Radushkevich representation is shown in figure 5.22. As in the case of benzene being adsorbed onto the sample, the representation shows a strong downward curvatures in the region of low relative pressure. This deviation from the linear region is more marked in the case of the carbon tetrachloride plot. This is as would be expected if the deviation does in fact arise from some constriction in the microporous structure because a carbon tetrachloride molecule being larger than a benzene molecule, would experience greater difficulty in passing a constriction. The Dubinin-Radushkevich equation yields a value of 25.52 $kJmol^{-1}$ for the characteristic energy of CEP-51 for the case of carbon tetrachloride. This value is in relatively good agreement with the value 25.36 $kJmol^{-1}$ obtained when benzene was employed. These values should not differ as the characteristic energy E_o is a function of the adsorbent and should therefore be independent of the adsorbate used, provided an adsorbate is not excluded from part of the microporous structure. The representation also produced a value for W_o of $0.449cm^3g^{-1}$. This is smaller than the value of 0.478 cm^3g^{-1} that was obtained from

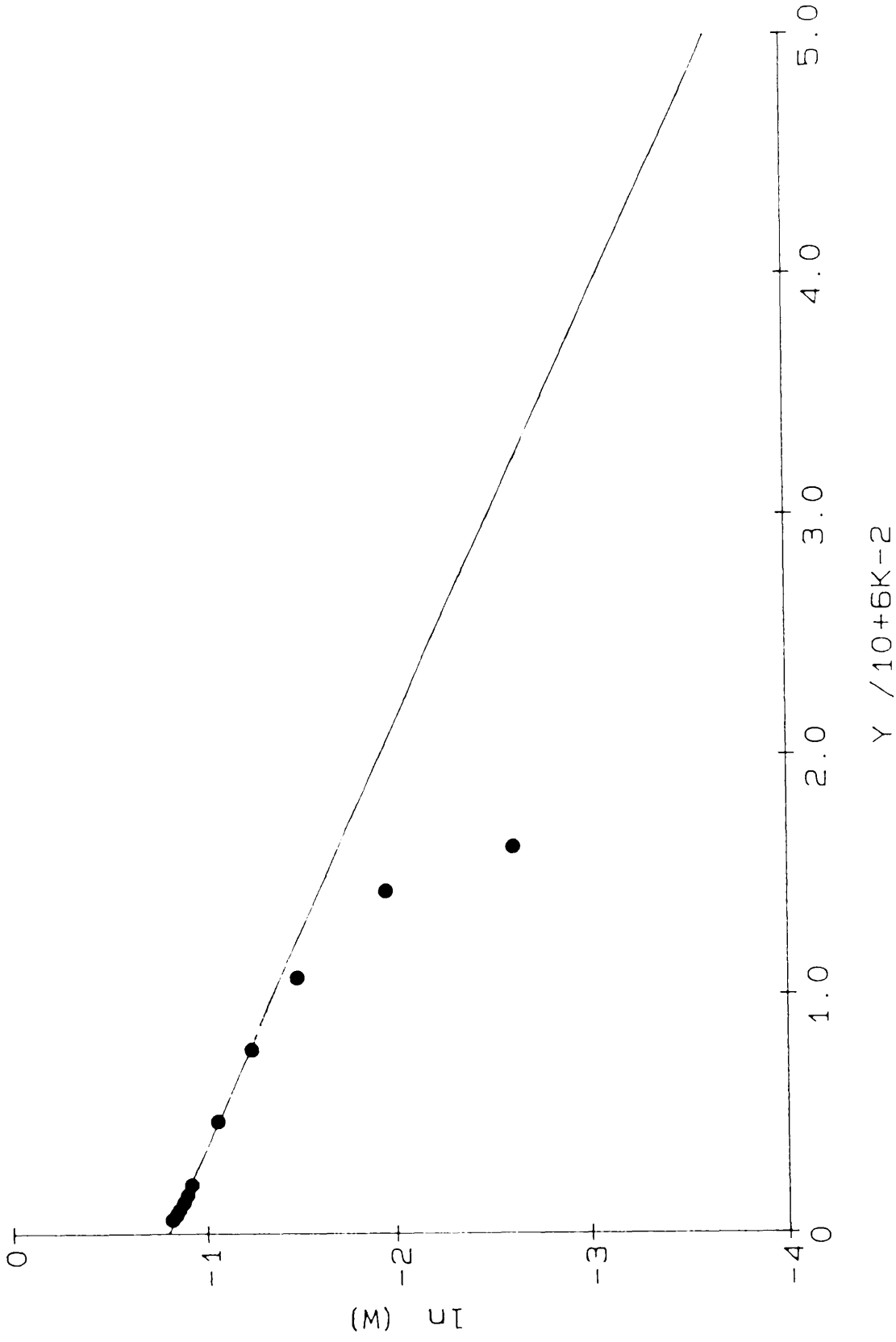

Figure 5.22

Dubinin-Radushkevich representation of CCl_4 on CEP-51 at 293K.

immersion calorimetry using carbon tetrachloride. Perhaps this is because at the lower pressures involved in the adsorption experiments and the longer times necessary to reach equilibrium as opposed to the calorimetric ones, the carbon tetrachloride molecules could not totally overcome the barrier presented by the constrictions within the time in which the experiment was undertaken.

In view of the micropore size distribution obtained using immersion calorimetry, it was considered appropriate to carry out an adsorption experiment using methylene chloride as the adsorbate. This was because the first peak in the calorimetric distribution was due purely to methylene chloride as these pores were too small to accommodate benzene or carbon tetrachloride molecules and it was thought that a Dubinin-Radushkevich representation using methylene chloride should reflect this double distribution. The adsorption isotherm resulting from the methylene chloride adsorption is shown in figure 5.23. When the values from this experiment were used to construct the Dubinin-Radushkevich representation, the plot displayed in figure 5.24 was obtained. This representation does not display as strong a downward deviation as those produced by benzene and carbon tetrachloride. This is more clearly visible in figure 5.25, which shows all three representations plotted together. Again this was the expected effect because methylene chloride, being the smallest of the molecules, should experience the least problem in accessing the pores. The methylene chloride representation is not normal

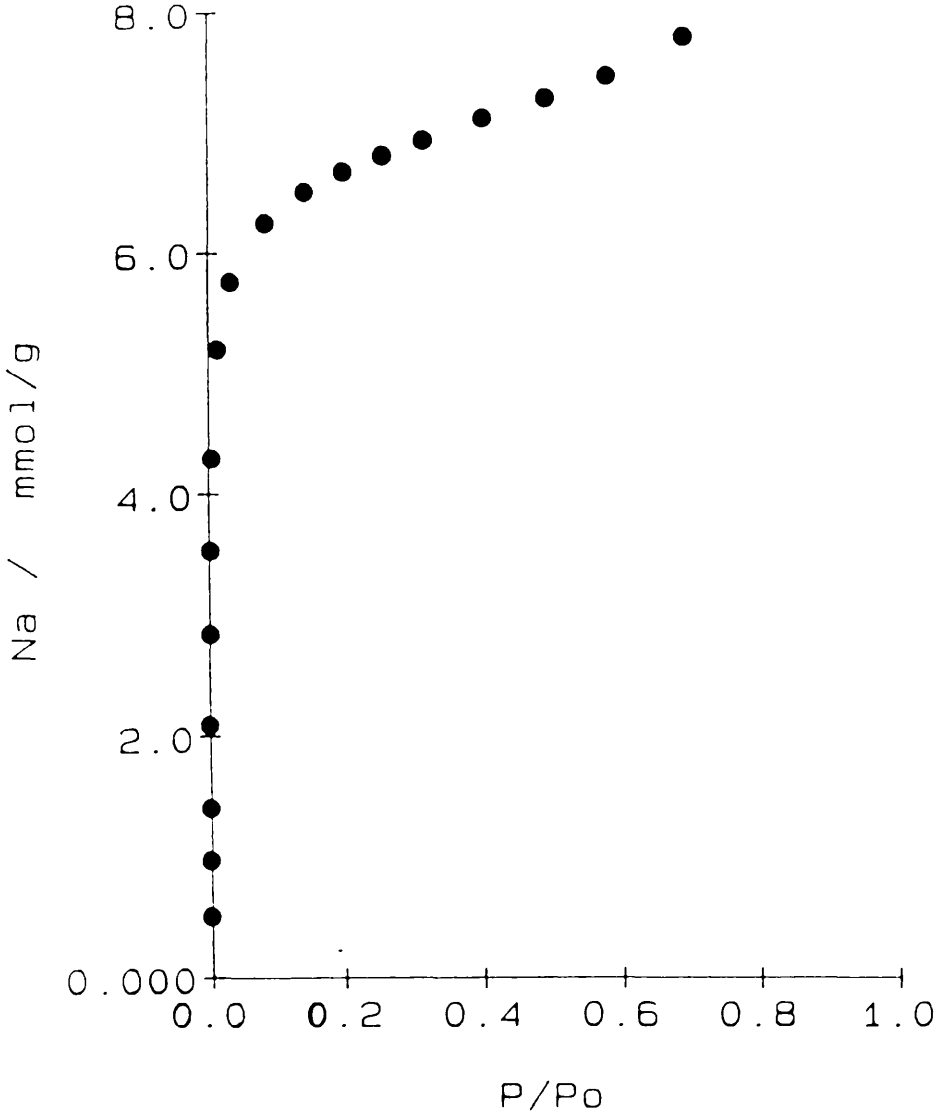

Figure 5.23

Adsorption isotherm of CH_2Cl_2 on CEP-51 at 293K.

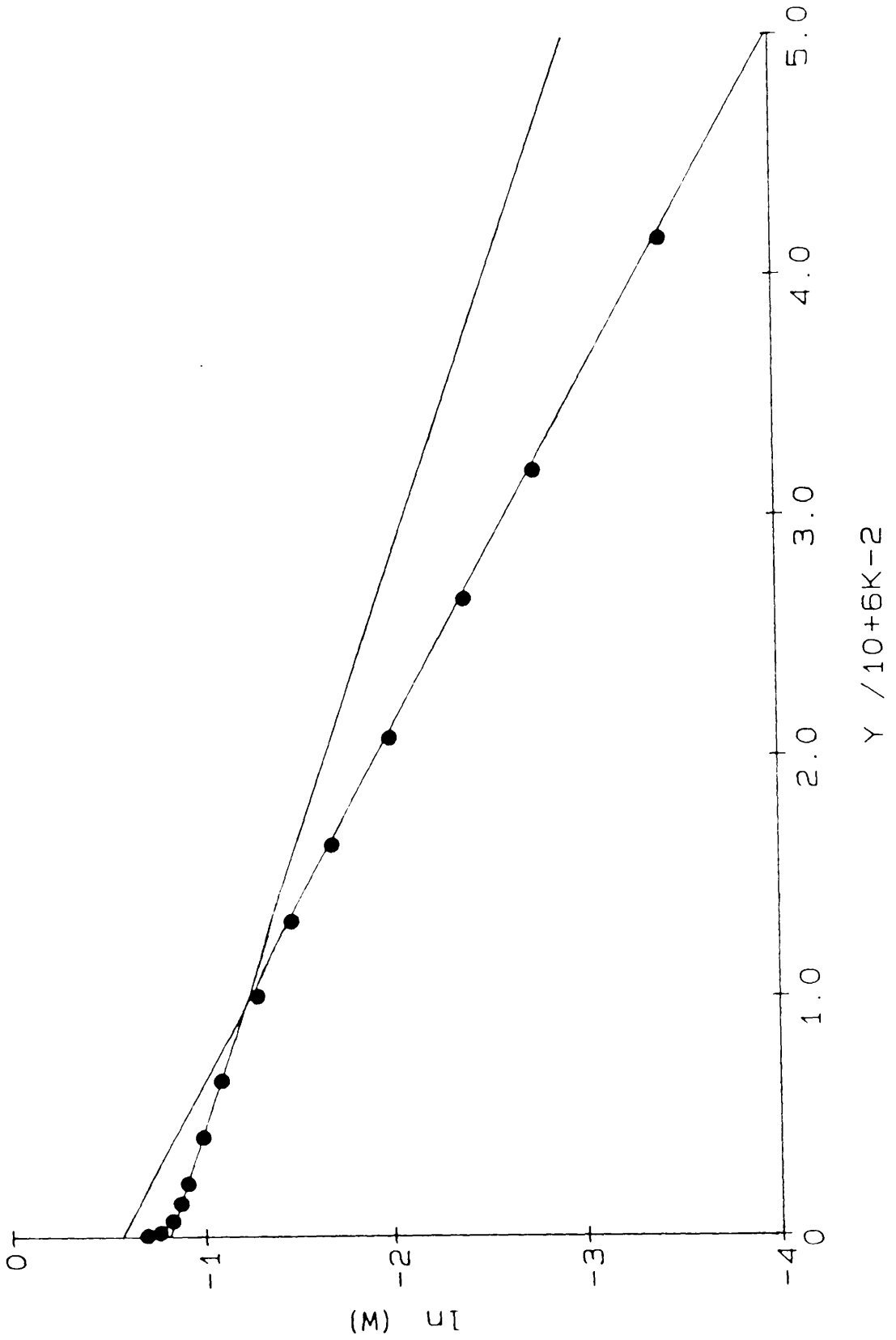

Figure 5.24

Dubinin-Radushkevich representation of CH_2Cl_2 on CEP-51 at 293K.

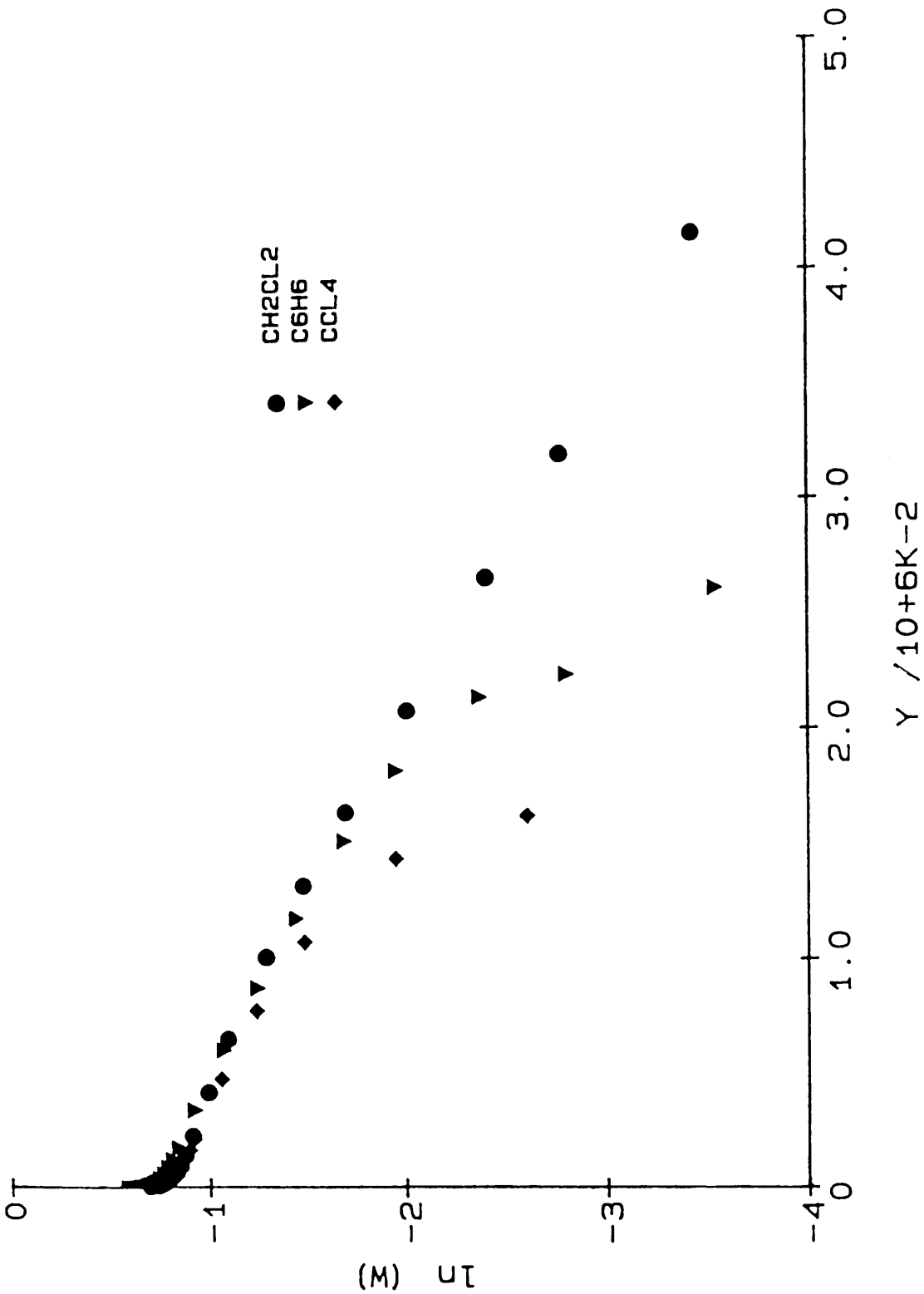

Figure 5.25

Dubinin-Radushkevich representation of C_6H_6, CCl_4 and CH_2Cl_2 on CEP-51 at 293K.

in appearance. Rather than a linear region at higher relative pressure with greater and greater deviation from linearity at lower relative pressure, there are two distinct linear regions. The linear section at low relative pressure displays a value of E_o of 23.16 $kJmol^{-1}$. The section in the higher relative pressure range results in the value 29.26 $kJmol^{-1}$. Neither of these E_o values agree with the results obtained using the previous two adsorbates. Another feature of this representation is the value of W_o that is obtained. Using the linear section in the higher relative pressure region, a value of 0.442 cm^3g^{-1} is obtained for the volume of the micropores. This volume is far lower than expected, almost 0.1cm^3g^{-1} lower than the value 0.534 cm^3g^{-1} obtained from immersion calorimetry. In fact the volume obtained from the methylene chloride isotherm is equivalent to that obtained from the adsorption experiment using carbon tetrachloride. The reason for the two linear regions is unclear, although the linear region at lower relative pressure is possibly just the usual deviation due to constrictions which for some reason does not display a strong curvature. The two linear regions do not however represent a double distribution of micropores. The usual type of representation encountered in the circumstance of a double distribution of micropores is a Dubinin-Radushkevich plot with the lesser slope in the low relative pressure region with a greater gradient in the region of high relative pressure as shown in figure 5.26. This is because, in accordance with Dubinin's theory on the volume filling of micropores, the smaller pores should be filled before the

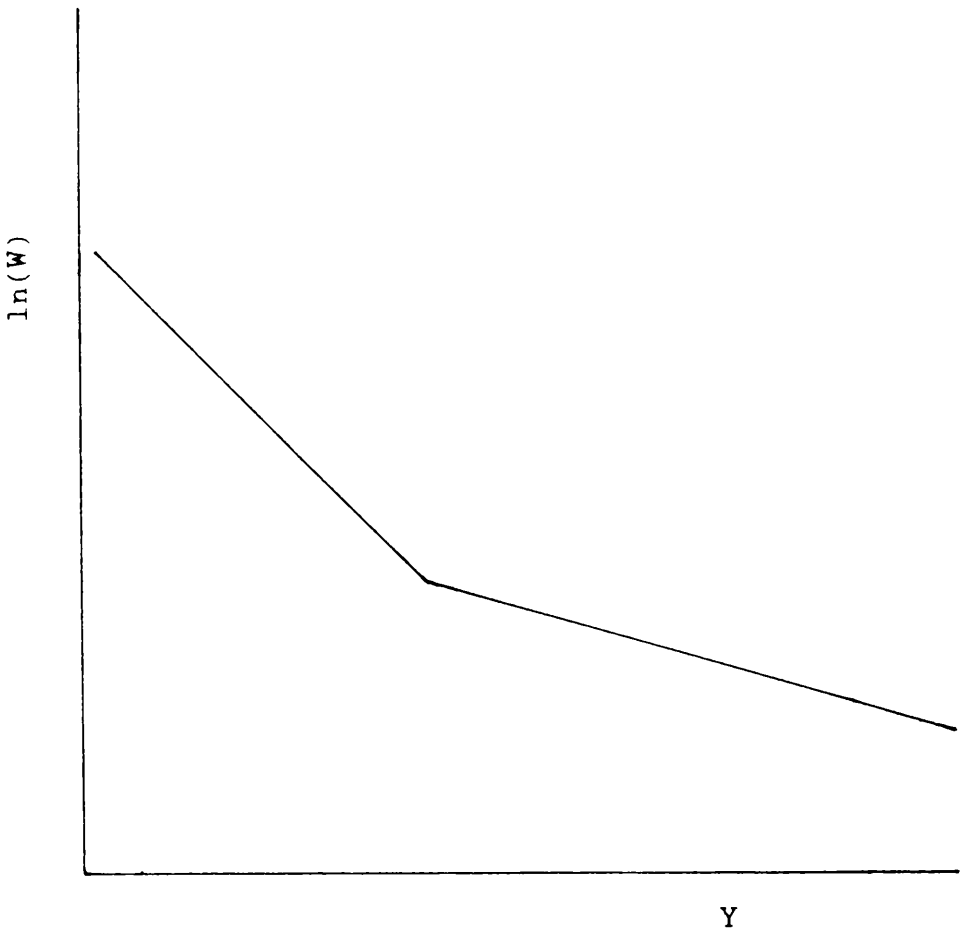

Figure 5.26

General appearance of Dubinin-Radushkevich representation for a sample containing a double distribution of micropores.

larger pores and the smaller pores result in a higher value of E_o and hence a less steep slope. In the methylene chloride representation the opposite situation was encountered. Before any further discussion on these results could ensue, it was considered necessary to examine CEP-51 by means of high resolution electron microscopy.

The sample possessed a similar general appearance to all the other CEP specimens studied in this work. When the pores exiting at the edge of the sample were measured, the results displayed in table 5.12 were obtained.

Table 5.12 Percentage of pores in different pore width ranges obtained from HREM for CEP-51.

Sample	Pore Widths (x 10^{-1} nm)					
	3.01-4	4.01-5	5.01-6	6.01-7	7.01-8	8.01-9
CEP-51	45.1	48.3	1.1	2.2	1.1	2.2

These results can be seen in figure 5.27, displayed on the same diagram as the immersion data. It is obvious that both techniques do show a peak in the low micropore size range, however that obtained by microscopy extends up to 0.5 nm whereas that gained from immersion studies only extends to 0.41 nm. The peak in the 0.69 to 0.75 nm range does not appear on the microscopy distribution. Further examination of of the micrographs showed the "cavities"

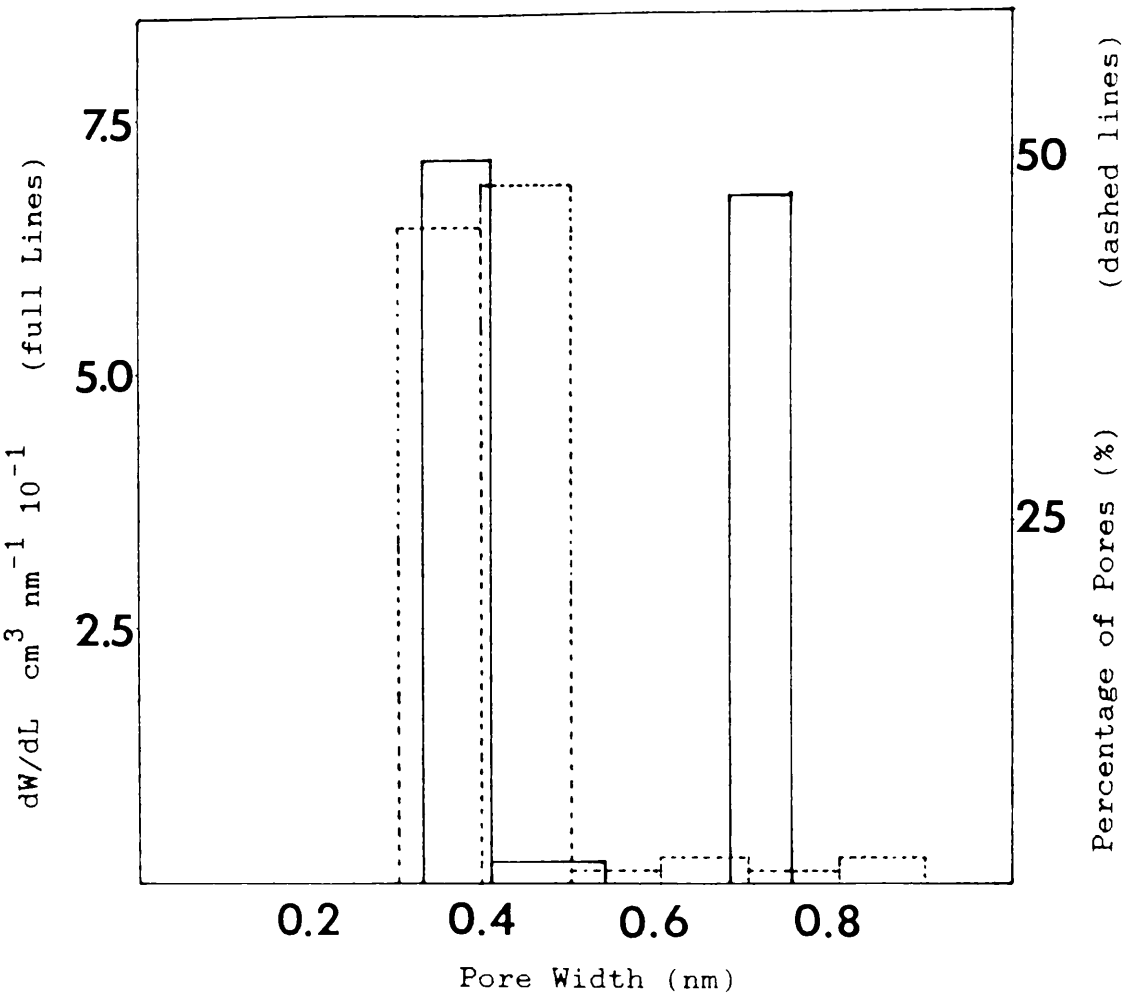

Figure 5.27

Micropore size distribution of CEP-51 obtained from immersion calorimetry and HREM (Full and dashed lines respectively).

illustrated in plate 18 to be a very common feature. These cavities are of a larger size than the pores measured exiting the sample, however, as mentioned earlier for the cases of CEP-31 and CEP-*35, it was not possible to quantify this porosity. When an entry point is apparent, these larger pores are accessed by smaller pores. However, as all the pores exiting the sample appear to be of a very small size, yet the pore volume of this sample is considerable, it would appear that these smaller pores may expand to allow access to the larger pores by an adsorbate molecule. This would explain the downward deviations observed in the Dubinin-Radushkevich representations. It would also explain why in the micropore size distribution obtained by electron microscopy, no second distribution in the larger size range was observed as this would be the part of the porous structure that was not measured from the micrographs. On the matter of the smaller sized pores, although both techniques do show a peak, that obtained from electron microscopy would indicate that a benzene molecule could be accommodated within the pores, whereas according to the calorimetric evidence this does not happen. It is possible that the pores measured in the 0.3 to 0.5 nm range using electron microscopy actually possess very little volume in themselves but merely connect a network of larger pores within the sample - although such an extensive structure cannot be imaged because as the specimen thickness increases it becomes more difficult to resolve the pore structure. This would mean that in the case of immersion calorimetry, adsorption in these pores would not show a considerable volume and the pores

available to methylene chloride discovered from the calorimetric values are actually pores of a different nature. As the Dubinin-Radushkevich representation for methylene chloride does not show the presence of a small sized pore distribution at low relative pressure, it would appear that something is restricting access to these pores. These pores are possibly extremely small pores that can exfoliate to allow methylene chloride molecules to enter them. Some micrographs such as that shown in plate 19 do show lattice fringes which open out at their ends. Perhaps methylene chloride molecules can enter these areas and even spread the planes further apart. As to this type of porosity, only speculative conclusions can be reached, because of the vacuum involved within the microscope, obviously no extensive evidence for exfoliation can be obtained. One factor not explained by the porous structure suggested here is why both the methylene chloride and carbon tetrachloride Dubinin-Radushkevich representations, yield such low values for the volume of the micropores compared with the immersion results whereas when benzene is used as an adsorbate, both techniques give the same result.

The low value in relation to carbon tetrachloride may be explained by its size and the corresponding difficulty presented to it in passing through the smaller pores. Methylene chloride however, using this explanation, would be expected to have the greatest access to the pore system. Even if it is prevented, for some reason, from accessing the pores smaller than 0.41 nm, it would still

be expected that it would have access to at least the same volume of porosity as benzene. It is also unclear as to whether the fact that the values of the pore volume accessible to methylene chloride and carbon tetrachloride obtained from adsorption experiments and that accessible to perchlorocyclopentadiene from immersion studies are all approximately 0.44 cm^3g^{-1} is of any real significance or if it is just a chance occurrence.

5.5 Validity of the Everett and Powl Model

Examination of all the micropore size distributions obtained by both the techniques of immersion calorimetry and high resolution electron microscopy, show the two methods to be in good agreement for many of the carbons studied in the present work. The main deviations between the results occur in the measurement of pores above around 0.6 nm in size or in the studies of carbons of highest burn-off. The excellent coincidence of the peaks of the distributions for carbons CEP-0 and CEP-17 must surely validate the Everett and Powl model for the reduced interaction radius of an adsorbate molecule and the assumption of the value 0.2nm selected to be subtracted from the microscopy results in the present work. The fact that the value 0.2nm seems to be appropriate rather than the value 0.23nm determined from using the 10:4 potential in theoretical calculations shows that although the theory is correct in predicting a reduction in the interaction radius, the exact value obtained from theory may not be correct. The fact that the value 0.2nm did appear to be

applicable may possibly be an indication that the theoretical description of these carbons should lie somewhere between the 10:4 and 9:3 potentials although nearer to the 10:4 potential. The discrepancy may also be due to the situations unaccounted for in the theory that were mentioned earlier or else because Everett and Powl conducted experiments using noble gases. Perhaps the larger molecules employed in this work are more easily and to a greater extent, compressed and distorted by the adsorption forces. However, on the basis of the work conducted here it is not possible to give a definite reason for this discrepancy.

The fact that the value 0.2nm was applicable may also be simply a product of the means of presentation. The use of the value 0.23nm in place of 0.2nm would not necessarily simply displace the histograms 0.03nm to a lower value. The effect of this change in value would be dependent on the choice of pore size ranges that was made. If 0.23nm was subtracted from all the measured pore widths but the same pore size ranges were employed (i.e. 0.301-0.4, 0.401-0.5 etc.) the effect would be to change the extremities of the bands, removing pores from the lower side of each size range and shifting them to the higher side of the next lowest band. It was thought unnecessary to carry out this recalculation because any agreement still remaining would not prove anything as it is not possible to obtain an exact value for the reduced interaction radius using the techniques employed here. This is purely due to the fact that with both of the

methods, pores with widths occurring in specific bands are obtained rather than a continuous distribution over all of the widths. With an extremely large sample of micropores and a more accurate measuring technique it would be possible to obtain a continuous distribution using electron microscopy. However, the bands in the histograms obtained from immersion calorimetry will always be limited by the size of the molecular probes that are available. This would mean that any developments in microscopical techniques would not further the search for the exact value of the reduced interaction radius, if indeed this is a specific quantity, because the results obtained would still be limited by the broadness of the bands in the immersion calorimetry distribution.

Although an exact value cannot be obtained, the results presented here for CEP-0 and CEP-17 and also the agreement found in the region below around 0.6nm for CEP-18, CEP-31, CEP-35 and CEP-*35 do indeed provide evidence that the interaction distance between an adsorbate molecule and the carbon atoms constituting the walls of a micropore is indeed reduced and this reduction is approximately 0.2nm, a value that appears to be applicable for a number of carbons and adsorbates. Had the Everett and Powl treatment not been applicable then no agreement would have been observed for any of these samples. For carbons of higher burn-off the agreement between the techniques is not good, although this can be explained, as suggested earlier, by the variation in the behaviour of such structures under the differing conditions of pressure

to which the samples are subjected with each of the methods of examination.

5.6 Presence of Two Types of Porosity

The results obtained from use of the two techniques seems to indicate that there are two distinct types of porosity present in some of these carbons, slit-pores in the region below around 0.6 nm and larger pores of variable shape in the region above 0.6 nm. This boundary value of 0.6 nm, is the value that was selected by Dubinin (1975) to differentiate between ultra-microporosity and super-microporosity. A more detailed discussion of these larger pores will be given in a later section.

These larger pore types do not appear in the electron microscopical micropore size distributions because they were not found at the sample edge when the pore sizes were being measured. Perhaps the reason for this is as follows: When the sample is finely ground for viewing within the microscope, the smaller sized pores because they are slit pores and can have considerable length, may be cleaved at some point along their length thus leaving the presence of such porosity at the particle edge. The larger pores however, do not appear to be long slits but in fact seem to be voids of a more cylindrical shape. Such pores if cleaved, may simply result in an indentation at the edge of the sample which if observed on a micrograph could not be identified with any certainty as the remnants of a pore. Such a process is displayed schematically in figure

5.28.

Figure 5.28 Schematic diagram of pore cleavage.

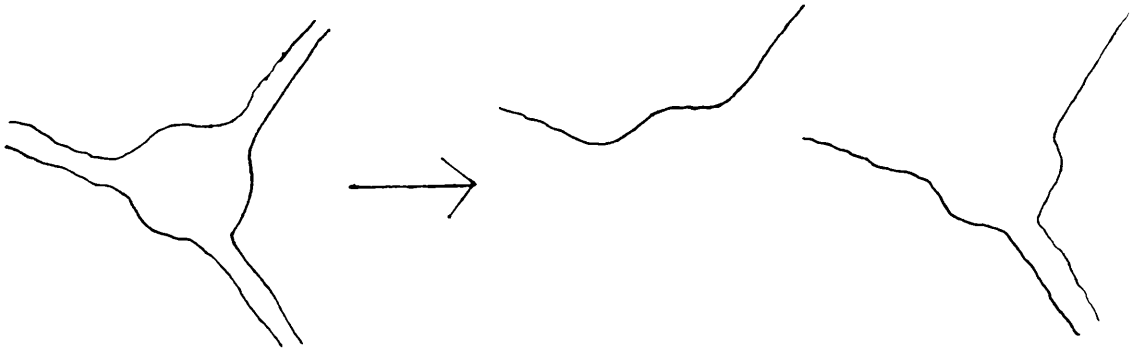

This diagram shows that for such a case, the areas resulting at the sample edge would simply be masked by the "bumpy" appearance of the specimen edge that is generally present. The pores that would actually be measured in such a case would be the smaller slit-pores that previously accessed the larger voids but now exit the particle edge.

The use of these two methods of study in conjunction makes a very powerful technique for the examination of carbons. When they result in a similar distribution this would seem to indicate that both techniques do show a true representation of the microporous structure of the sample. The variations between the experiments are also of great importance however, in deducing structural features of the sample such as the ability of the pores to exfoliate in the presence of an adsorbate or the presence of differing types of porosity. Such features could not be discovered from the interpretation of an adsorption isotherm or for that matter from the use of either high resolution electron microscopy or immersion calorimetry alone. In

place of immersion calorimetry, the limiting micropore volumes W_o could be derived from adsorption experiments using the vapour from the molecular probes and the Dubinin-Radushkevich equation. However, this technique is extremely time consuming and the low vapour pressures and slow adsorption equilibria lead to difficulties. Immersion calorimetry on the other hand, takes relatively little time and can be readily repeated to check the accuracy of the results.

5.7 Difference in the Quantity Measured with HREM as Opposed to Immersion Calorimetry

A point that should be raised in relation to the comparison of the two techniques used to obtain micropore size distributions is that they do not measure the same quantity. With immersion calorimetry it is the pore volume occurring within a specified pore width range that is deduced, whereas in the case of electron microscopy it is the number, or percentage of pores within the range that are seen to be exiting the sample that is obtained. Obviously, these two quantities are not equivalent although one would assume that a greater number of pores would be matched with a corresponding increase in pore volume, provided the distribution of pore lengths is not greatly affected. In any event, it is the only means available for comparing the techniques, as the volume of the porosity cannot be deduced from measurements carried out on electron micrographs. The method used when

measuring pores from the micrographs is analogous to that employed by topographical scientists, whereby a grid is superimposed onto a map and the percentage of specific features is analysed by frequency of occurrence of these features at the grid line intersections which is then extrapolated to the area of the map as a whole. With the pore measuring technique, the use of a grid is replaced by the sample edge, the number of pores occurring on this line then being extrapolated to the sample as a whole. It may be claimed that there are many problems associated with such a method, however the correlations obtained, for the samples studied here at least, do seem to indicate that it is a valid technique, at least for small pore widths. Perhaps with a study of a greater number of samples and the development and utilisation of more powerful image processing programs the effectiveness of such a statistical method could be enhanced further but as an initial study, the correlations produced here are at least an indication of the feasibility of such studies.

The main problem that is associated with this method of obtaining a pore size distribution from a sample is that only slit-pores are measured because by their very nature they are the only ones observed to be leaving the specimen edge. Other pore types that may be present, as has been stated earlier, tend only to be seen within the main body of the sample.

5.8 Porous Structure of Carbons as Revealed by HREM

The fact that the general appearance of the CEP samples was similar, with all of them displaying lattice structures of both short and long range as well as the porous ribbon-like structure albeit to varying degrees has been discussed earlier so no attention will be given to such features in this section. The only obvious variation in the microporous structure in the pore width region below around 0.6 nm was the distribution of the micropore sizes, the various lengths, shapes, branches and angular bends were visible in all of the specimens. The major difference, to be discussed here, is the variation in the porous structure in the pore size range greater than 0.6 nm. The lower burn-off carbons: CEP-0, CEP-17 and CEP-18 as well as CEP-35 displayed mainly small slit pores. The larger type pores described earlier as cavities were apparent in these samples but by no means were they extensive. From the many micrographs that were taken of these samples only very few of these pores were observed. When CEP-49 was studied, it was found that in this case also there were very few of this type of pore. Plate 20 shows some larger pores, their presence being indicated by arrows. This sample does not have the "loose" structure associated with the other higher burn-off carbons. For the carbons mentioned above, except for CEP-49, good agreement had been found between the immersion and electron microscopical techniques. The calorimetric results had also indicated the presence of very little larger pores which seemed to be the case with electron microscopy.

It is in the case of CEP-31, CEP-*35 and CEP-51 that the larger pore type is commonly observed. The two lower burn-off carbons showed the presence of these pores as can be seen in plates 16 and 17. However, it was in the case of CEP-51 that they were most extensively imaged. These observations fit in well with the immersion data that were obtained for these samples. All three specimens showed the presence of relatively high pore volumes accessible to perchlorocyclopentadiene and in the case of CEP-51 in particular there was a vast quantity of porosity in the region above 0.6 nm, in fact the pore volume in this region was greater than the total pore volume for many active carbon samples. It would be expected and indeed it was found to be the case that in the micrographs of this sample more of such larger pore types were observed. Plate 21 shows many such voids. This porosity is neither constantly sized nor shaped. There are pores such as those denoted A and B which appear to be enclosed by a single curved layer plane leading to an approximately circular shape. These two pores have widths of 0.82 nm and 0.1 nm respectively. These values were not corrected using the Everett and Powl treatment. Also, in the same area, indicated by C there are pores which approximate to slit pores, being enclosed by pairs of layer planes whose spacings vary from approximately 0.7 to 0.1 nm. An interesting feature visible at point D is the presence of both large and small slit-pores together. These pores which appear to be interconnected have arisen from the arrangement between some very contorted layer planes. This area has been drawn schematically in figure 5.29. Such a

feature shows well the variety of pore widths and the difficulty associated with assigning a value to the width of such pores from microscopical determinations.

Figure 5.29 Schematic diagram of pore structure.

Even with such twisted planes, some degree of parallelism is still apparent between a few layers. Similar features can also be seen at E and F and for that matter extensively throughout the sample. At G, yet another type of void is apparent. This has a diameter of approximately 0.2 nm. However, rather than being enclosed by one or two layer planes, its walls are composed of many layer planes. This perhaps emphasizes the danger of imagining a pore as a structural feature in its own right rather than as an area of low electron density or an area in which no structure exists. Plate 18 shows similar features to those presented by the previous plate showing that the occurrence of these pores is not an isolated incident.

The above plates show that the larger pores are not simply enlargements of those in the sub 0.6 nm range but are of a different and much more disordered nature. The "loose" appearance of these pores also suggests that they could be more flexible than the smaller pores which are generally

contained within a much denser structure. It would appear that the burning out of layer planes after greater and greater degrees of activation shifts the porosity to a larger average pore size by removing the more ordered smaller pores and leaving such spaces in the structure as to allow the formation of the very distorted larger pore types. The pores described here are not unlike the cage-like voids described by Marsh et al. (1982), although the ones in the present work are perhaps a little smaller. The fact that the smaller and larger pores observed in this study appear to have different structures may justify the use of the terms ultra-micropore and super-micropore, although the naming of pores is generally used to reflect the different pore filling mechanisms that occur within them. Some larger sized pores do have structures not dissimilar to those in the sub 0.6 nm range, perhaps therefore prefixes other than ultra- and super- should be selected, ones which reflect the pore structure rather than purely the size. Such a classification would reflect the importance of using high resolution electron microscopy in conjunction with a technique such as immersion calorimetry. With such a combination, immersion data would show the presence and volume of larger pores with the microscopical evidence then illustrating the type of pores that were present. Even microscopy alone could give a semi-quantitative analysis of the pore structure although no volume terms could be determined.

5.9 Comparison of the Behaviour of CEP-17,CEP-31, CEP-*35 and CEP-51

An examination of the volume terms shown in tables 5.2, 5.6, 5.9 and 5.11 shows that the micropore volume increases as the degree of activation of the sample increases, although this behaviour is perhaps not unexpected. A more detailed investigation of these results was undertaken to see in what way the micropore distribution actually changed with the degree of burn-off of the sample.

Table 5.13 shows the values of W(L) and dW(L)/dL that were obtained for each of the samples CEP-17, CEP-31, CEP-*35 and CEP-51 from immersion calorimetry. These values have already been presented in earlier tables but for convenience they have been displayed again in a form where they appear together. The micropore size distributions of these samples have also been presented in a superimposed form which can be seen in figure 5.30.

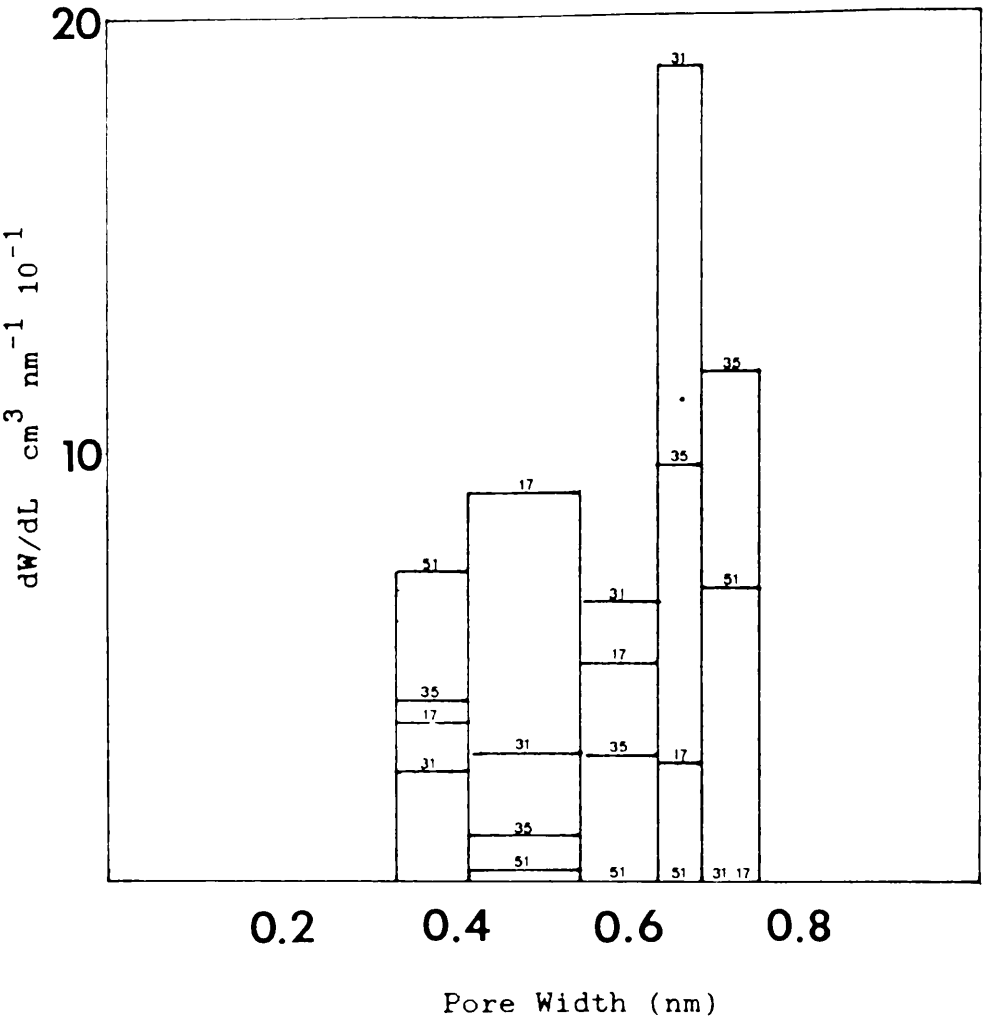

Figure 5.30

Micropore size distribution of CEP-17, CEP-31, CEP-*35 and CEP-51 obtained from immersion calorimetry.

Table 5.14 Values of W(L) and dW(L)/dL for CEP-17, CEP-31, CEP-*35 and CEP-51.

Sample	17	31	*35	51	17	31	*35	51
Probe	W(L) (cm^3g^{-1})				dW(L)/dL			
CH_2Cl_2	0.266	0.329	0.378	0.534	0.36	0.25	0.41	0.71
C_6H_6	0.237	0.309	0.345	0.477	0.89	0.29	0.10	0.02
C_6H_{12}	0.121	0.271	0.332	0.475	0.50	0.64	0.29	-0.04
CCl_4	0.076	0.213	0.306	0.478	0.28	1.88	0.96	0.00
$C_{10}H_{16}$	0.062	0.119	0.258	0.478	-0.01	-0.01	1.17	0.68
C_5Cl_6	0.063	0.120	0.176	0.442				

The simplest way to study the behaviour of the materials is to consider the differences in the properties between pairs of samples. Comparing the micropore size distributions of CEP-17 and CEP-31, it is apparent that there is a decrease in the volume of porosity in the range 0.33 to 0.54 nm and an increase from 0.54 to 0.68 nm as the sample becomes more activated. In the range 0.68 to 0.75 nm, both samples display the presence of no porosity, however in the region above 0.75 nm the volume of porosity is greater in CEP-31 than in CEP-17. The formation of the new larger pores is obviously developed at the expense of the smaller ones. In the case of CEP-31 and CEP-*35 there is an increase in porosity from 0.33 to 0.41 nm, a decrease from 0.41 to 0.68 nm followed by another increase in the region above 0.68 nm. The increase in the porosity below 0.41 nm may be attributed to the opening of sealed-

off microporosity. There is of-course the possibility that these are totally new pores. If new pores of this small size are formed by the mechanism whereby the activating gas burns away a layer plane then some collapse of the remaining layer planes must occur. The reason for this is as follows: The spacing between a group of three layer planes would be, at least, 0.67 nm. The burning out of a central layer would leave a void of accessible width 0.47 nm if the Everett and Powl value of 0.2 nm is used for twice the radius of a carbon atom. Therefore, unless the layer planes do in fact collapse towards each other it would not be possible for such a mechanism to result in the formation of pores with widths smaller than 0.47 nm. Plate 22, which is of one of the earlier samples, CEP-18, shows possible evidence for such a collapsing mechanism although it must be noted that such examples as stated here were not extensively observed. The boxed area of this micrograph is also shown schematically in the bottom right of the plate. The layer planes in this area turn through sharp angular bends, indicating the presence of sp^3 hybridised bonds in addition to the sp^2 bonds normally present in a flat graphitic carbon layer plane. The interlayer spacing of the group of three planes is 0.34 nm, that normally associated with turbostratic carbon. However, along this area the central layer is no longer present. The spacing between the remaining two layer planes appears to be only 0.5 nm and not the 0.68 nm that would have been expected had these two planes maintained the same distance from each other. The area enclosed by the remaining two planes is obviously a very small pore as

after subtraction of the value 0.2 nm, there would be a width of 0.3 nm accessible to an adsorbate molecule. There is of-course no evidence to suggest that the missing layer plane was burnt out by the carbon dioxide activation process and this feature may always have been present in this carbon. The structure does however indicate the influence that sp^3 hybridised bonding may have on the flexibility or relative positioning of carbon layer planes.

For the final two carbons, CEP-*35 and CEP-51, there is again an increase in the porosity below 0.41 nm which is accompanied by a decrease in the pore volume from 0.41 to 0.75 nm. An examination of the pore volumes accessible to perchlorocyclopentadiene show the amount of porosity to increase vastly in the region above 0.75 nm. These results as a whole show that except for the increase in pore volume below 0.41 nm, the pores are shifted to larger and larger sizes, the smaller pores no doubt being destroyed as they are incorporated into larger ones.

In the CEP series examined by Kraehenbuehl et al. (1986) a similar trend was observed, if less clearly defined due to the broadness of the distributions. It was considered better not to compare the results obtained in the present work for the CEP series with those of Kraehenbuehl et al. due to the variations encountered in the behaviour of samples with similar degrees of activation. The reason for the differences in the two series such as those between CEP-35 and CEP-*35 are not clear, although perhaps some

factor was changed between the production of the earlier series and the ones obtained in the course of the present work. Whatever the reason, for the purposes of considering the processes occurring in the CEP carbons, it is better to consider the two series separately.

5.10 Micropore Size Distributions from Isotherms

The micropore size distributions obtained in the course of the present work illustrate the dangers of estimating the average size of the micropores from an adsorption isotherm as opposed to direct methods such as immersion calorimetry or high resolution electron microscopy. In order to show this point more clearly a number of such estimates have been made employing a variety of techniques: The method of Kraehenbuehl using equations 3.44 and 3.45 described earlier; the method of Dubinin and Stoeckli also described previously (equation 3.42) and the method of McEnaney (1987). In this the final of the three techniques, two values are obtained, one from utilising the equation:

$$W_m = 4.691\exp(-0.0666E_o)\text{nm}$$

an equation based on the use of molecular probes and the other is derived from the theoretical calculations of Everett and Powl in which a graph of E_o against W_d is used to obtain the pore width. In this case McEnaney suggests that the value 0.24nm should be subtracted from W_d in order to obtain the accessible pore width W_a. With this method the values should reflect the upper and lower

limits of the micropore dimension. It must be stressed at this point that each of these authors has stated that their methods are only approximate.

It is difficult to make a direct comparison of the results derived from these techniques with those obtained in the present work because of the volume of porosity occurring in the region above 0.75nm which could not be put into specific pore width ranges. However, a rough indication can be obtained.

The results from the adsorption of benzene onto samples CEP-17, CEP-31, CEP-*35 and CEP-51 were used to determine the average micropore widths using the methods described above. Table 5.15 illustrates the values obtained from using each of the techniques.

Table 5.15 Average micropore sizes descibed from E_o values.

SAMPLE	Kraehenbuehl	Dubinin-Stoeckli	McEnaney	
			graph	equation
CEP-17	0.226	0.515	0.46	0.521
CEP-31	0.368	0.555	0.49	0.609
CEP-*35	0.461	0.584	0.50	0.675
CEP-51	0.686	0.670	0.515	0.866

From this table it is instantly apparent that there is

very little agreement between the results obtained from the various methods. For the carbon of lowest burn-off CEP-17 all the techniques except that of Kraehenbuehl show an approximate agreement with the distribution obtained in the present work. However, for the three higher burn-off carbons, all of the techniques seem to underestimate the average micropore size. The method closest in value is the equation derived by McEnaney although this does still appear to be low. Interestingly, McEnaney (1987) claimed that this method probably gave an overestimate of the pore widths. Although the techniques described here have been claimed to work for other carbons, it is obvious that such is not the case for the CEP series assuming the calorimetric and microscopical distributions obtained here to be true. The techniques do appear to be in reasonable agreement for CEP-17, a carbon with a fairly narrow pore size distribution. This sample also does not possess any of the larger pore types associated with CEP-31, CEP-*35 and CEP-51, therefore it is possibly the presence of these larger type pores that are causing the discrepancy between the techniques. This implies that in order to apply these methods to obtain the average micropore size, it must first be known whether or not the carbon being studied is one to which the technique is applicable. Therefore, it is probably better to avoid such methods. In any case, the average size of the micropores is not of any great informative value unless the distribution of pores around this value can be deduced. It has been suggested that the micropore distribution may be obtained theoretically from the adsorption isotherm, however the most reliable of

evidence can only be obtained from direct methods of determining the distribution. A final point to present further the problems associated with determining the average pore size from a parameter determined from the adsorption isotherm such as E_o is the case of CEP-35 and CEP-*35 studied here. In this case the values of E_o were quite similar, however the micropore size distributions were very different.

5.11 Studies of Coke Samples

In addition to the series of CEP carbons that were studied in the course of this work, a brief investigation was also undertaken of some coke samples supplied by M. Shevlin of Glasgow University. The two cokes that were examined were Redcar I Ex-Tuyere and Redcar I Feed. The intention was to activate these samples to varying degrees and study them in a manner analogous to that employed in the investigation of the CEP samples. The cokes were activated at 850°C using carbon dioxide, the flow rates of which along with the activation times and resulting degrees of burn-off can be seen in table 4.1 of section 4.7. The cokes were studied initially by both immersion calorimetry and density pycnometry. The method that was employed for measuring the densities of the samples was not a highly accurate technique and the values probably do not reflect the true densities of the materials, nonetheless the method should reflect relative values thus allowing differences between the samples to be discovered. The values that were obtained for the densities and immersion

enthalpies of the samples can be found in table 5.16. These values all refer to the use of benzene as the medium in which the density was to be determined and into which the samples were immersed.

Table 5.16 Results from density and immersion measurements on coke samples. Both values relate to experiments conducted with benzene.

Sample	Burn-Off	$\Delta H_i (Jg^{-1})$	Density(gcm^{-3})
Redcar I ET	0	0.509	2.07
Redcar I ET	8	0.160	2.05
Redcar I ET	22	0.030	2.06
Redcar I ET	39	0.592	2.05
Redcar I Feed	0	0.223	1.92
Redcar I Feed	7	2.352	1.95
Redcar I Feed	19	3.875	1.96

The density values, although different for the two series, are equivalent within a particular series within the errors of the experimental set-up. Even at degrees of activation of almost 40% there is no obvious change. The results from immersion calorimetry also show there to be no development of an internal surface. In fact the values from the immersion experiments are so low as to suggest that these samples possess no internal surface whatsoever. Although there appear to be slight differences in these

values, no comparison can be made between them as they are so low that experimental error will contribute vastly to them.

For these samples it had originally been thought that activation with carbon dioxide may have opened up sealed-off porosity present within them. This however, was shown not to be the case. It appears that rather than the preferential burn-off of certain areas associated with pore formation in active carbons, during activation of these cokes there is no preferred area open to attack by carbon dioxide. This would mean that the coke would be attacked equally in all areas and there would be a gradual eating away of the coke particle without the formation of any microporous structure.

CONCLUSION

These studies on the feasibility of using high resolution electron microscopy and immersion calorimetry in conjunction for the study of active carbons have resulted in a number of points. For most of the carbons studied, a reasonable agreement was found between the two techniques especially in the region of pore sizes below around 0.6nm. In view of the relatively small number of pores that were measured from microscopy, particularly in the case of the three samples initially studied, the agreement obtained was extremely good. Perhaps an analysis of a greater number of pores would yield an even better agreement between the techniques. This would be of most value where a broad distribution of pores is present, for obviously in such a situation, statistics are more important than in a distribution where all of the pores fall into the same small size interval.

The disagreement encountered in the larger pore size range indicated the presence of pores of a different nature i.e. not slit-pores. It also appeared that the volume of such porosity increased with increasing degree of burn-off. Another implication of these studies was that the discrepancies occurring for one of the carbons, suggested that the differences in the micropore size distributions obtained from using the two techniques may be used to provide evidence of exfoliation of the porous structure in the presence of a vapour or liquid.

The results presented in this work, perhaps most importantly, consider the definition of a pore and provide direct evidence for the reduced interaction radius of an adsorbed molecule suggested by Everett and Powl. Although no definite value could be produced for this reduction, and indeed there is probably no specific value for this quantity, it is no doubt dependent on both the adsorbate molecule being utilised and the adsorbent, the value of 0.2nm used in the course of this work to account for both the finite width associated with a carbon atom and the reduced interaction value seems to be an acceptable value for obtaining a micropore size distribution from high resolution electron microscopy which is in good agreement with that obtained from immersion calorimetry.

In conclusion, the combination of the two techniques results in a powerful method for the elucidation of porous structure in active carbons, with both the agreements and disagreements leading to conclusions on the porous structure of the sample.

REFERENCES

ABRAMOVITZ, M. and STEGUN, I.A., "Handbook of Mathematical Functions", Dover, New York, p264, (1965).

AHMED, H., Proc. 25th. Anniv. Meeting EMAG, 30, Institute of Physics, London, (1971).

ALI, S. and McENANEY, B., J. Coll. Int. Sci., 107, 355, (1985).

ALLPRESS, J.G., HERVAT, F.A., MOODIE, A.F. and SANDERS, J.V., Acta. Cryst., A30, 280, (1972).

ANDERSEN, J.C. ,"Refining of Oils and Fats for Edible Purposes", Academic Press, New York, p93, (1953).

AST, D.G., KRAKOW, W. and GOLDFARB, W., Report No.2328, Mats. Sci. Centre, Cornell Univ., (1974).

A.S.T.M. INDEX, Publication PO 15-15i, (1965).

BACON, G.E., Acta. Cryst., 3, 137, (1950).

BACON, G.E., Acta. Cryst., 4, 558, (1951).

BACON, G.E., Acta. Cryst., 5, 392, (1952(a)).

BACON, G.E., Acta. Cryst., 5, 492, (1952(b)).

BACON, G.E., Acta. Cryst., 7, 359, (1954).

BACON, G.E., AERE Report, M/R 2702, (1958).

BAIRD, T. and FRYER, J.R., Carbon, 12, 381, (1974).

BAIRD, T., FRYER, J.R. and GRANT, B., Nature, 233, 329, (1971).

BAKER, C., GILLIN, C.M. and KELLY A., 2nd Ind. Carbon and Graphite Conf., Society of Chemical Industry, London, (1965).

BALLERINI, L., Travail de Diplome, University of Neuchâtel, (1986).

BAN, L.L., CRAWFORD, D. and MARSH, H., J. Appl. Cryst., 8, 415, (1975).

BERING, B.P., DUBININ, M.M. and SERPINSKY, V.V., J. Coll. Int. Sci., 21, 378, (1966).

BERNAL, J.D., Proc. Roy. Soc. (London), A106, 749, (1924).

BISCOE, J. and WARREN, B.E., J. Appl. Phys., 13, 364, (1942).

BOEHM, H.P. and COUGHLIN, R.W., Carbon, 2, 1, (1964).

BOEHM, H.P. and HOFFMAN U., Z. Anorg. Allg. Chem., 282, 278, (1955).

BOERCHIA, A. and BONHOMME, P., Optik, 39, 437, (1974).

BOLLMAN, W., Phil. Mag., 5, 621, (1960).

BOLLMAN, W., Proc. 5th Conf. Carbon, Phil. II, Pergamon Press, London, p303, (1961(a)).

BOLLMAN, W., Proc. Eur. Reg. Conf. Electron Microscopy, Delft, p330, (1961(b)).

BOLLMAN, W., Proc. 1st Int. Conf. Properties of Reactor Materials, p132, (1961(c)).

BOURAOUI, A. and MERING, J., Carbon, 1, 465, (1964).

BRUNAUER, S., DEMING, L.S., DEMING, W.S. and TELLER, E., J. Am. Chem. Soc., 62, 1723, (1940).

BRUNAUER, S., EMMETT, P.H. and TELLER, E., J. Am. Chem. Soc., 60, 309, (1938).

CHARLIER, M.-F. and CHARLIER, A., in "Chemistry and Physics of Carbon", (ed. P.A. Thrower), Marcel Dekker, New York, vol.20, p59, (1987).

CHENEY, H.A., McALLISTER, S.H., FOUNTAIN, E.N., ANDERSON, J. and PETERSON, W.H., Ind. Eng. Chem., 42, 2580, (1950).

CHESSICK, J.J. and ZETTLEMOYER, A.C., Adv. Catalysis, 11, 263, (1959).

CLINT, J.H., J. Chem. Soc. Faraday Trans. I, 69, 1320, (1973).

COSSLETT, V.E., in "Practical Electron Microscopy", Oxford University Press, London, (1951).

COSSLETT, V.E., Q. Rev. Biophysics, 2, 95, (1969).

COSSLETT, V.E., Inst. Elect. Eng., 117, 1489, (1970).

COSSLETT, V.E., Contemp. Phys., 22, no.2, 3, (1981(a)).

COSSLETT, V.E., Contemp. Phys., 22, no.2, 147, (1981(b)).

COULSON, C.A., Nature, 159, 265, (1947).

COULSON, C.A. and TAYLOR, E., Proc. Phys. Soc., A, 65, 815, (1952).

COWLEY, J.M., in "Physical Aspects of Electron Microscopy and Microbeam Analysis", (ed. B.M. Siegel and D.R. Beamen), Wiley, New York, p3, (1975).

COWLEY, J.M. and MOODIE, A.F., Acta. Cryst., 10, 609, (1957).

CRACKNEL, A.P., Adv. Phys., 18(70), 681, (1969).

CREWE, A., EGGENBERGER, D.N., WALL, J. and WALTER, L.J., Rev. Sci. Inst., 39, 576, (1968).

de BROGLIE, L., Phil. Mag., 47, 446, (1924).

de SAUSSURE, N.T., Gilbert's Ann., 59, 94, (1843).

DACEY, J.R., in "The Solid-Gas Interface", (ed. E.A. Flood), Arnold, London, vol.2, p995, (1967).

DANNENBERG, E.M. and BOONSTRA, B.B.S.T., Ind. Eng. Chem., 47, 339, (1955).

DEBEYE, P. and SCHERRER, P., Phys. Z., 18, 291, (1917).

DUBININ, M.M., Quart. Rev. Chem. Soc., 9, 101, (1955).

DUBININ, M.M., in "Adsorpton-Desorpton Phenomena", (ed. F. Ricca), Proc. 2nd Int. Conf. 1971, Academic Press, London, (1972).

DUBININ, M.M., in "Prog. in Surface and Membrane Sci.", (ed. D.A. Cadenhead), Academic Press, London, vol.9, p1, (1975).

DUBININ, M.M., in "Characterisation of Porous Solids", (eds. S.J. Gregg, K.S.W. Sing and H.F. Stoeckli), SCI, London, (1979).

DUBININ, M.M., Carbon, 18, 355, (1980).

DUBININ, M.M. and ASTAKHOV, V.A., "Molecular-Sieve Zeolites-II", American Chemical Society, Washington, (1971(a)).

DUBININ, M.M. and ASTAKHOV, V.A., Izv. Akad. Nauk. SSSR, Ser. Khim., 1, 5, (1971(b)).

DUBININ, M.M. and ASTAKHOV, V.A., Izv. Akad. Nauk. SSSR, Ser. Khim., 1, 11, (1971(c)).

DUBININ, M.M. and KADLEC, O., Carbon, 13, 263, (1975).

DUBININ, M.M. and POLSTYANOV, E.F., Izv. Akad. Nauk. SSSR, Ser. Khim. N4, 610, (1966).

DUBININ, M.M. and STOECKLI, H.F., J. Coll. Interface Sci., 75, 34, (1980).

DUBININ, M.M. and TIMOFEEV, D.P., Dokl. Akad. Nauk. SSSR, 54, 705, (1946).

DUBININ, M.M. and TIMOFEEV, D.P., Dokl. Akad. Nauk. SSSR, Ser. Khim., 55, 137, (1947).

DUBININ, M.M. and TIMOFEEV, D.P., Zh. Fiz. Khim., 22, 133, (1948).

DUBININ, M.M. and ZAVERINA, E.D., Zh. Fik. Khim., 23, 1129, (1949).

DUBININ, M.M. and ZAVERINA, E.D., Zh. Fiz. Khim., 72, 319, (1950).

DUPOUY, G. and PERRIER, F., J. Microscopie, 1, 167, (1962).

EELES, W.T. and WILSON, A.J.C., Nature, 205, 66 (1965).

EISENHANDLER, C.B. and SIEGEL, B.M., J. Appl. Phys., 37, 1963, (1966).

ERGUN, S., J. Phys. Chem., 60, 480, (1956).

ERGUN, S., in "Chemistry and Physics of Carbon", (ed. P.L. Walker Jr.), Marcel Dekker, New York, vol.1, p1, (1965).

ERGUN, S., Carbon, 6, 141, (1968(a)).

ERGUN, S., in "Chemistry and Physics of Carbon", (ed. P.L. Walker Jr.), Marcel Dekker, New York, vol.3, p211, (1968(b)).

ERGUN, S. and GIFFORD, T.J., J. Appl. Cryst., 1, 313, (1968).

ERGUN, S. and GIFFORD, T.J., J. Chim. Phys. Phisicochim. Biol., 99, (1969).

ERICKSON, H.P., Adv. Opt. Elec. Micros., 5, 163, (1973).

EVANS, M. and MARSH, H., in "Characterisation of Porous Solids", (eds. S.J. Gregg, K.S.W. Sing and H.F. Stoeckli), SCI, London, p53, (1979).

EVERETT, D.H. and POWL, J.C., J. Chem. Soc. Faraday Trans. 1, 72, 619, (1976).

EWALD, P.P.,Sitzungsber Munch. Akad., 4, 7, (1914).

FINCH, G.I. and WILMAN, H., Proc. Roy. Soc. (London), A155, 345, (1936).

FISCHBACH, D.B., in "Chemistry and Physics of Carbon", (ed. P.L. Walker Jr.), Marcel Dekker, New York, vol.7, p1, (1971).

FONTANA, F., Memorie Mat. Fis. Soc. Ital. Sci. 1, 679, (1777).

FRANK, J., Optik, 38, 519, (1973).

FRANKLIN, R.E., Acta. Cryst., 3, 107, (1950).

FRANKLIN, R.E., Acta. Cryst., 4, 253, (1951(a)).

FRANKLIN, R.E., Proc. Roy. Soc., (London), A209, 196, (1951 (b)).

FRIEDEL J.,"Dislocations", Addison-Wesley, London, (1964).

FRYER, J.R., Soc. Chem. Ind. Proc. 3rd Int. Conf. Carbon and Graphite, Glasgow, vol. 13, (1970).

FRYER, J.R., 8th Int. Cong. Elect. Micros. Canberra, (eds. J.K. Sanders and D.J. Goodchild), Australian Academy of Science, Canberra, vol.1, p680, (1974).

FRYER, J.R., in "Characterisation of Porous Solids", (eds. S.J. Gregg, K.S.W. Sing and H.F. Stoeckli), SCI, London, p41, (1979).

FRYER, J.R., Carbon, 19, 431, (1981).

FRYER, J.R., Mol. Cryst. Liq. Cryst., 96, 275, (1983).

GADSBY, J., LONG, F.J., SLEIGHTHOLM, P. and SYKES, K.W., Proc. Roy. Soc. (London), A193, 357, (1948).

GOLDMAN, F. and POLANYI, M., Z. Phys. Chem., 132, 321, (1928).

GOODMAN, P. and MOODIE, A.F., Acta. Cryst., A30, 280, (1974).

GRADSHTEYN, I.S. and RHYZHIK, I.M., "Tables of Integrals, Series and Products", Academc Press, London, 525, (1980).

GREGG, S.J. and LANGFORD, J.F., Trans. Faraday. Soc., 65, 1394, (1969).

GREGG, S.J. and SING, K.S.W.,"Adsorption Surface Area and Porosity", Academic Press, London, (1967).

GREGG, S.J. and SING, K.S.W., "Adsorption, Surface Area and Porosity", 2nd ed., Academic Press, London, (1982).

GRINTON, G.R. and COWLEY, J.M., Optik, 34, 221, (1971).

GRISDALE, R.O., J. Appl. Phys., 24, 1288, (1953).

HAERRING, R.R., and MROZOWSKI, S., Prog. Semicond., 5, 273, (1960).

HALL, C.E., in "Introduction to Electron Microscopy", London, (1953).

HALL, C.E. and HINES, R.L., Philos. Mag., 21, 1175, (1970).

HANZEN, K.J., Adv. Opt. Electron Microscopy, 4, 1, (1971).

HANZEN, K.J. and TREPTE, L., Optik, 32, 519, (1971).

HASSEL, O. and MARK, H., Z. Physik., 25, 317, (1924).

HEERSCHAP, M., DELAVIGNETTE, P. and AMELINCKX, S., Carbon, 1, 235, (1964).

HILLIER, J. and VANCE, A.W. in "Electron Optics and the Electron Microscope", Wiley, New York, (1945).

HIRSCH, P.B., HOWIE, A., NICOLSON, R.B., POSHLEY, D.W. and WHEELANS, M.J., in "Electron Microscopy of Thin Crystals", Butterworths, London, (1965).

HONIG, J.M., Ann. N.Y. Acad. Sci., 58, 741, (1954).

HOUSKA, C.R. and WARREN, B.E., J. Appl. Phys., 25, 1503, (1954).

HOWIE, A., KRIVANEK, O.C. and RUDEE, M.L., Phil. Mag. 27, 235, (1973).

HYNDSHAW, A.Y., J. New Eng. Water Works Assoc., 79, 236, (1965).

IIJIMA, S., Optik, 48, (2), 193, (1977).

I.U.P.A.C., Pure and Appl. Chem. 57, 603, (1985).

JANOSI, A. and STOECKLI, H.F., Carbon, 17, 465, (1979).

KAHLE, H., Chem. Ing. Techn., 25, 144, (1953).

KAHLE, H., Chem. Ing. Techn., 26, 75, (1954).

KAISER, K., Brauwelt, 97, 1203, (1957).

KAPTEIJN, F. and MOULIJN, J.A., in "Carbon and Coal Gasification", (eds. J.L. Figueiredo and J.A. Moulijn), NATO ASI Series, Series E: Applied Sciences, No. 105, p291, (1986).

KIRKWOOD, J.G., Phys. Zeits. 33, 57, (1932).

KNOLL, M. and RUSKA, E., Ann. d. Physik., 12, 607, (1932).

KOBAYASHI, K. and O'HARA M., Proc. 6th. Int. Cong. E. M., Kyoto, 1, 579, (1966).

KOBAYASHI, K. and SAKAOKU, K., Lab. Inst., 14, (6), pt.2, 1097, (1965).

KOMODA, T., Jap. J. Appl. Phys., 5, 179, (1966).

KRAEHENBUEHL, F., These de doctorat, Neuchâtel, (1983).

KRAEHENBUEHL, F., Unpublished Results, Neuchâtel, (1984-86).

KRAEHENBUEHL, F., STOECKLI, H.F., ADDOUN, A., EHRBURGER, P. and DONNET, J.B., Carbon, 24, 483, (1986).

KRAKOV, W., AST, D.G., GOLDFARB, W. and SIEGEL, B.M., Phil. Mag. 33, 985, (1976).

KRAUS, G., J. Phys. Chem., 59, 343, (1955).

KRIVANEK, D.L. and HOWIE, A., J. Appl. Cryst., 8, 213, (1975).

LAIDLER, D. and TAYLOR, A., Nature, 146, 130, (1940).

LAINE, N.R., VASTALA, F.J. and WALKER, P.L., Proc. 5th Conf. on Carbon, Pergammon Press, 2, 211, (1963).

LEHMER, O., Atomwirtsch, 5, 356, (1960).

LENNARD-JONES, J.E., Physca, 4, 941, (1937).

LEWIS, W.K., GILLILAND, E.R. and McBRIDE Jr., G.T., Ind. Eng. Chem., 41, 1213, (1949).

LIPPENS, B.C., LINSEN, B.G. and DE BOER, J.H., J. Catalysis, 3, 32, (1964).

LIPSON, H. and STOKES, A.R., Nature, 149, 328, (1942(a)).

LIPSON, H. and STOKES, A.R., Proc. Roy. Soc. (London), A181, 101, (1942(b)).

LONDON, F., Z. Phys. Chem., 11, 222, (1930(a)).

LONDON, F., Z. Physik., 63, 245, (1930(b)).

LUKESH, J.S., Phys. Rev., 86, 226, (1950).

LUKESH, J.S., J. Chem. Phys., 19, 384, (1951(a)).

LUKESH, J.S., J. Chem. Phys., 19, 1203, (1951(b)).

LYNCH, D.F. and O'KEEFE, M.A., Acta Cryst., A28, 536, (1972).

McCLURE, J.W., Proc. 3rd Carbon Conf., Buffalo, Pergammon Press, New York, p179, (1959).

McDOWELL, L., J. Appl. Polymer Sci., 5, 663, (1961).

McENANEY, B., Carbon, 25, 69, (1987).

McENANEY, B., Carbon, 26, 267, (1988).

MAIRE, J., COLAS, H. and MAILLARD, P., Carbon, 6, 555, (1968).

MAIRE, J. and MERING, J., in "Chemistry and Physics of Carbon", (ed. P.L. Walker Jr.), Marcel Dekker, New York, vol.6, p125, (1970).

MARSH, J.D.F., Publication No. 393, The Institution of Gas Engineers, London, (1951).

MARSH, H., CRAWFORD, D., O'GRADY, T.M. and WENNERBERG, A., Carbon, 20, 419, (1982).

MAUGHIN, C., Bull. Soc. Fr. Min., 49, 32, (1926).

MERING, J. and MAIRE, J., J. Chem. Phys., 57, 803, (1960).

MILLWARD, G.R. and JEFFERSON, D.A., in "Chemistry and Physics of Carbon" (eds. P.L. Walker Jr. and P.A. Thrower), Marcel Dekker, New York, vol.14, p1, (1978).

MISELL, D.L., Adv. Electronics and Electron Physics, 32, 63, (1973).

MISELL, D.L., J. Phys., A4, 798, (1976).

MITSCHERLICH, E., Pogg. Ann., 59, 94, (1843).

MULLER, A., Proc. Roy. Soc. (London), 154A, 624, (1936).

MURATA, Y., BAIRD, T. and FRYER, J.R., Nature, 263, No.5576, 401, (1976).

NIXON, W.C., AHMED, H., CATTO, C.J.D., CLEAVER, J.R.A, SMITH, K.C.A., TIMBS, A.E., TURNER, P.W. and ROSS, P.M., EMAG, 13, (1977).

OBERLIN, A., THERRIERE, G. and BOULMIER, J.-L., J. de Microscopie, 21, 301, (1974).

PARSONS, J.R. and HOELKE, C.W., Phil. Mag., 30, 135, (1974).

PAULING, L., Proc. Natl. Acad. Sci., 56, 1646, (1966).

PERRET, R. and RULAND, W., J. Appl. Cryst., 1, 308, (1968).

PERRET, R. and RULAND, W., Paper 21 Paris Conf. J. Chim. Phys. (Special Issue), 96, (1969).

POLANYI, M. and WELKE, K., Z. Phys. Chem., 132, 371, (1928).

RADUSHKEVICH, L.V., Zh. Fiz. Khim., 23, 1129, (1949).

RAMSEY, Proc. Roy. Soc. (London), A76, 111, (1905).

RAMSEY, Proc. Roy. Soc. (London), A80, 599, (1908).

RAND, B., J. Colloid Interface Sci., 56, 337, (1976).

READ, W.T., "Dislocations in Crystals", McGraw-Hill, New York, (1953).

REIF, A.E., J. Phys. Chem., 56, 778, (1952(a)).

REIF, A.E., J. Phys. Chem., 56, 785, (1952(b)).

RILEY, H.L., Quart. Revs., 1, 59, (1947).

ROBINSON Jr., G.Y., Advan. Cryogen. Eng., 7, 137, (1961).

ROWE, R.N., Air Eng. 6(7), 15, (1964).

RUDEE, M.L. and HOWIE, A., Phil. Mag., 25, 1001, (1972).

RULAND, W., Paper 111-12, Symp. Carbon, Tokyo, (1964).

RULAND, W., Acta. Cryst. 18, 992, (1965(a)).

RULAND, W., Carbon, 2, 365, (1965(b)).

RULAND, W., Acta. Cryst., 22, 615, (1967(a)).

RULAND, W., Paper S159, 8th Carbon Conf., Buffalo, Pergammon Press , New York (1967(b)).

RULAND, W., in "Chemistry and Physics of Carbon", (ed. P.L. Walker Jr.), Marcel Dekker, New York, vol.4, p1, (1968).

SCHEELE, C.W., "Chemical Observations on Air and Fire", 182, (1780).

SCHERZER, D., J. Appl. Phys., 20, 20, (1949).

SCHILLER, C. and MERING, J., Paper S161, 8th Carbon Conf., Buffalo, Pergammon Press, New York, (1967).

SCHILLER, C., MERING, J., CORNVAULT, P. and du CHAFFAUT, F., Carbon, 5, 385, (1967(a)).

SCHILLER, C., MERING, J., CORNVAULT, P. and du CHAFFAUT, F., Carbon, 5, 507, (1967(b)).

SCHILLER, C., MERING, J. and OBERLIN, M., J. Appl. Cryst. 1, 282, (1968).

SCHOLTEN, J.J.F., BEERS, A.M. and DeWIT, L.A., Delft. Prog. Rev., 1, 29, (1973).

SCHOLTEN, J.J.F., BEERS, A.M. and KIEL, A.M., J. Catalysis, 36, 26, (1975).

SCHOLTEN, J.J.F. and DeWIT, L.A., J. Catalysis, 36, 30, (1975).

SCHRÖDINGER, E., Ann. Physik, 81, 109, (1962).

SCHULL, C.G., J. Am. Chem. Soc., 70, 1405, (1948).

SING, K.S.W., in "Surface Area Determination", Proc. Int. Symp. 1969, (eds. D.H. Everett and R.H. Ottewil), Butterworths, London, p25, (1970).

SLATER, J.C. and KIRKWOOD, J.G., Phys. Rev., A37, 682, (1931).

SLONCZEWSKI, J.C. and WEISS, P.R., Phys. Rev., 109, 272, (1958).

SMITH, D.J., CAMPS, R.A., FREEMAN, L.A., HILL, R., NIXON, W.C. and SMITH, K.C.A., J. Microsc., 130, 127, (1983).

STOECKLI, H.F., Chimia, 28, 727, (1974).

STOECKLI, H.F., "Adsorption Physique a l'interface Gaz-Solid", Lecture Course, Neuchâtel, (1976).

STOECKLI, H.F., in "Characterisation of Porous Solids", (eds. S.J. Gregg, K.S.W. Sing and H.F. Stoeckli), SCI, London, p31, (1979).

STOECKLI, H.F., Proc Conf. Microstructures of Carbon and Graphite, Glasgow, vol.13, (1980).

STOECKLI, H.F. and HUBER, U., Agents and Actions, 3, 411, (1977).

STOECKLI, H.F. and KRAEHENBUEHL, F., Carbon, 22, 297, (1984).

TAIT and DEWAR, Proc. Roy. Soc. (Edinburgh), 8, 348, (1874 (a)).

TAIT and DEWAR, Proc. Roy. Soc. (Edinburgh), 8, 628, (1874 (b)).

TRAPNELL, B.M.W., in "Catalysis", (ed. P.H. Emmett), Rheinhold Publ. Corp., New York, p1, (1955).

UBBELOHDE, A.R., Nature, 180, 380, (1957).

UBBELOHDE, A.R. and LEWIS, F.A.,"Graphite and its Crystal Compounds", Oxford University Press, (1960).

VALTER, V., in "Active Carbon", (eds. M. Smisek and R.S. Cerny), Elsevier, Amsterdam, p219, (1970).

WALKER Jr., P.L., RUSNIKO Jr., F. and AUSTIN, L.G., in "Advances in Catalysis", (eds. D.D. Eley et al.), Academic Press, London, vol.2, p133, (1959).

WARREN, B.E., Phys. Revs., 59, 693, (1941).

WARREN, B.E., Proc. 1st and 2nd Carbon Conf., Buffalo, 1953, 1955, Waverly Press, University of Buffalo, New York, 49, (1956).

WARREN, B.E. and BODENSTEIN, P., Acta, Cryst., 18, 262, (1965).

WARREN, B.E. and BODENSTEIN, P., Acta. Cryst., 20, 602, (1966).

WEIBULL, W., J. Appl. Mech., 18, 293, (1951).

WHELAN, M.J., Inst. Metals, 87, 392, (1959).

WILLIAMS, G.C. and FALLIN, E.A., Ind. Eng. Chem., 35, 251, (1943).

WOLF, R.J. and JOY, D.C., Proc. 27th. EMAG, 34, Institute of Physics, (1971).

WOODRUFF, E.M., J. Chim. Phys. (Special Issue) 96, (1969).

YOUNG, D.M. and CROWEL, A.D., "Physical Adsorption of Gases", Butterworths, London, (1962).

ZAVERINA, E.D. and DUBININ, M.M., Zh. Fz. Khim., 13, 151, (1939).

ZETTLEMOYER, A.C. and NARAYAN, K.S., in "The Solid-Gas Interface", (ed E.A. Flood), Dekker, New York, (1967).

ZWORYKIN, V.K., MORTON, G.A., RAMBERG, E.G., HILLIER, J and VANCE, A.W., in "Electron Optics and the Electron Microscope", Wiley, New York, (1945).

List of Plates

15. Micrograph of CEP-17 showing an enlargement of the boxed area of plate 14.
16. Micrograph of CEP-31 showing the presence of "cavities" near to the edge of the sample.
17. Micrograph of CEP-*35 showing the presence of "cavities" near to the edge of the sample.
18. Micrograph of CEP-51 showing the presence of "cavities" near to the edge of the sample.
19. Micrograph of CEP-51 showing short range lattice fringes.
20. Micrograph of CEP-49, the arrows indicating the presence of larger pore types.
21. Micrograph of CEP-51 showing different types of pores.
22. Micrograph of CEP-18 showing possible evidence of collapsing mechanism during pore formation.

Plate 1.

Micrograph of CEP-49 showing the unsuitability of standard carbon coated electron microscope grids when viewing carbon samples.

Magnification = X 1515000

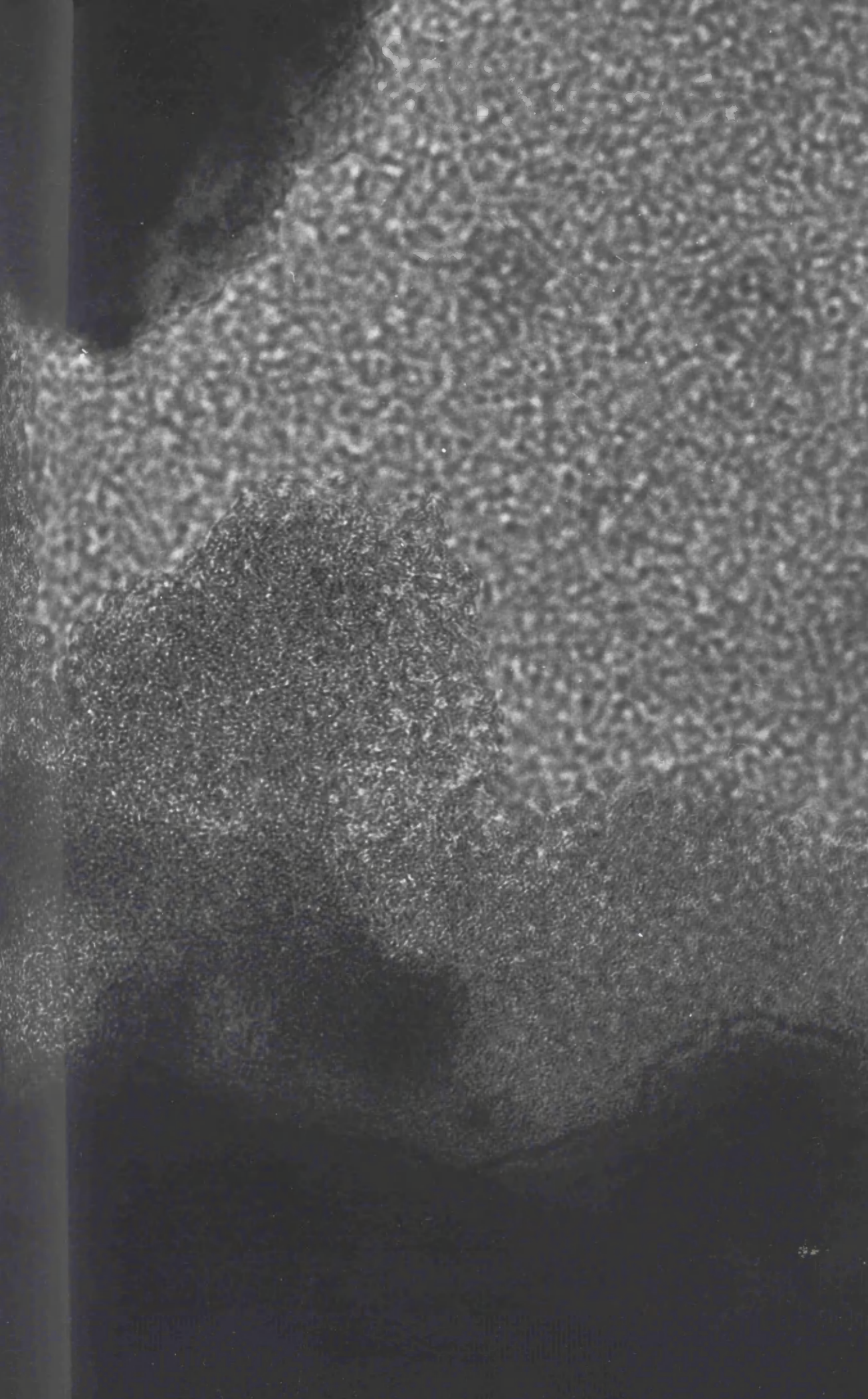

Plate 2.

Micrograph of CEP-18 showing extensive lattice imaging.

Magnification = X 2025000

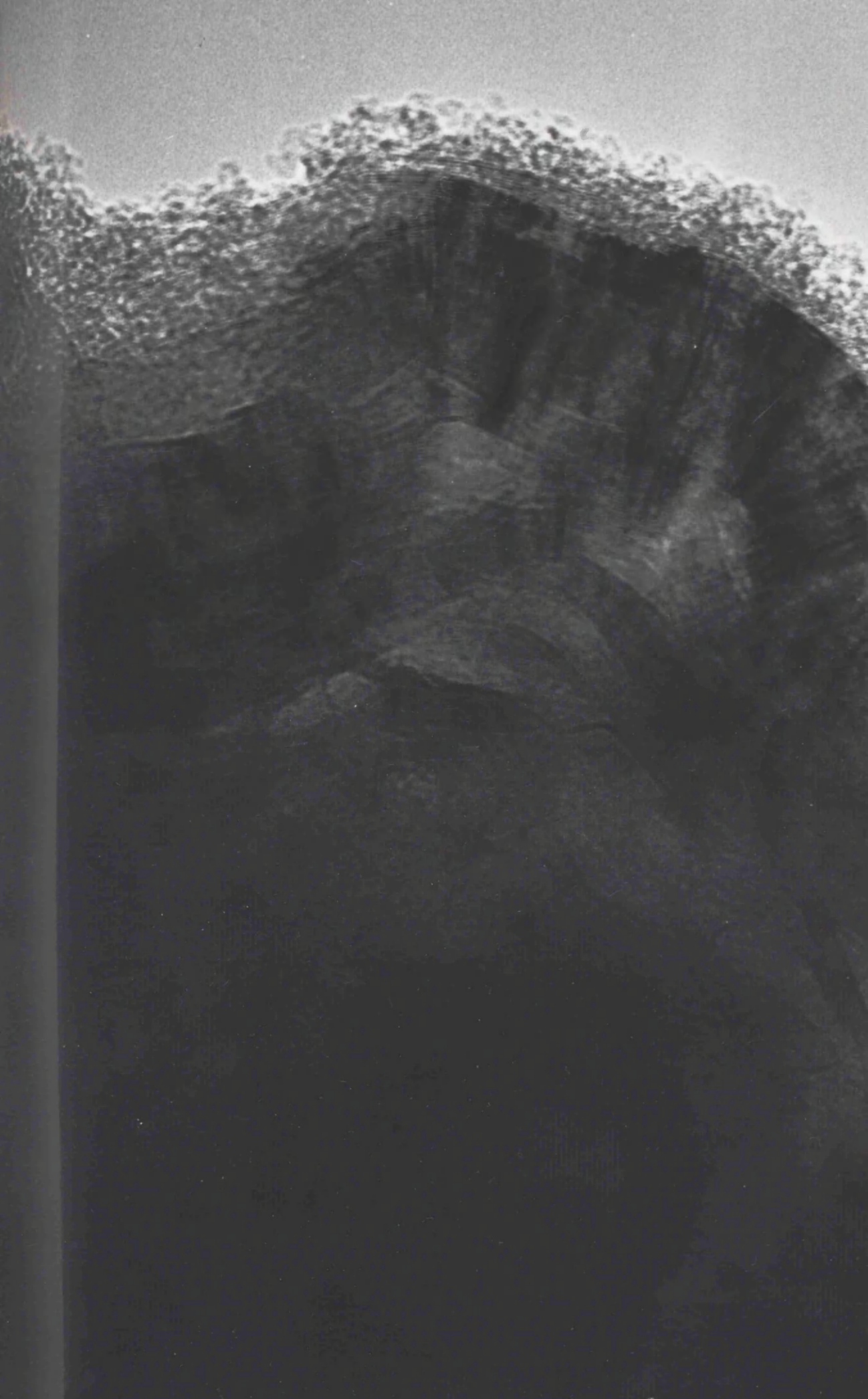

Plate 3.

Micrograph of CEP-18, the arrows indicating the presence of micropores.

Magnification = X 1225000

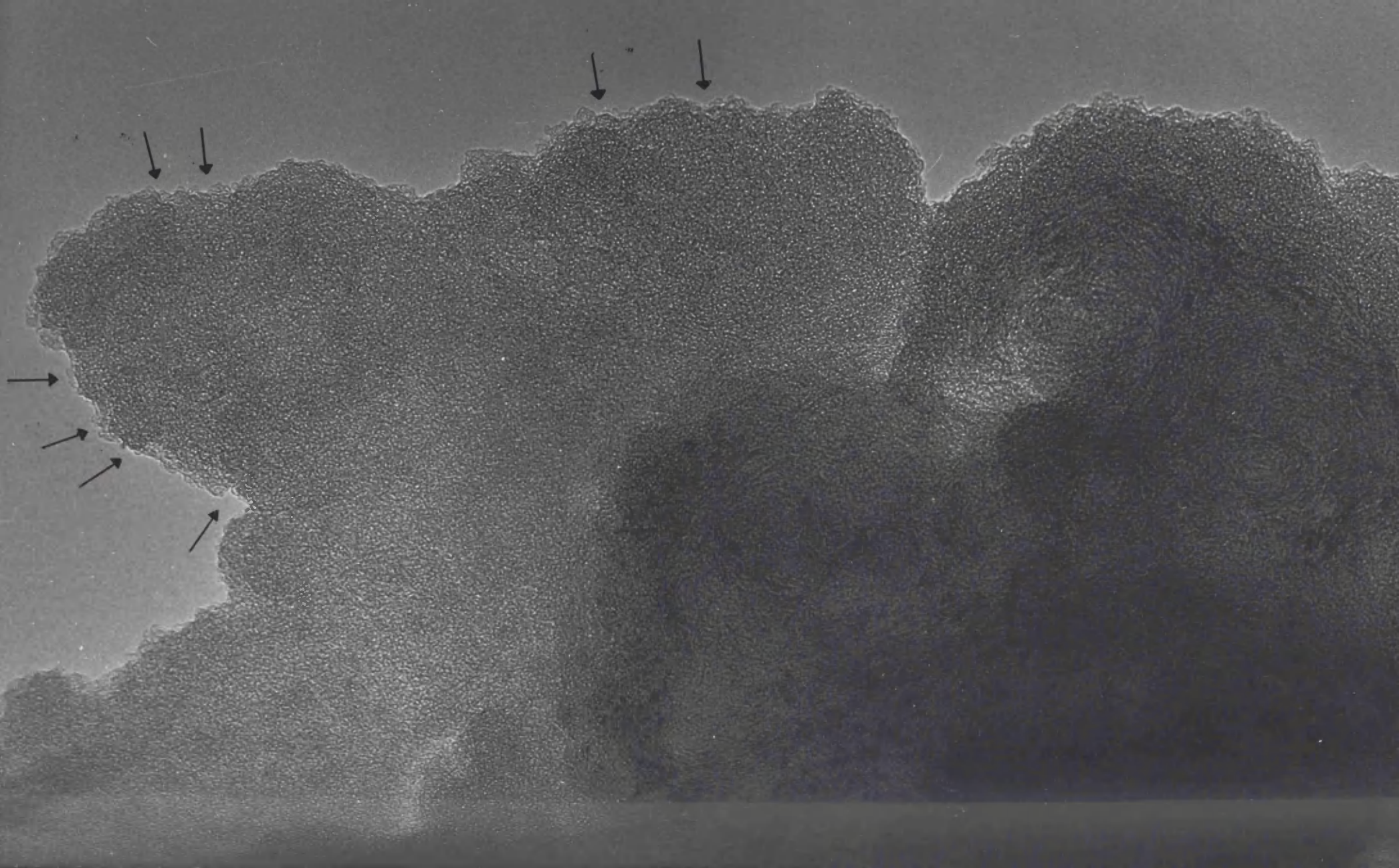

Plate 4.

Micrograph of CEP-18 showing "ribbon" like structure.

Magnification = X 2190000

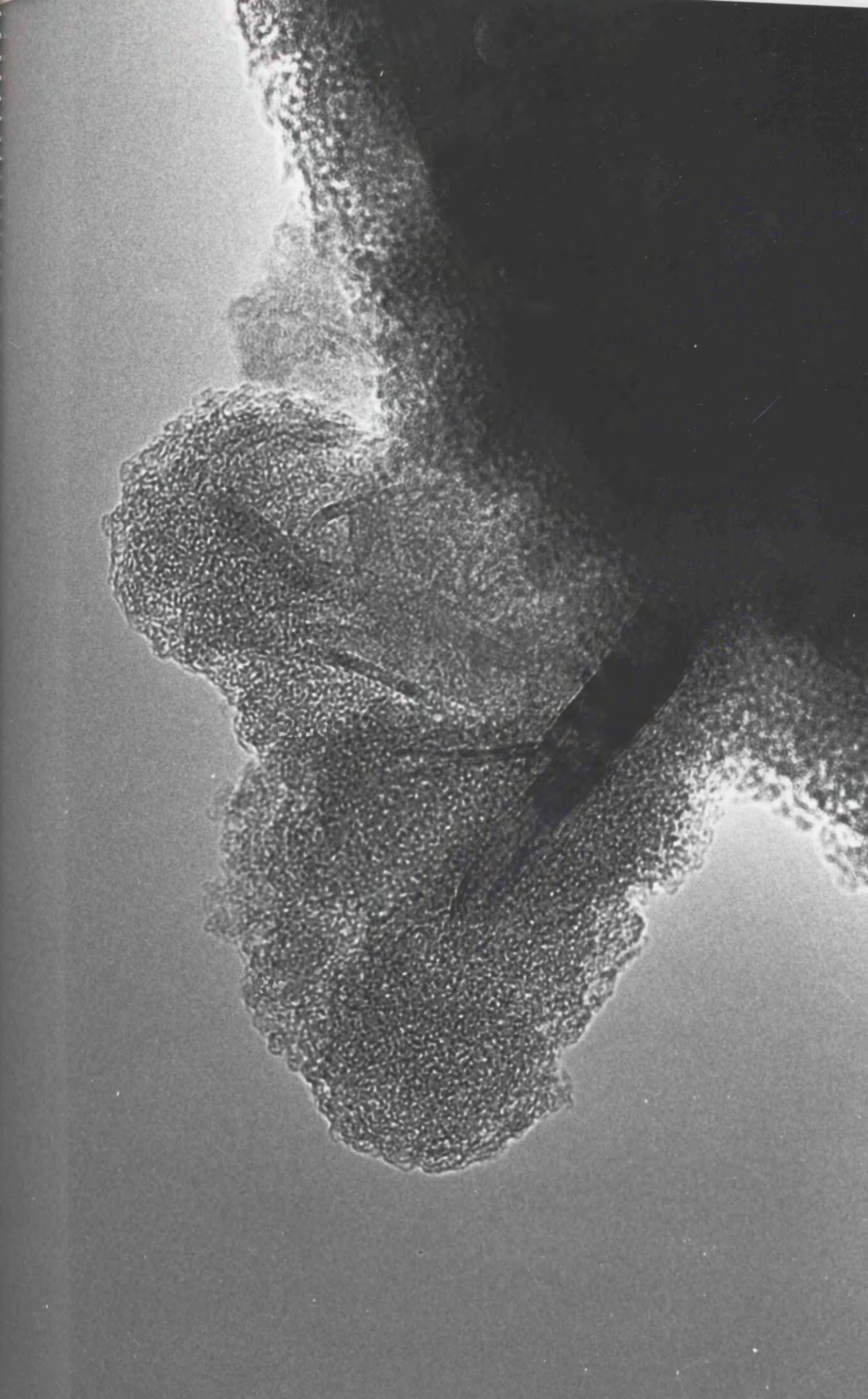

Plate 5.

Micrograph of CEP-18 showing the same area as plate 4. but at a greater defocus value, showing the presence of lattice fringes.

Magnification = X 2190000

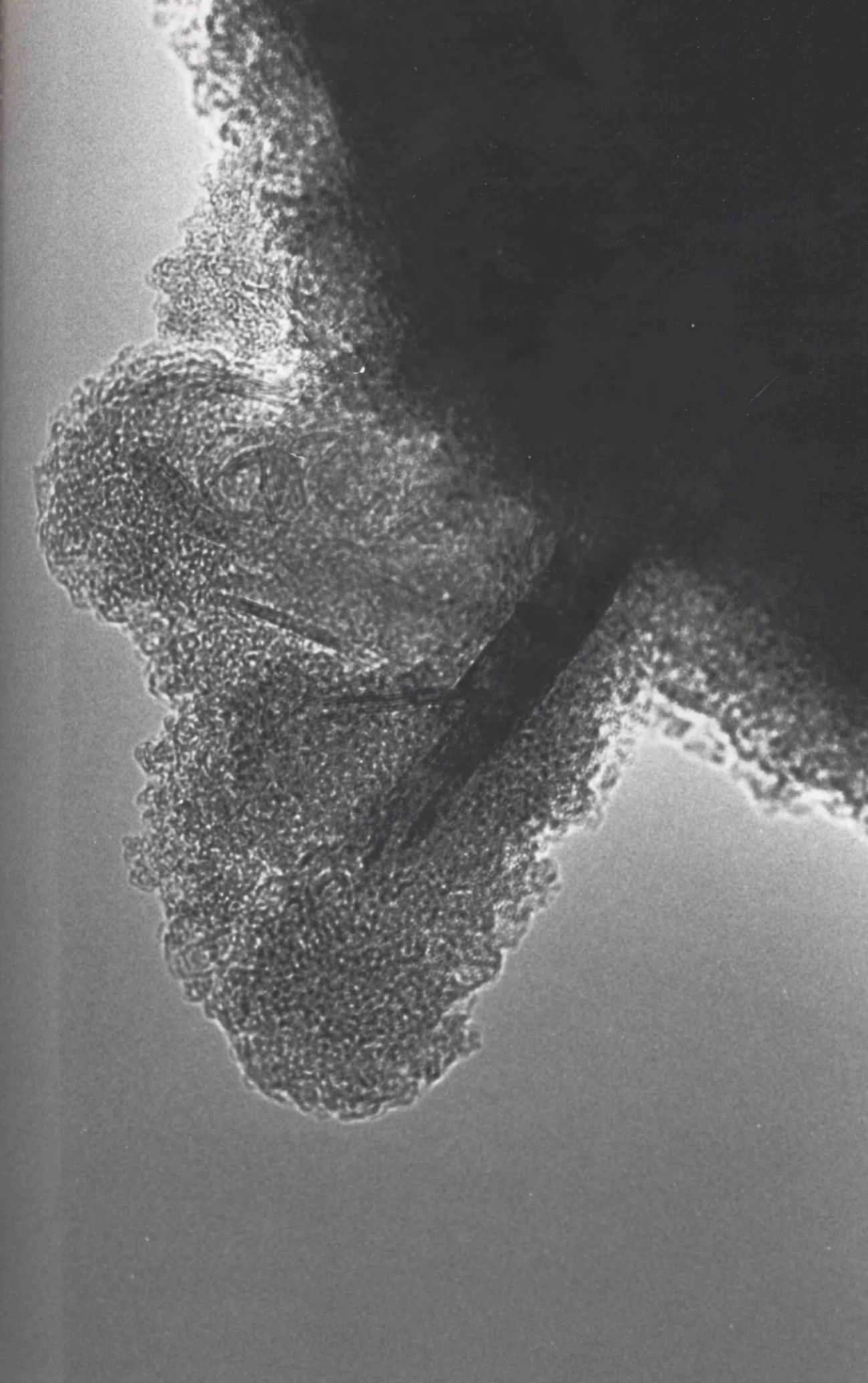

Plate 6.

Micrograph of CEP-18 showing various structural types.

Magnification = X 2130000

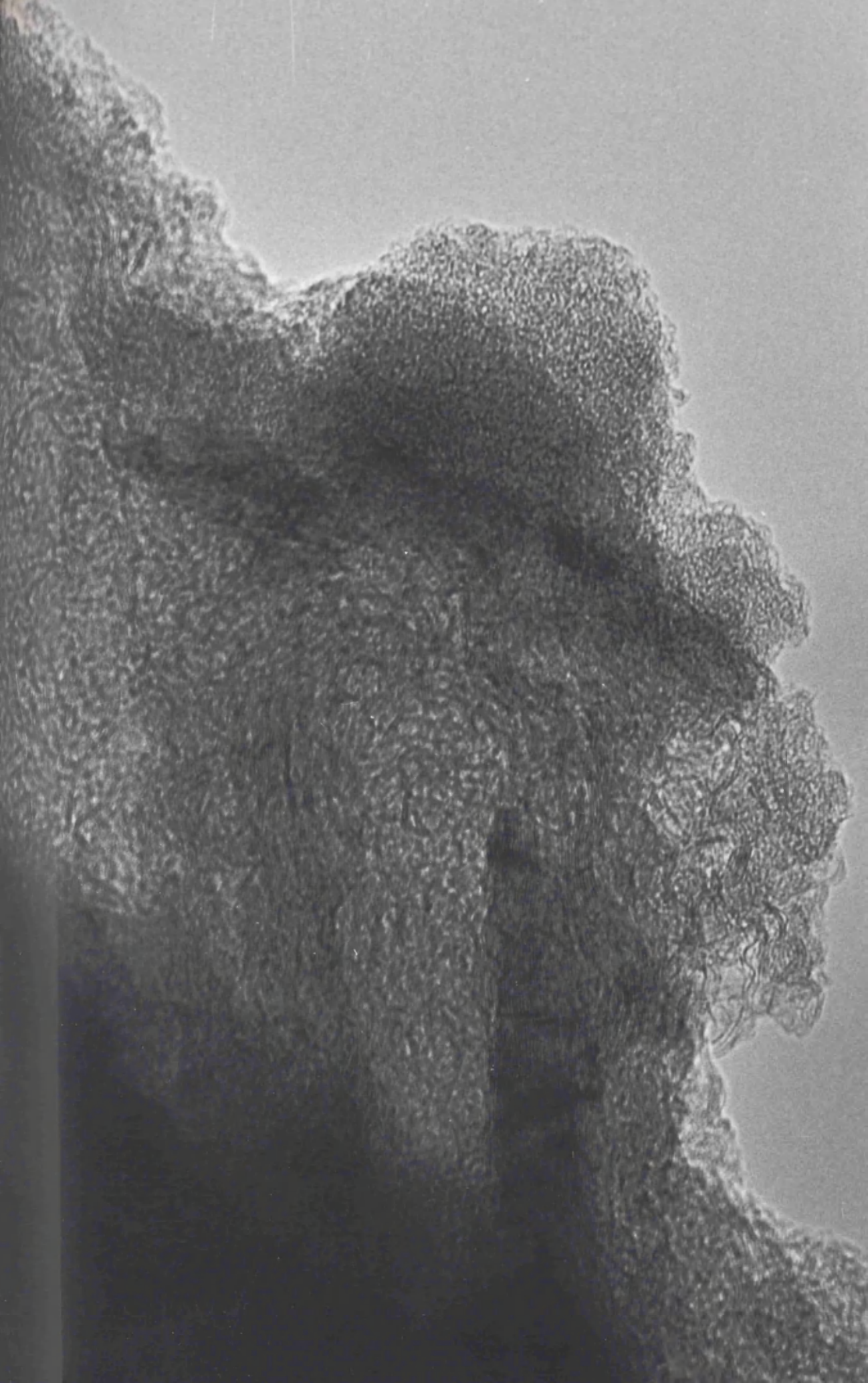

Plate 7.

Micrograph of CEP-18 showing an area of plate 6. at a greater magnification.

Magnification = X 5055000

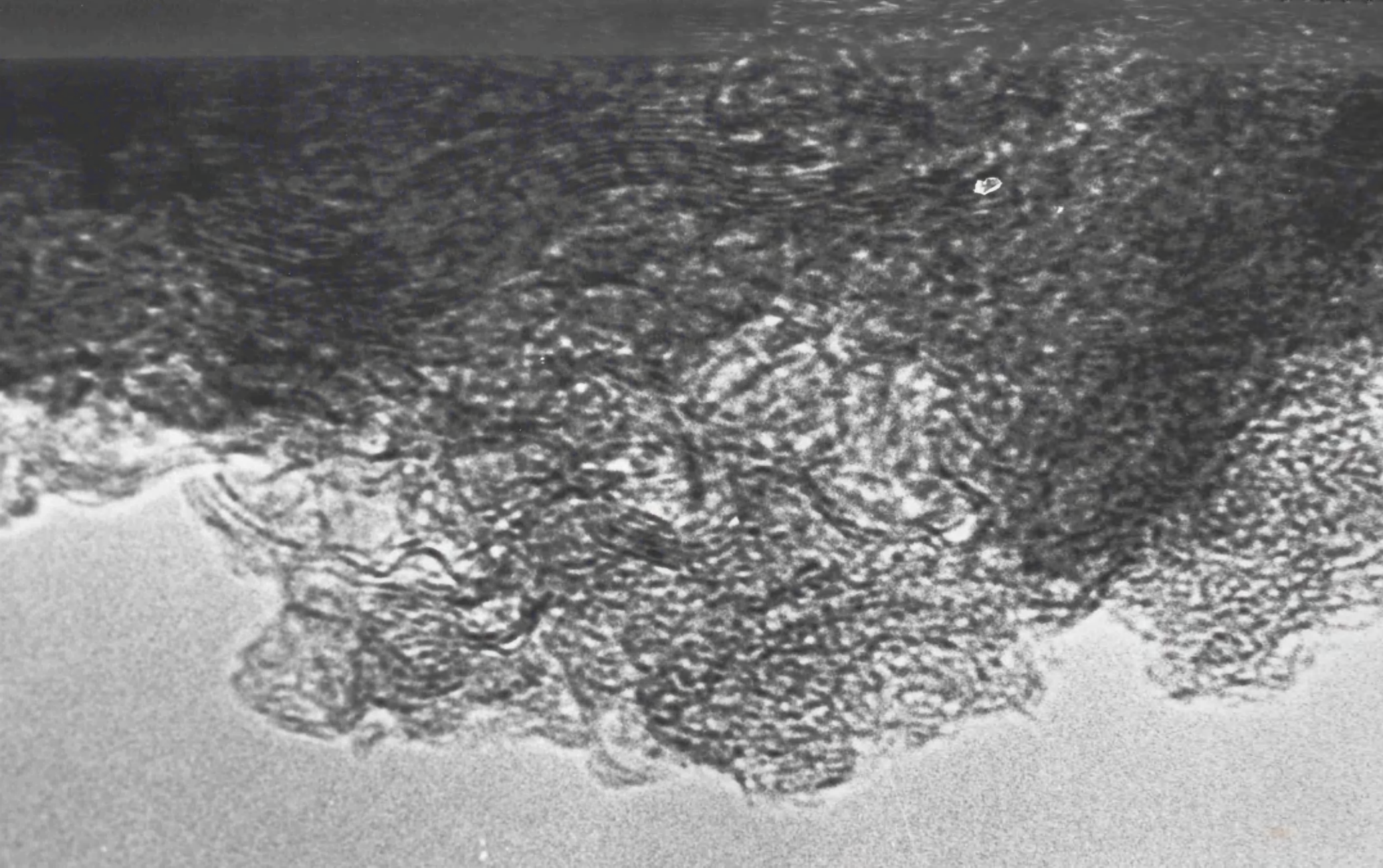

Plate 8.

Micrograph of CEP-18 showing an area of plate 6. at a greater magnification.

Magnification = X 5055000

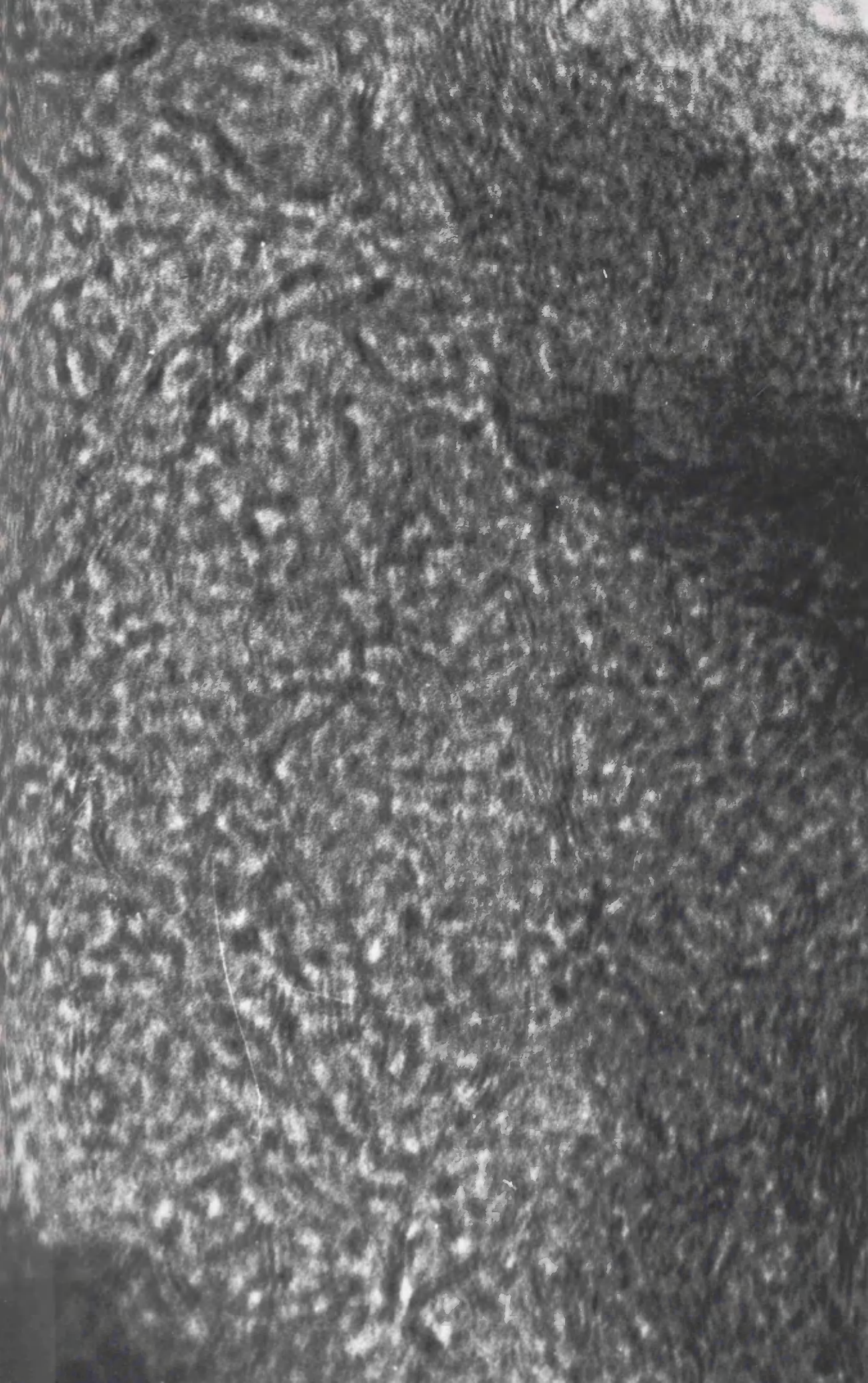

Plate 9.

Micrograph of CEP-35 showing porous structure.

Magnification = X 1695000

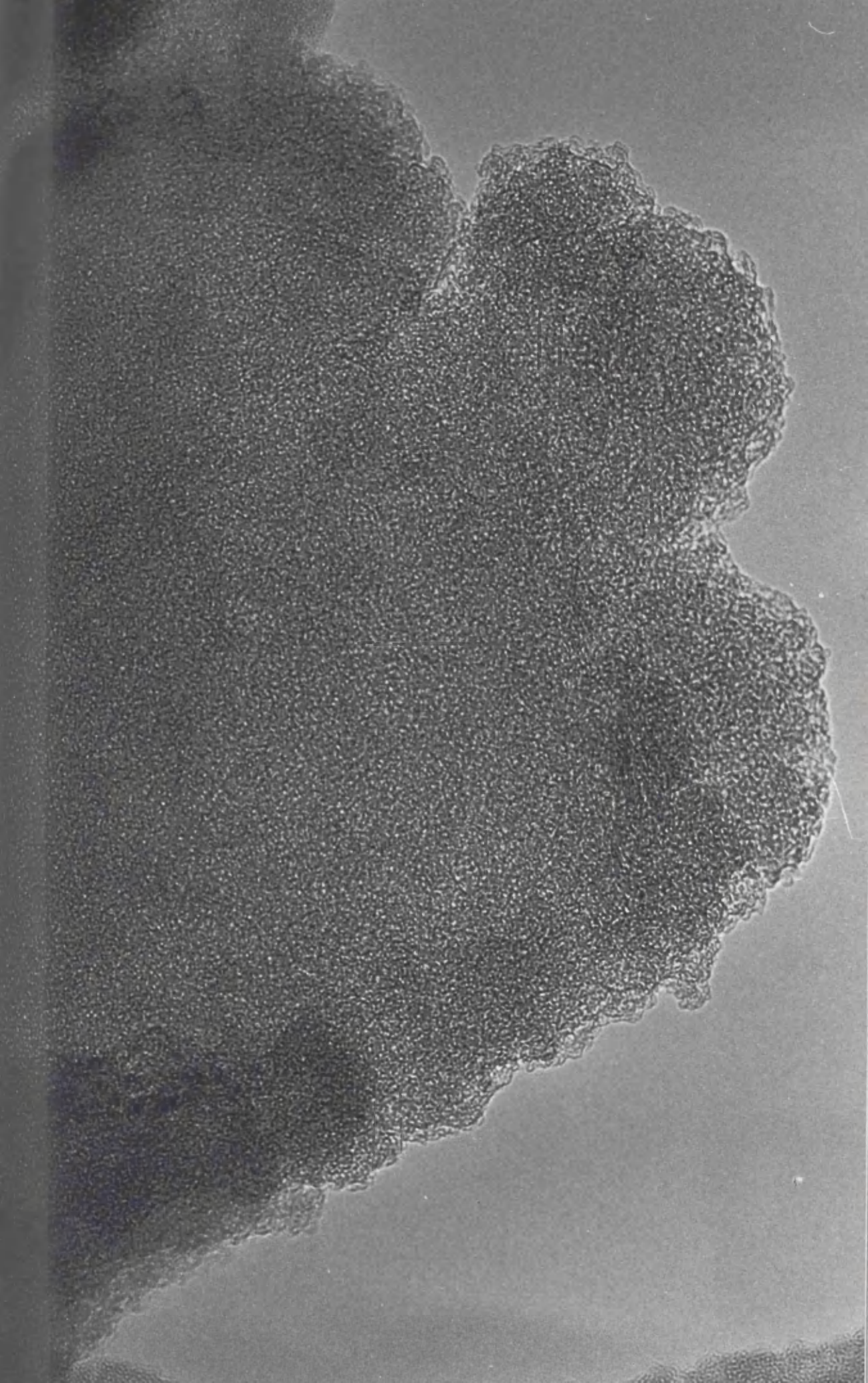

Plate 10.

Micrograph of CEP-35 showing short range lattice fringes.

Magnification = X 1740000

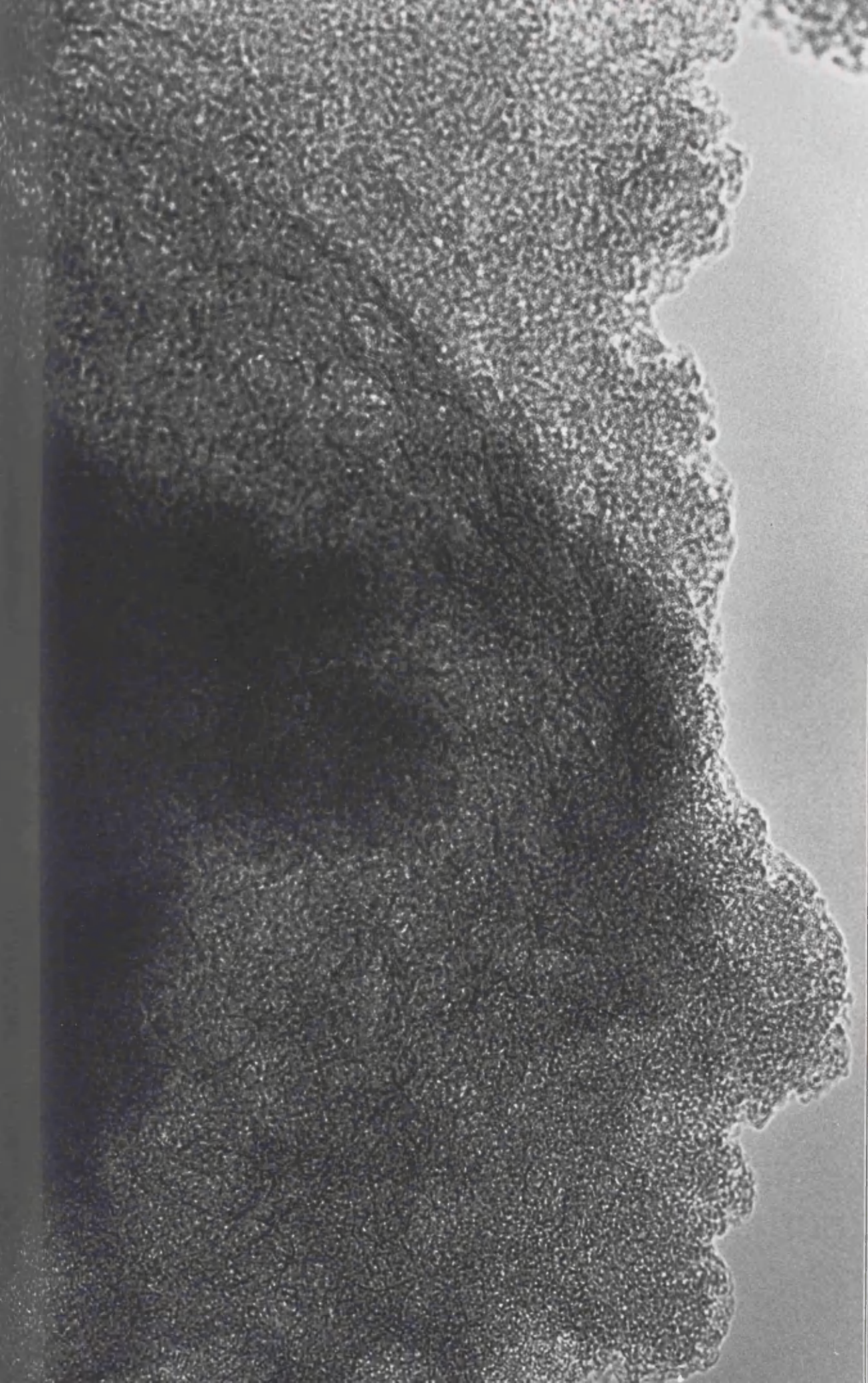

Plate 11.

Micrograph of CEP-35 showing more "ordered" porous region.

Magnification = X 1725000

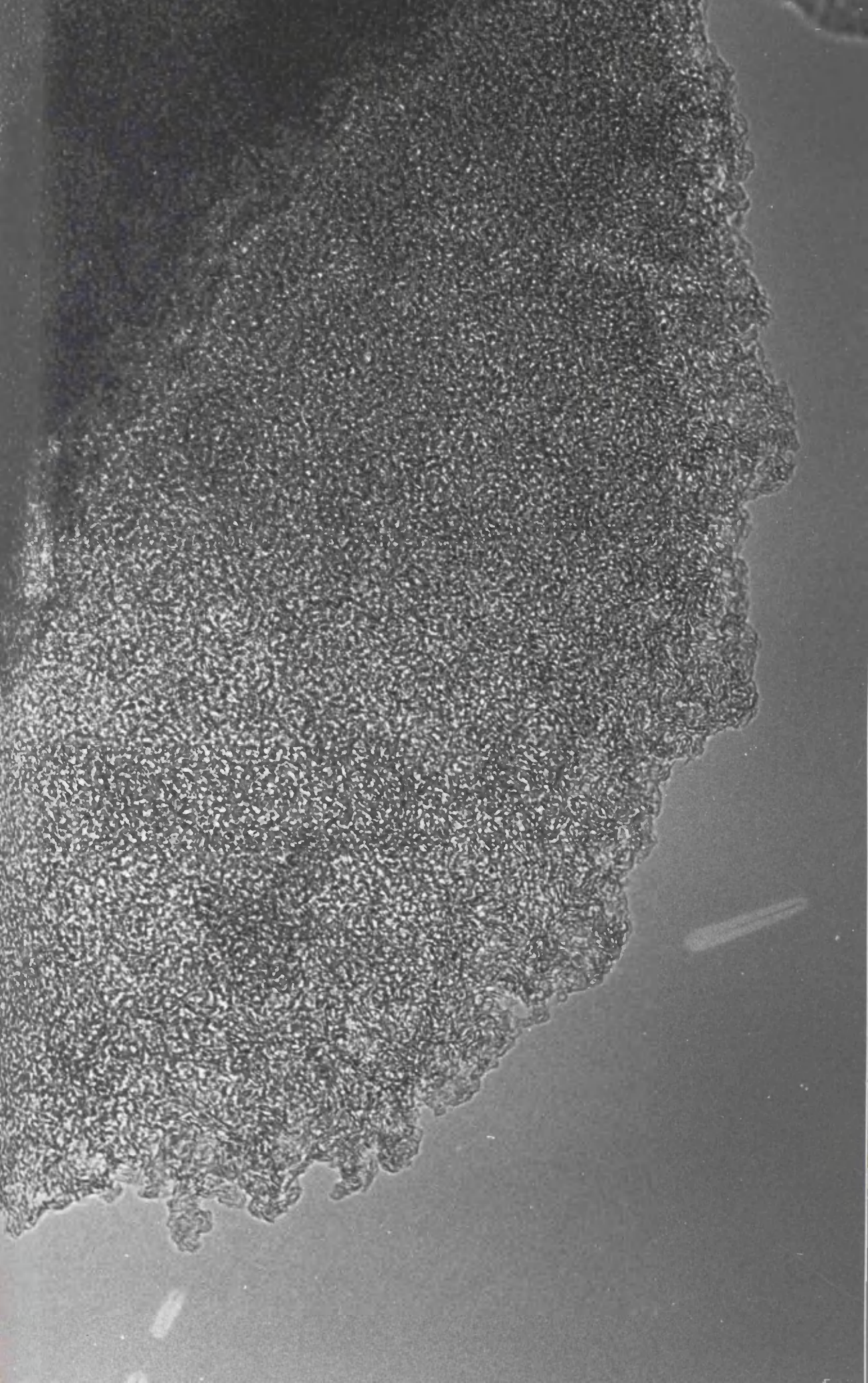

Plate 12.

Micrograph of CEP-49 showing fairly extensive lattice fringes.

Magnification = X 1725000

Plate 13.

Micrograph of CEP-17.

Magnification = X 1725000

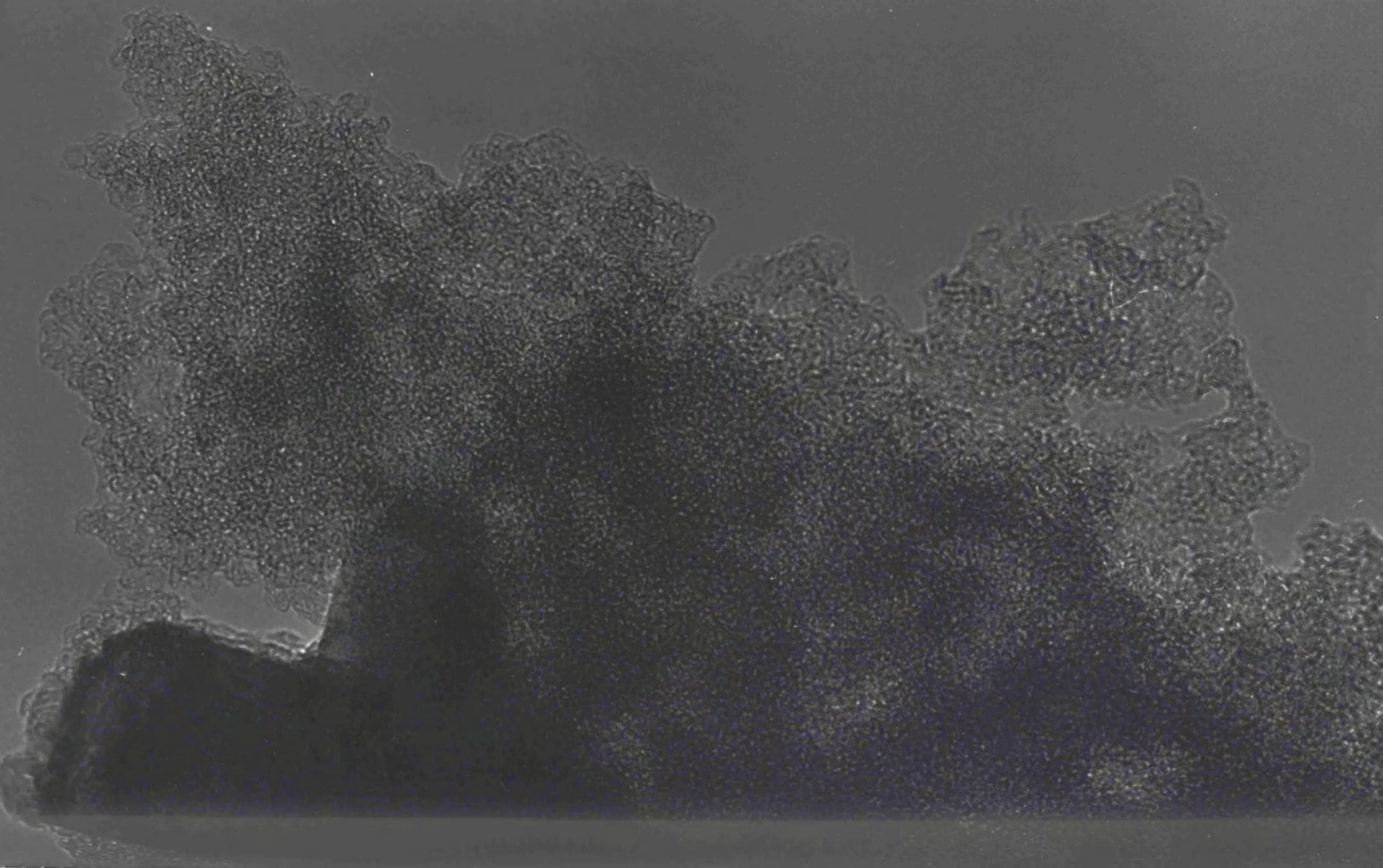

Plate 14.

Micrograph of CEP-17 showing short range lattice fringes.

Magnification = X 1350000

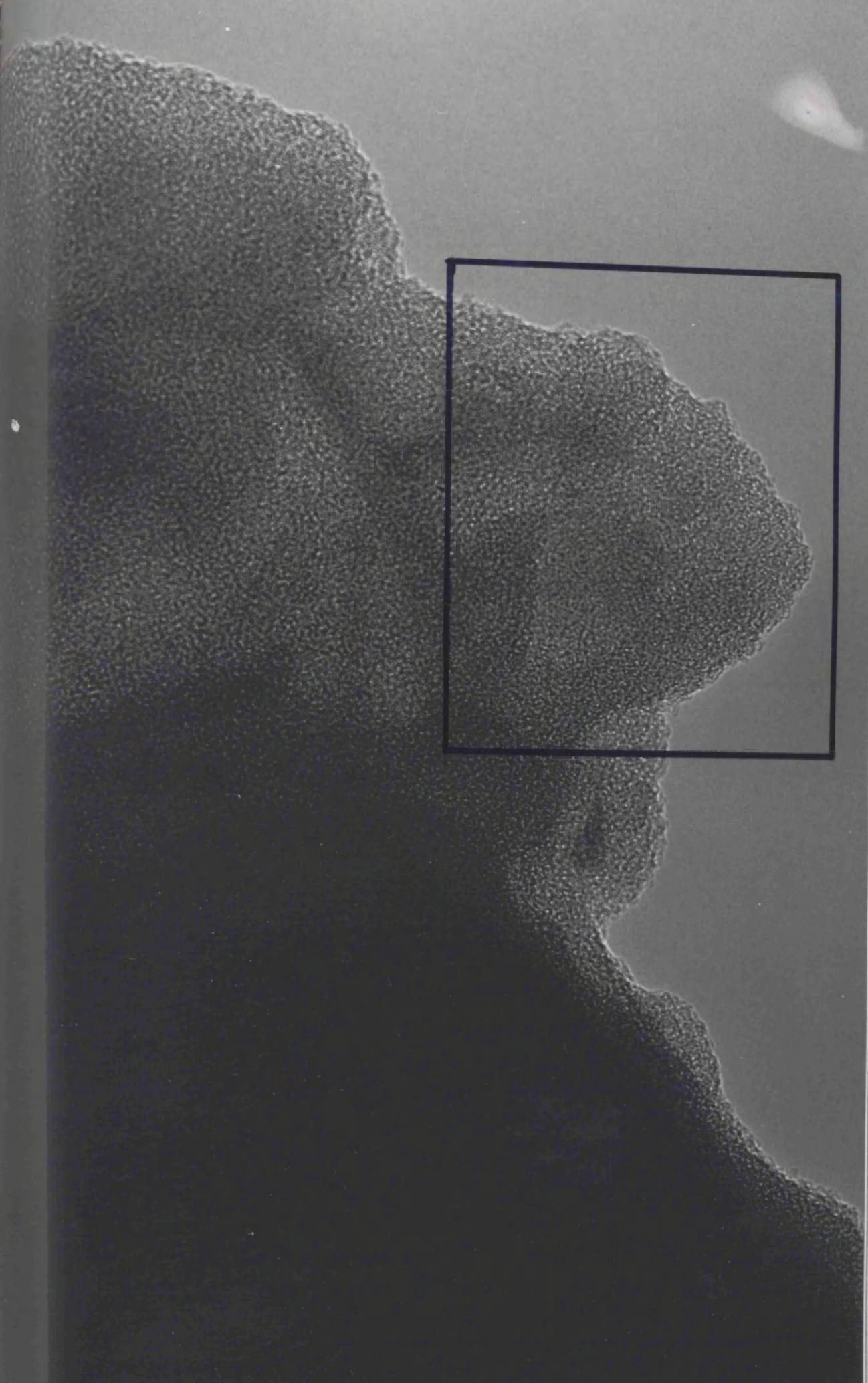

Plate 15.

Micrograph of CEP-17 showing an enlargement of the boxed area of plate 14.

Magnification = X 3465000

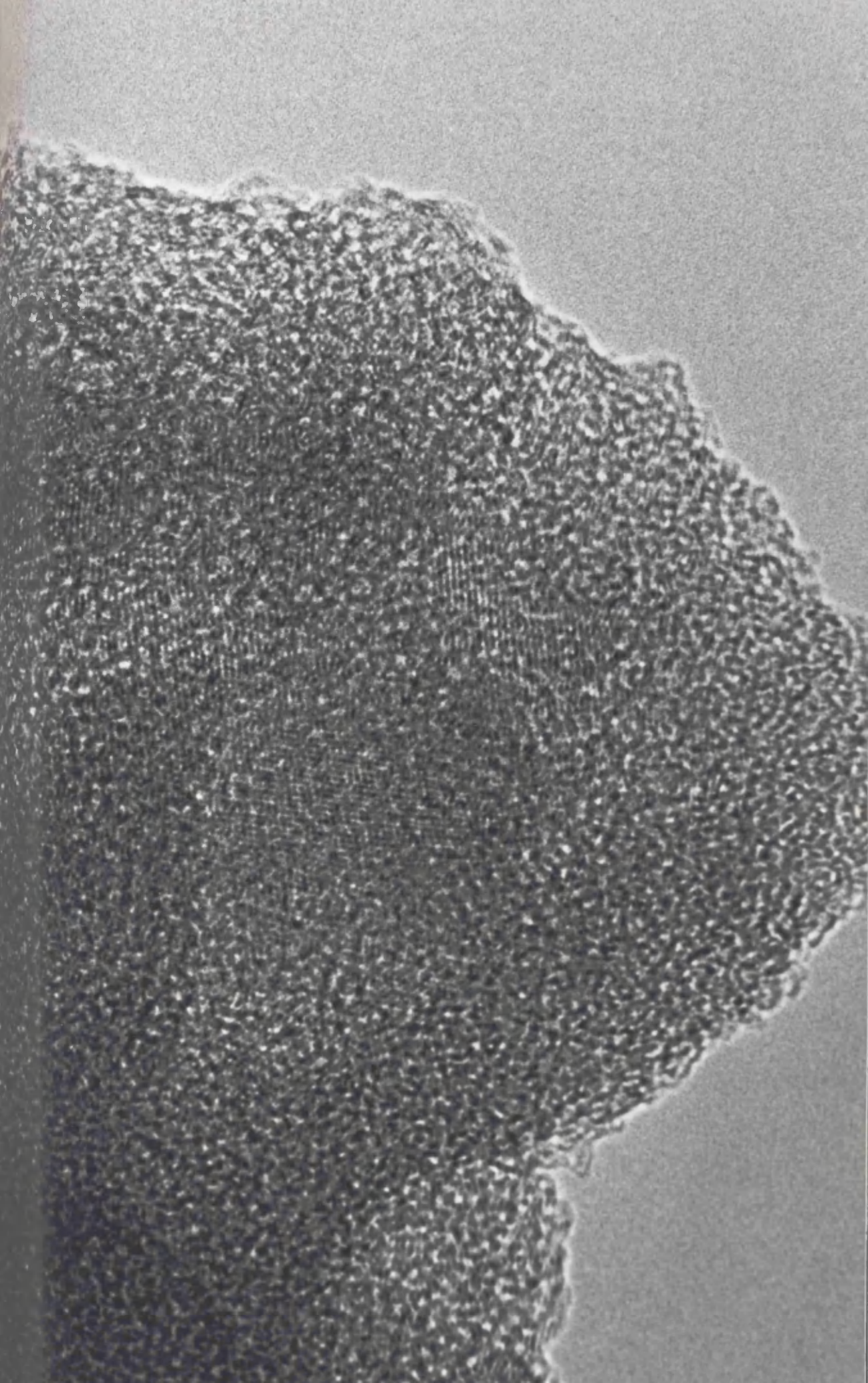

Plate 16.

Micrograph of CEP-31 showing the presence of "cavities" near to the edge of the sample.

Magnification = X 1800000

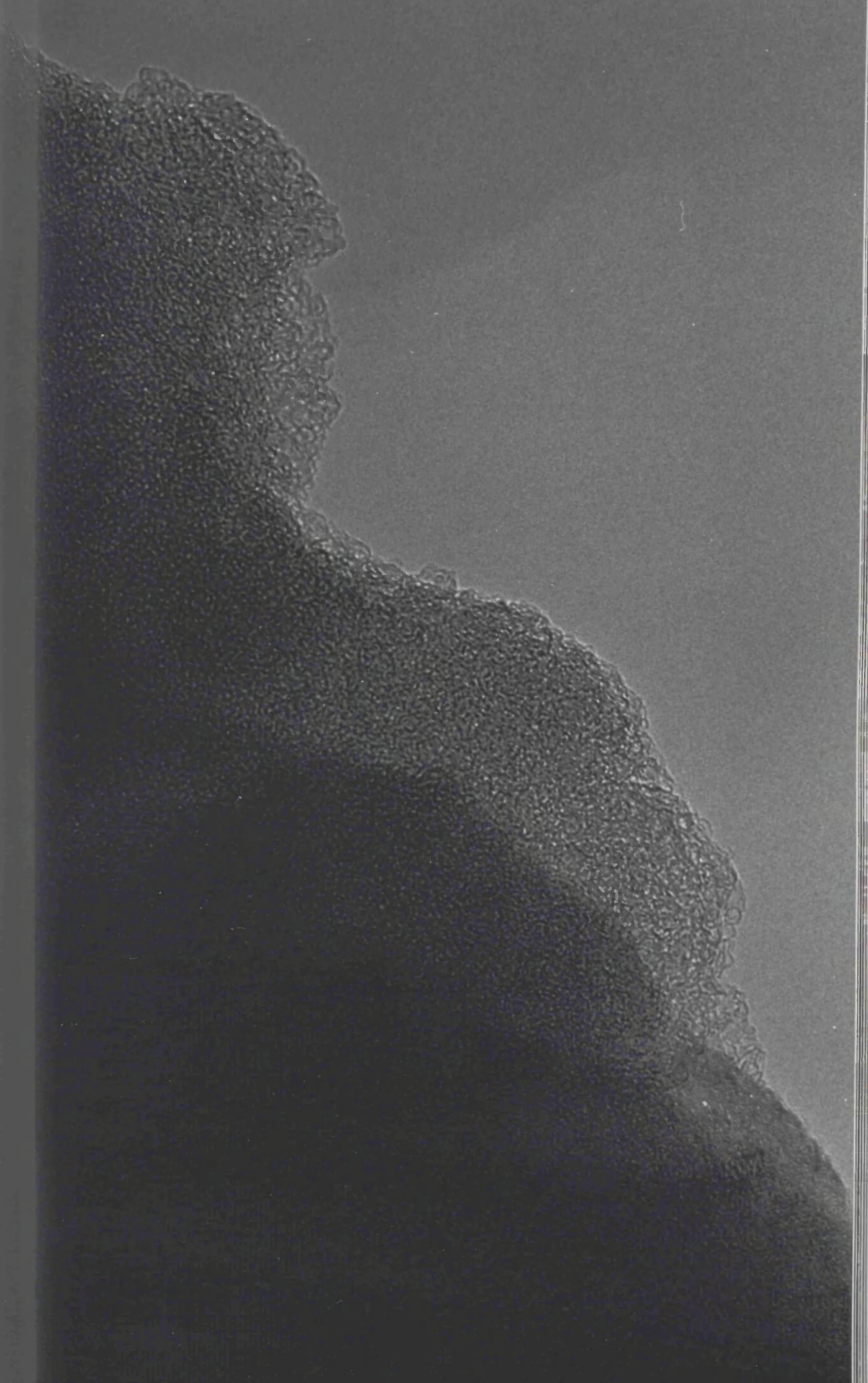

Plate 17.

Micrograph of CEP-*35 showing the presence of "cavities" near to the edge of the sample.

Magnification = X 1800000

Plate 18.

Micrograph of CEP-51 showing the presence of "cavities" near to the edge of the sample.

Magnification = X 1800000

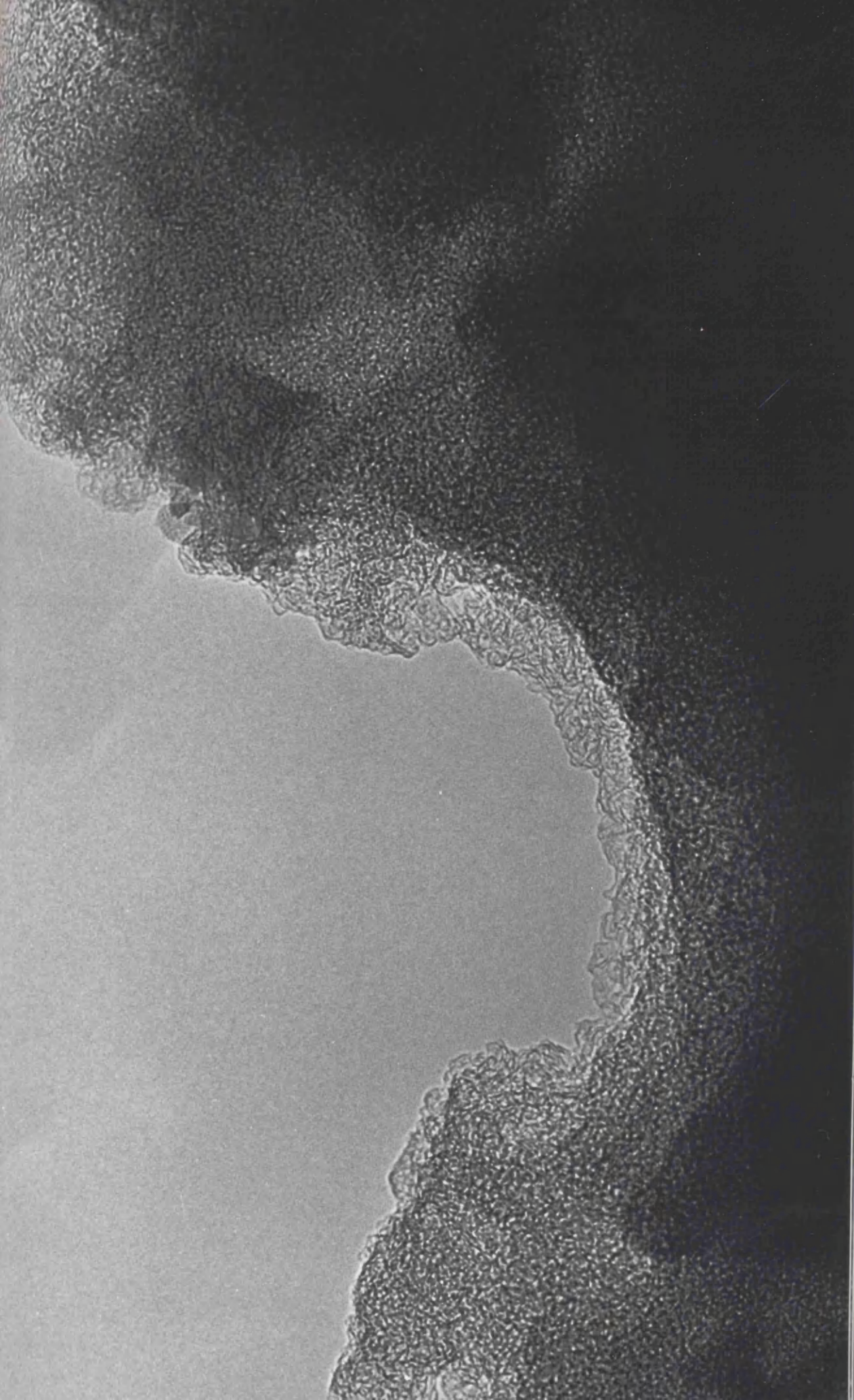

Plate 19.

Micrograph of CEP-51 showing short range lattice fringes.

Magnification = X 3465000

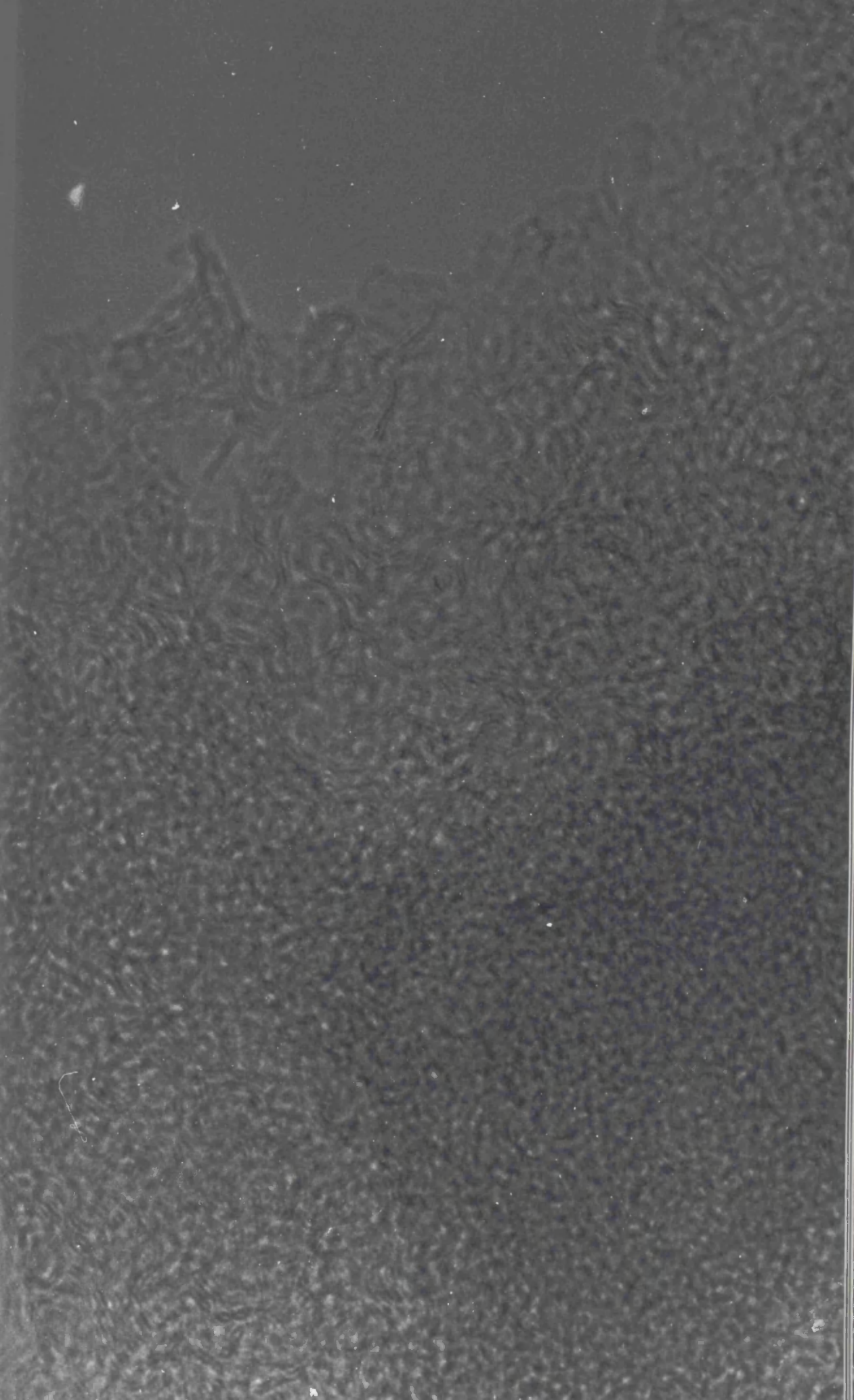

Plate 20.

Micrograph of CEP-49, the arrows indicating the presence of larger pore types.

Magnification = X 1800000

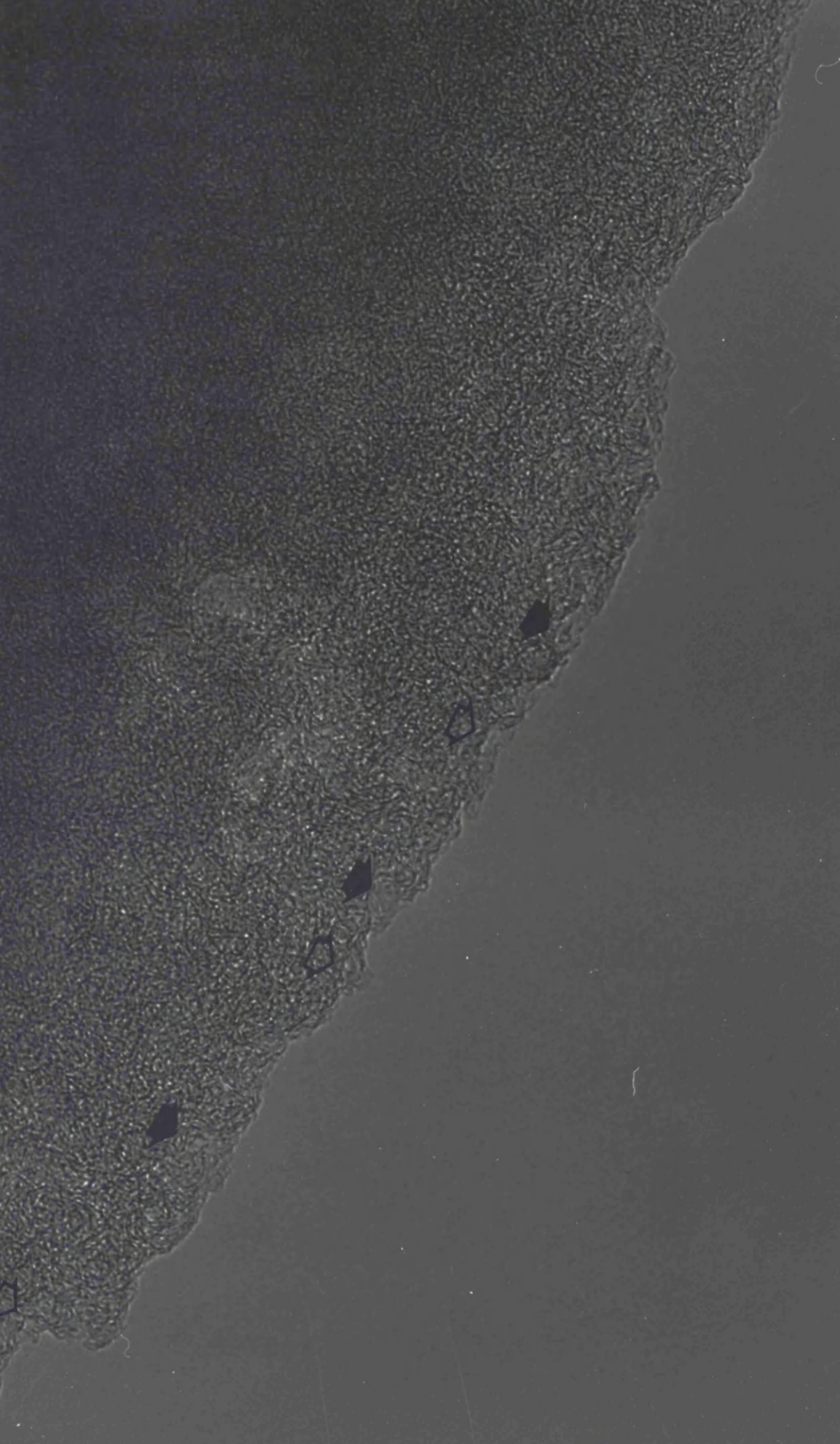

Plate 21.

Micrograph of CEP-51 showing different types of pores.

Magnification = X 2055000

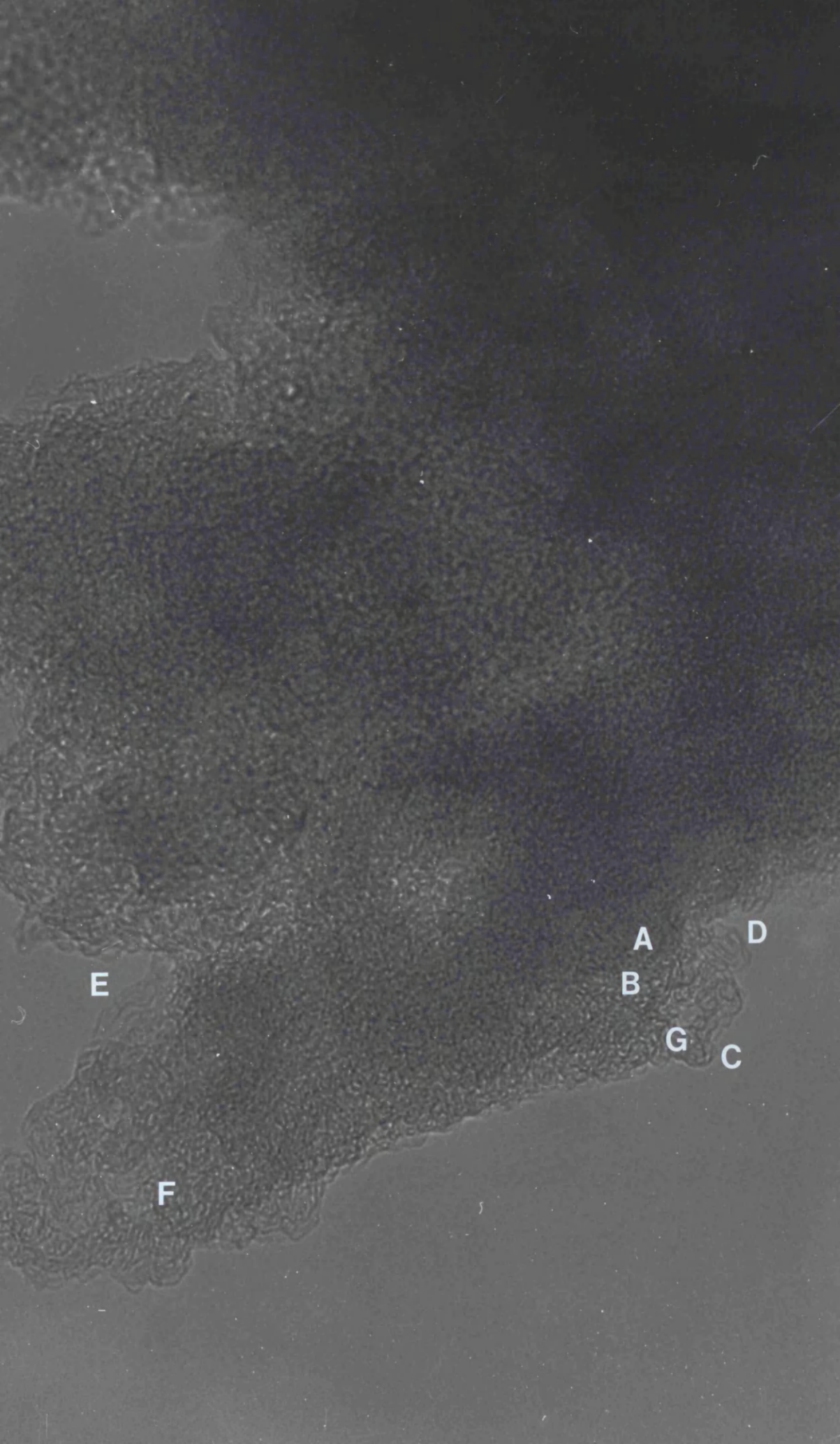
A
D
E
B
G
C
F

Plate 22.

Micrograph of CEP-18 showing possible evidence of collapsing mechanism during pore formation.

Magnification = X 4115000

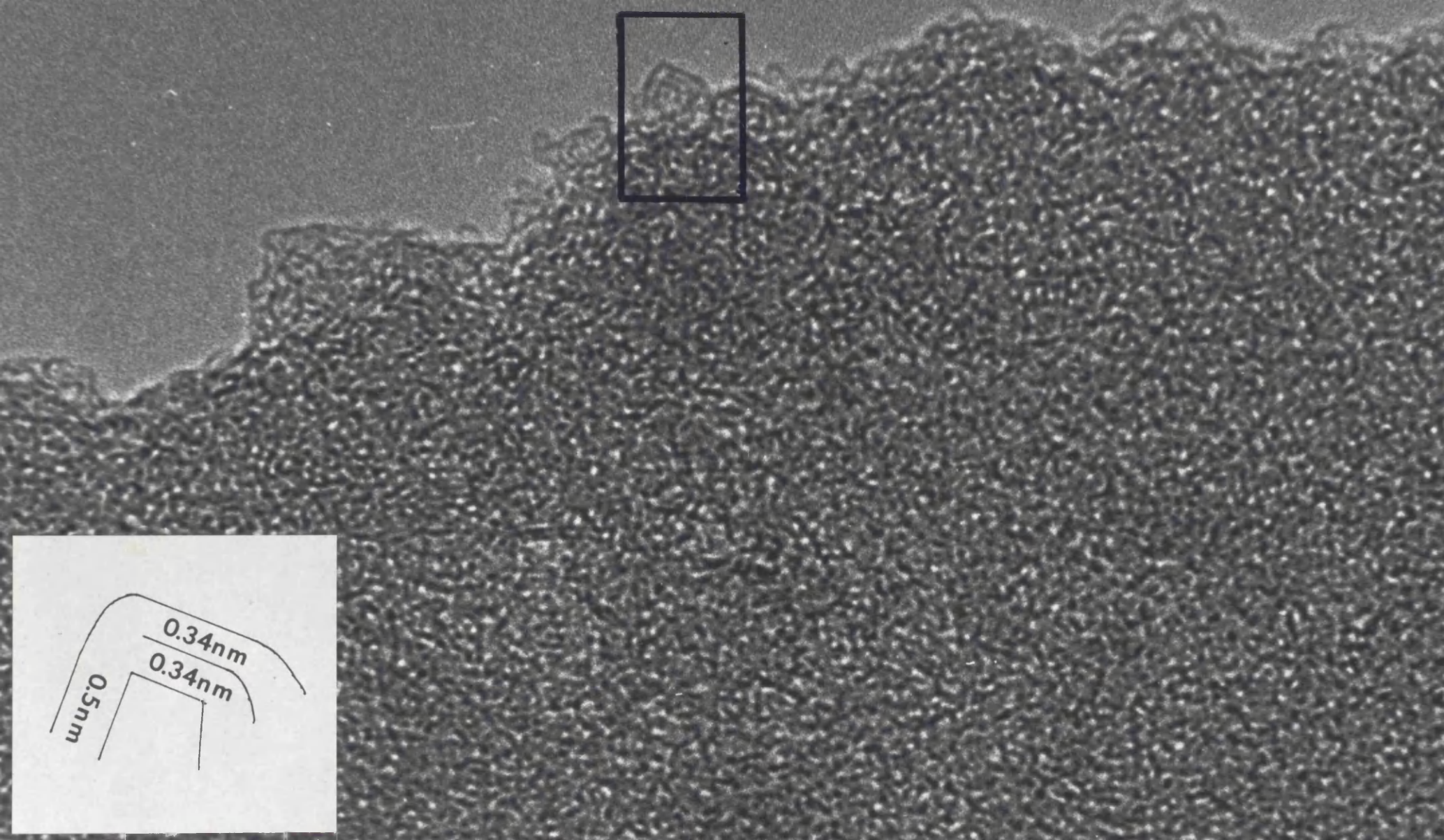
0.34nm
0.34nm
0.5nm